

Atomic-scale Characterization of Strain and Gate effects on Two-dimensional Materials by Scanning Tunneling Microscopy

Présentée le 11 septembre 2023

Faculté des sciences de base
Laboratoire de science à l'échelle nanométrique
Programme doctoral en physique

pour l'obtention du grade de Docteur ès Sciences

par

Jz -Yuan JUO

Acceptée sur proposition du jury

Prof. P. Ricci, président du jury
Prof. K. Kern, directeur de thèse
Prof. J. Meyer, rapporteur
Prof. K. Bolotin, rapporteur
Prof. N. Grandjean, rapporteur

Abstract

Strain is an inevitable phenomenon in two-dimensional (2D) material, regardless of whether the film is suspended or supported. Moreover, strain is known to alter the physical and chemical properties, such as the band gap, charge carrier effective masses, dielectric properties, chemical reactivity, and many more.

One example is the metal-2D material junction, where the interaction at the interface between the contact electrode can be significantly altered by strain. Moreover, the response to strain varies depending on the contact material used. In this study, we explored different substrate roughness levels and investigated the interface properties between monolayer MoS₂ and metal using X-ray photoelectron spectroscopy, atomic force microscopy, and Raman spectroscopy. Furthermore, to enable the direct measurement of strain response, I successfully developed a nanoindentation system integrated with a scanning tunneling microscopy (STM) sample holder. The system allows for in-situ reversible control of strain and gate electric fields. It utilizes a gearbox and a piezoelectric actuator, providing precise control of indentation depth at the nanometer level. The 2D materials are placed on a flexible polyimide film to ensure mechanical stability, and a Pd clamp is used to improve the transfer of strain from the polyimide to the 2D layers. The small size of the sample holder ($\sim 160 \text{ mm}^2 \times 5.2 \text{ mm}$) makes it compatible with a broad range of measurement systems, including atomic force microscopy and Raman spectroscopy, in addition to STM. By employing the novel approach described above, the study has successfully observed atomic precision strain responses of 2D materials like graphene and monolayer MoS₂. In their relaxed states, strain mostly arises from local curvature caused by the polyimide surface roughness. However, when the materials are under strained conditions with tented structures, lattice parameters become more sensitive to changes in indenter height, leading to additional stretching strain. The indentation system allows for further adjustments to the indenter and sample configuration, which enable the application of uniaxial strain for measuring the Poisson's ratio.

As a future perspective, we identify existing challenges related to performing local spectroscopy and research topics on defect in-gap states in monolayer MoS₂.

Keywords: strain, scanning tunneling microscopy, two-dimensional materials, graphene, monolayer MoS₂, Poisson's ratio, metal contact, gate

Zusammenfassung

„Strain“, ist ein unvermeidliches Phänomen in zweidimensionalen (2D) Materialien, unabhängig davon, ob der Film freitragend oder gestützt ist. Des Weiteren ist bekannt, dass Strain/Verformung die physikalischen und chemischen Eigenschaften, wie z.B. die Bandlücke, effektive Massen der Ladungsträger, dielektrische Eigenschaften, chemische Reaktivität und vieles mehr, verändern kann.

Ein Beispiel hierfür ist die Grenzfläche zwischen Metall und 2D-Material, bei der die Wechselwirkung an der Grenzfläche zur Kontakt-Elektrode durch Verformung erheblich verändert werden kann. Die Wirkung der Verformung variiert je nach verwendetem Kontaktmaterial. In dieser Arbeit wurden unterschiedliche Rauigkeitsgrade von Substraten untersucht und die Grenzflächeneigenschaften zwischen monolagigem MoS₂ und Metall mithilfe von Röntgenphotoelektronenspektroskopie, Rasterkraftmikroskopie und Raman-Spektroskopie analysiert. Darüber hinaus wurde erfolgreich ein Nanoindentationssystem entwickelt, das in einen Rastertunnelmikroskopie-(STM)-Probenträger integriert ist, um direkt die Reaktion des Materials auf die Strain-Belastung zu messen. Das System ermöglicht eine reversible in-situ Kontrolle von Strain und Gate-Spannung. Der Probenhalter ist eine Kombination aus einem Getriebe und einem piezoelektrischen Aktuator, wodurch eine präzise Kontrolle der Eindringtiefe im Nanometerbereich gewährleistet werden kann. Die 2D-Materialien werden auf einem flexiblen Polyimidfilm platziert, um mechanische Stabilität zu garantieren. Es wird eine Pd-Klemme verwendet, um die Übertragung von Verformung vom Polyimid zu den 2D-Schichten zu verbessern. Die geringe Größe des Probenträgers ($\sim 160 \text{ mm}^2 \times 5,2 \text{ mm}$) macht ihn mit einer breiten Palette von Messsystemen kompatibel, einschließlich Rasterkraftmikroskopie und Raman-Spektroskopie, neben STM. Durch die Anwendung des oben beschriebenen neuartigen Ansatzes wurden erfolgreich Verformungsreaktionen von 2D-Materialien wie Graphen und monolagigem MoS₂ mit atomarer Präzision beobachtet. Im relaxierten Zustand entsteht Verformung/Strain hauptsächlich durch lokale Krümmung, die durch die Rauheit der Polyimid-Oberfläche verursacht wird. Wenn die Materialien jedoch unter Spannung stehen, reagieren die Gitterparameter empfindlicher auf Änderungen der Indentorhöhe, was zu einer zusätzlichen Streckspannung führt. Das Indentationssystem ermöglicht weitere Anpassungen am Stempel und der Probenkonfiguration, die die Anwendung von uniaxialer Verformung zur Messung des Poisson-Verhältnisses ermöglichen.

Die lokale Spektroskopie unter Spannung stehender 2D Materialien sowie die elektronischen Zustände in Defekten von MoS₂ Monolagen sind interessante Fragestellungen zukünftiger Untersuchungen.

Zusammenfassung

Schlüsselwörter: Verformung, Rastertunnelmikroskopie, zweidimensionale Materialien, Graphen, monolagiges MoS₂, Poisson-Verhältnis, Metallkontakt, Gate

Contents

Abstract (English/Deutsch)	i
List of Figures	vii
List of Tables	ix
Abbreviations	xi
1 Introduction	1
2 Background	5
2.1 Strain Engineering in 3D Semiconductor Industry	6
2.2 Strain Engineering in 2D Materials	7
2.2.1 Graphene	9
2.2.2 Monolayer MoS ₂	11
2.2.3 Remark	15
3 Experimental Methods	17
3.1 Scanning Tunneling Microscopy	17
3.1.1 Strain- and Gate-Controllable Sample Holder	18
3.1.2 Data Analysis	21
3.2 Atomic Force Microscopy	24
3.3 X-ray Photoelectron Spectroscopy	25
3.3.1 Compatibility with Strain- and Gate-Controllable Sample Holder	27
3.4 Raman Spectroscopy	27
4 Materials and Sample Preparation	29
4.1 Polyimide Film	29
4.1.1 Transfer	29
4.1.2 UHV Compatibility of Polyimide Film	30
4.2 Transfer of Graphene and Monolayer MoS ₂	30
4.3 Deposition of Metal Contacts	32
4.4 Strain- and Gate-Controllable Sample Holder	34
4.4.1 Assembly	34
4.4.2 Indentor Approaching	35

Contents

4.4.3 Loading to STM	37
5 In-situ Atomic Level Observation of the Strain Response of Graphene Lattice	39
5.1 Macroscopic Scale Insight	39
5.2 Atomic Scale Characterization	42
5.3 Conclusions	50
6 Atomic-Scale Determination of Poisson's Ratio in Two-Dimensional Materials	51
6.1 Introduction	51
6.2 Experiment Design	52
6.3 Results	54
6.4 Conclusions	59
7 Characterization of Strain Engineered Metal Contact on Monolayer MoS₂	61
7.1 Introduction	61
7.2 Metal-S Interactions	62
7.3 Engineering Interface Roughness	65
7.4 Strain Dependent Interfacial Interactions	66
7.5 Conclusions	73
8 Conclusions	77
9 Outlook	79
Bibliography	102
Acknowledgements	103
Curriculum Vitae	105
Publications	107

List of Figures

2.1	STM images and STS spectra of graphene nanobubbles	10
2.2	Graphene on engineered nanostructures	11
2.3	Photovoltaic device based on indented monolayer MoS ₂	12
2.4	Artificial atom in strained MoS ₂ indented by SiO ₂ nanocones	13
2.5	TMdCs structural phase transition induced by mechanical strain	13
2.6	Strained sulfur vacancies in MoS ₂ basal planes for hydrogen evolution	14
3.1	Design concept of a strain- and gate-controllable STM	18
3.2	Design of strain- and gate-controllable STM sample holder	19
3.3	Design concept of the gearbox	20
3.4	Electrical contact pins for connecting the piezoelectric actuator, V_b , and V_g	21
3.5	Structure of the hexagonal lattice	22
3.6	Compatibility of XPS with the strain- and gate-controllable sample holder	28
4.1	Transfer of the polyimide film	30
4.2	Mass spectra on polyimide film at 96°C, 142°C, and 176°C	31
4.3	Schematic of deposition of metal contacts using a shadow mask	32
4.4	Before and after deposition of Pd clamp on monolayer MoS ₂ /polyimide	33
4.5	Exploded view of step-by-step installation instructions of the strain and gate-controllable sample holder	36
4.6	Photograph of the sample surface before and after indenter approaching	37
5.1	Height controllability of the sample plate and the indenter using gearbox and piezoelectric actuator	40
5.2	Characterization of strain distribution	41
5.3	STM measurement on the graphene transferred on polyimide film	43
5.4	Reversible graphene/polyimide height changes	44
5.5	Characterization of gate-controllability	44
5.6	STM topography images with increasing indenter height	45
5.7	Atomic-resolution image of graphene	46
5.8	Boxplot interpretation	46
5.9	Characterization of strain-controllability	48
5.10	Scatter plots of local graphene lattice points	49
5.11	Bias independence of STM topography images in the tented case	49

List of Figures

6.1	Experimental setup for measuring the Poisson's ratio of 2D materials	53
6.2	Photo of an STM tip-sample junction for Poisson's ratio measurement	53
6.3	Evaluation of lattice parameter changes with increasing uniaxial strain	54
6.4	Atomic resolution STM image of graphene/polyimide under uniaxial strain	56
6.5	Unit length changes of graphene parallel and perpendicular to stretching	57
6.6	Unit length changes of monolayer MoS ₂ parallel and perpendicular to stretching	57
6.7	3D view of local wrinkles in STM topography images of graphene/polyimide	58
7.1	MoS ₂ /Au and MoS ₂ /Pd interfacial interaction.	63
7.2	Absence of modes for 1T phase and defects in the normalized representative Raman spectra of MoS ₂ /HOPG, MoS ₂ /Au/HOPG, and MoS ₂ /Pd/HOPG	64
7.3	Schematic of our method to investigate monolayer MoS ₂ /metal interactions with increasing interface roughness	65
7.4	Surface roughness of Au-deposited with increasing Ar plasma reaction time before and after transferring monolayer	65
7.5	AFM topography images of Au/polyimide before and after transferring the monolayer MoS ₂ with increasing Ar plasma reaction time	67
7.6	AFM topography image of Au/polyimides with increasing Ar reaction time	68
7.7	Overlay images of AFM topography and phase images of MoS ₂ /Au/polyimide	69
7.8	AFM topography and phase images of Au/polyimide and Pd/polyimide with increasing Ar plasma reaction times	70
7.9	AFM topography image of MoS ₂ /Au/polyimide treated with 14 mins Ar plasma	70
7.10	Strain dependence of MoS ₂ /Au interfacial interaction	71
7.11	AFM topography images of Pd/polyimide before and after transferring the monolayer MoS ₂ with increasing Ar plasma reaction time	72
7.12	AFM topography image of Pd/polyimides with increasing Ar reaction time	73
7.13	Overlay images of AFM topography and phase images of MoS ₂ /Pd/polyimide	74
7.14	Strain dependence of MoS ₂ /Pd interfacial interaction	75
9.1	STM images of defects in monolayer MoS ₂ /polyimide	79
9.2	Bandgap histograms and distributions of a Mo vacancy with increasing V _{st} from 0 to 90 V	81

List of Tables

7.1 Summary of the parameters extracted from Raman spectra measured on monolayer MoS ₂ /Au/polyimide and MoS ₂ /Pd/polyimide with various Ar plasma reaction time	68
---	----

Abbreviations

2D	two-dimensional
3D	three-dimensional
AFM	atomic force microscopy
ESE	elastic strain engineering
FFT	fast Fourier transformation
HER	hydrogen evolution reaction
LDOS	local density of states
NPR	negative Poisson's ratio
PI	polyimide
RMS	root mean square
RT	room temperature
STM	scanning tunneling microscopy
STS	scanning tunneling spectroscopy
TMdCs	transition metal dichalcogenides
UHV	ultra high vacuum
V_b	sample bias voltage
V_g	gate voltage
V_{st}	piezoelectric actuator voltage
XPS	X-ray photoelectron spectroscopy

1 Introduction

A material changes its size in response to an external force. In case of crystalline materials, the force supplies the requisite energy for changing the length of atomic bonds inside the lattice structure. Since the lattice structure is responsible for determining a material's properties, deformation signifies not only a change of size but also concurrent changes in all properties.

Compared to 3D bulk materials, 2D materials exhibit increased susceptibility to deformation. When supported by a substrate, deformation is induced by surface morphology, resulting in out-of-plane bending strain [1], or by lattice mismatch, which causes a moiré pattern with an in-plane periodic strain distribution [2, 3]. Even when suspended, 2D materials display a complex landscape of corrugations rather than a simple planar surface [4], incorporating substantial built-in elastic strain. As a consequence, it is essential to consider strain effects when investigating various phenomena and properties of 2D materials or their utilization in the development of future straintronics.

2D materials, such as monolayer TMdCs, feature atomic-scale thickness, sizable electronic bandgap, and strong spin-orbit coupling [5]. Furthermore, due to their superior flexibility, they are able to endure strain up to 10% before breaking [6]. Strain can modulate various properties such as the bandgap [1, 7], spin-orbit coupling [8], thermal conductivity [9, 10], effective masses of charge carriers [11], the energy barriers for structural phases [12, 13] and the catalytic efficiency for hydrogen evolution reactions [14, 15]. Moreover, an electrostatic gate can control the charge-carrier concentration and mobility of 2D materials [16]. The simultaneous application of strain and doping may drive the phase transition from the thermodynamically stable 2H phase to other phases, such as 1T' [17], H' [18], or 1S phases [19], with the reduced transition energy barrier [12, 13]. Each phase has its unique properties, such as direct optical bandgap [20], chemical reactivity [21], or non-trivial topological states [17]. As a result, monolayer TMdCs with ample scope for elastic strain engineering are good candidates for developing future applications such as flexible electronics and optoelectronics [22–24], mountable physiological monitoring devices [25, 26], flexible energy storage systems [27–31], and catalysis [32–35].

Optical methods such as Raman spectroscopy and photoluminescence are routinely employed to characterize strain effects on 2D materials [36]. By using a bending apparatus with a 2D material transferred onto a flexible substrate, strain can be inferred from the physical geometric structure and compared with the strain-induced change in the spectrum [37, 38]. However, optical methods suffer from limited spatial resolution, with observed strain effects being averaged over a finite beam size of around half a micrometer. Given that strain varies at the nanoscale, the direct observation of the electronic structure at the atomic scale is required to characterize the impact of strain on individual atoms. In this regard, STM is an ideal tool for understanding strain effects at the atomic level. STM allows us to obtain atomic-resolution images of the lattice structure of 2D materials, and STS enables the measurement of their local density of states. The use of STM in this manner allows the strain on 2D materials to be calculated by the length changes in lattice constants and then be compared with and directly correlated with their band structures.

Numerous strategies have been implemented to apply strain to 2D materials for STM measurements. Some approaches involve patterning the substrate with tailored nanostructures [39, 40] or millimeter-sized wedges [41], which can apply a strain up to 3% to 2D materials. Additionally, an electromechanical device controlled by the piezoelectric effect can be used to apply a uniform and controllable biaxial compressive strain of up to 0.2% to trilayer MoS₂ [42]. Another method involves gluing bulk crystals of 2H-MoSe₂ onto two ends of a movable bridge controlled by piezoelectric devices, which can apply a uniaxial strain of around $\pm 3\%$ [43]. However, the technical limitations of these approaches have constrained the amount of strain that can be applied. To overcome these limitations and achieve greater control over the application of strain, a dual-probe STM setup has been developed and used to directly measure the deformations induced by one STM probe on free-standing few-layer graphene, providing a way to apply strain until 2D materials break [44, 45]. Nonetheless, this approach has posed challenges for monolayer samples due to the challenge of maintaining stability. As a result, the integration of STM with strain-controllable devices for atomic-scale thickness 2D materials has not been realized, owing to the stringent requirements for compatibility with cryogenic temperatures, ultra-high vacuum, and mechanical stability.

In this thesis, I present the development of a new nanoindentation system for subjecting 2D crystals to controllable strain and gating inside the low temperature STM. Employing this technique, I examined the strain response of 2D materials, including monolayer MoS₂ and graphene, with atomic precision. The thesis is organized as follows: Chapter 2 reviews the progress of strain engineering from the 3D semiconductor industry to 2D materials such as graphene and monolayer MoS₂. In Chapter 3, I explain my design concept for the nanoindentation system and the working principle of STM, as well as other experimental systems, including XPS, AFM, and Raman spectroscopy, used throughout this thesis. The analysis for lattice parameters and local curvature for calculating the strain is also presented. Chapter 4 details our methods for transferring polyimide, metal deposition, and the usage of the strain- and gate-controllable STM sample holder. Chapter 5 demonstrates the performance of the strain- and gate-controllable STM sample by examining the strain response of monolayer

MoS₂ and graphene from both the macroscopic scale using AFM and Raman spectroscopy and from the atomic scale using STM. Chapter 6 continues to present our experiments to measure the Poisson's ratio of 2D materials, including graphene, and monolayer MoS₂, by modifying the shape of the indenter to deform 2D materials in the uniaxial direction. In addition to STM results obtained from the nanoindentation system, Chapter 7 presents my work on engineering the strain applied to monolayer MoS₂ by controlling the contact metal surface roughness to characterize the interface interactions and contact behaviors. Finally, I conclude the thesis and provide a future research outlook and discuss the challenges associated with measuring local spectroscopy.

2 Background

The manipulation of lattice structure profoundly influences the physical and chemical properties of crystalline materials. Even small variations in the lattice parameters, as little as 1%, can substantially affect the material's behavior. Based on this concept, strain engineering has emerged as a potent technique for tailoring the properties of materials, enabling the transformation of conventional materials into artificially engineered ones with optimized or unusual properties distinct from their strain-free states [46].

In the semiconductor industry, strain engineering has revolutionized electronic device design and fabrication, enhancing performance and functionality [47, 48]. Strained silicon technology, for instance, has significantly contributed to non-classical scaling, which has delayed Moore's Law over the past two decades [49, 50]. The band structure modification in strained silicon resulted in a reduction of the effective mass of charge carriers, leading to a remarkable enhancement of carrier mobility by several hundred percent [51]. Although such piezoresistance effect was demonstrated as early as 1954 [52], it was not until the early 2000s that mass-scale production was realized [53]. In addition to transistors, strain engineering in 3D semiconductors has also found extensive applications in lasers, detectors, and various optoelectronic devices [47, 54, 55].

Recently, strain engineering has been extended to encompass 2D materials, which exhibit unique and attractive electronic, mechanical, magnetic, optical, and catalytic properties, all of which can be further enhanced through strain manipulation. Various techniques have been developed for applying strain to 2D materials and characterizing the strain effects. Furthermore, the potential for designer stacking and twisting 2D materials in their van der Waals heterostructures can be exploited to create much richer and more exotic deep elastic strain engineering than that of 3D materials [46].

This chapter provides an overview of strain engineering, reviewing techniques, and strain effects, beginning with those from the 3D semiconductor industry and extending to the 2D materials, with a focus on graphene and monolayer MoS₂. Subsequently, we will see that through the development of synthesis methods, strain application, characterization of strain

distribution, measurements of local strain-induced properties, and theoretical predictions, researchers have attained unprecedented control over the physical and chemical properties of these atomic sheets. This controllability has unveiled exciting opportunities for applications across a broad spectrum of scientific and technological fields.

2.1 Strain Engineering in 3D Semiconductor Industry

The semiconductor industry has had a significant impact on the global economy. It has undergone remarkable technological advancements in the past six decades, resulting in the development of smaller and more powerful electronic devices. Moore's law has quantified the progress of silicon complementary metal-oxide-semiconductor (CMOS) field-effect-transistor (FET) technology, describing how the number of transistors on a given area of silicon doubles with each technology generation on a one to two year cycle. However, as the technology roadmap approaches its limit, conventional structures and processes for down-scaling CMOS transistors are becoming increasingly challenging to implement. Additionally, aggressive down-scaling of transistors leads to an increase in power density, off-leakage current, and carrier mobility degradation.

Strain engineering is one of the promising techniques for further enhancing device performance beyond the limits of conventional scaling [48, 50, 56]. Strain can modify the silicon band structure to reduce the effective mass of charge carriers, leading to a remarkable mobility enhancement by several hundred percent [51]. Innovative techniques such as compressive and tensile stressed silicon nitride top layers [57], global biaxial strain [58], local uniaxial strain by stressors [59], and even strain induced by defects [60] have been developed and incorporated into conventional CMOS technology. Among these techniques, epitaxial growth has proven to be the most successful approach, allowing for direct engineering of the lattice parameter on the starting substrate prior to device fabrication. The GeSi alloy system, in particular, offers precise control of the lattice parameter by regulating the composition during epitaxial growth, ranging from that of Si (0.357 nm) to that of Ge (0.356 nm). This method enables subsequent layers of Si grown on relaxed GeSi alloy layers to experience biaxial tensile strain. This global strain approach offers significant advantages, including well-controlled magnitude and uniformity of strain and the use of standard device fabrication steps, resulting in significant improvements in both electron and hole mobility [58, 61].

Alternatively, process-induced local strain can be applied in the channel region by selective epitaxy growing strained GeSi layers as a stressor material within the source/drain regions. The resultant uniaxial compressive strain to the Si channel region has led to a 50% improvement in hole mobility [53]. As semiconductor technology has progressed, various strategies have been employed to further enhance this uniaxial process-induced strain, including increasing the Ge content, positioning the GeSi stressor toward the channel, altering the recess geometry, or utilizing strained gate material [62]. Due to diminishing effectiveness of localized stressors with each successive technology generation, a combination of biaxial and uniaxial strain in

the Si channel has also been employed through the conversion of biaxially strained layers via elastic relaxation [63], providing an effective way for future scaling in the sub 10nm regime.

2.2 Strain Engineering in 2D Materials

Elastic strain engineering (ESE) is an innovative approach that has gained considerable attention in the field of strain engineering, particularly for its potential applications in 2D materials [64]. Unlike brittle bulk crystals, where bulk defects and surface imperfections limit the ultimate strain, the atomic thickness and in-plane covalent bonding of 2D materials render them highly resistant to inelastic relaxation and amenable to an increased strain and, therefore a wider ESE process space. ESE facilitates flexible, continuous, and reversible modulation of material properties and even results in the emergence of unprecedented functionalities. Furthermore, the large strain in 2D materials can lead to phenomena such as the pseudo-magnetic field in highly strained graphene [65], and the phase transition in transition-metal dichalcogenides [12].

In 2D materials, the atomically thin nature allows for the implementation of various strategies to introduce strain. Lattice mismatch, for instance, can be employed in lateral or in-plane heterostructures. In monolayer WSe_2 - MoS_2 lateral heterojunctions, both tensile and compressive strain can be induced in the epitaxial MoS_2 region [66]. For in-plane WSe_2 - MoS_2 heterojunctions, Moiré patterns emerge with strain distributions induced by lattice mismatch. Such strain resulting from lattice mismatch is inhomogeneous, with the highest concentration at the center of the mismatched interface, gradually decreasing farther from the interface [67].

Owing to the van der Waals forces between 2D materials and substrates, unwanted bubbles can emerge at the interface through the aggregation of water and hydrocarbons during the assembly process [68]. These bubbles give rise to surface fluctuations in 2D materials, which induce out-of-plane strain. Alternatively, they can be generated deliberately by modulating the pressure differences in 2D materials suspended on the cavity [69, 70]. The 2D material exhibits either upward or downward bulging, corresponding to tensile or compressive biaxial strain. The pressure can be well controlled, allowing for continuous and reversible strain.

Flexible substrates have aroused great interest in inducing strain in 2D materials because such a combination can be used to develop flexible electronics [5]. For instance, wrinkles can be produced by pre-stretching flexible substrates with different elastic moduli than 2D materials [2, 71]. The strain induced by wrinkles is inhomogeneous, with the highest concentration at the hills or valleys, typically ranging from 1-2%, depending on the radius of curvature [72, 73]. On the other hand, stretching strain can be induced by heating flexible substrates with higher thermal expansion coefficients than 2D materials [74], although the induced strain could gradually release as temperature decreases or during long-term sample storage. Additionally, flexible substrates can transfer the strain to 2D materials through mechanical bending using a two-point or four-point fixing apparatus [37, 75]. The induced bending strain is uniaxial and homogeneous and can be controlled precisely and reversibly within a critical range of 0.6-3.2%

Chapter 2. Background

[37, 38, 75–81]. The use of polymers with high Young's modulus is preferred as it increases the strain transfer efficiency [82, 83]. Nonetheless, the weak van der Waals forces may cause the slippage of 2D materials during the bending processes [79]. Therefore, it is important to clamp the edges of 2D materials by either metal deposition [78] or chemical bonding [79] when inducing larger strain.

Piezoelectric substrates represent another method for precisely inducing strain by controlling the applied electric field [84]. This can be achieved by using the deformation caused by the Poisson's effect in the plane perpendicular to the field, subsequently producing a uniform biaxial strain in 2D materials. However, the maximum strain achieved remains limited to around 0.2% due to the small travel range of piezoelectric components [42]. Analogous to the bending method using polymers, this structure also requires an interface interaction to achieve a larger strain transfer efficiency. To fully exploit the limited travel range, 2D materials can be utilized as a bridge connecting two movable piezoelectric parts, thereby applying a uniaxial strain of up to $\pm 3\%$ [43].

Transferring 2D materials onto patterned substrates is also widely used to induce strain. Techniques such as ion-beam sputtering, photolithography, electron-beam etching, and self-assembly have been employed to modify the surface of either flexible or rigid substrates, resulting in the formation of unique surfaces exhibiting periodic ripple [85], nanocone [86], or nanopillar [87–89] structures. Utilizing patterned substrates has the advantage of maintaining 2D materials in a consistent local strained configuration, facilitating scalable production or characterization methods [90]. Furthermore, the bending strain is closely related to the morphology of the patterned substrates, allowing for engineering the strain-induced properties by altering nanostructure patterns [91].

AFM has been used to induce strain in 2D materials through local deformation resulting from direct tip-sample contact, so-called nanoindentation [6, 92]. Typically, this method involves suspending 2D materials onto the holey surface of a rigid substrate with a carefully designed structure. This approach offers a unique opportunity to apply strain to 2D materials until they eventually fracture. However, it should be noted that the induced strain is highly localized and inhomogeneous, occurring predominantly around the indenter area [92]. While the scalability of this method may pose a challenge, it remains a valuable approach for characterizing the effect of high strain on 2D materials.

The aforementioned methods, ranging from lattice mismatch, bubbles, bending, piezoelectric and patterned substrates to nanoindentation, can further synergize with other techniques, including defect engineering [93, 94] and doping engineering [95]. Moreover, they can combine with the recent van der Waals heterostructure engineering, such as controlling the number of layers, stacking materials, and twist angles [96–98], to optimize the emergent physical phenomena in 2D materials. Such a wide range of uses of elastic strain engineering opens up endless possibilities for tailoring material properties.

In the following sections, I will continue to review the strain-induced changes and phenomena in 2D materials by taking graphene and monolayer MoS₂ as two classic examples.

2.2.1 Graphene

Ever since the isolation of graphene, an atom-thick layered form of graphite, by Novoselov and Geim in 2004 [99], graphene and its derivatives have provided groundbreaking insights, such as being the strongest material ever discovered [92], having high electron mobility [99] and thermal conductivity [100], and exhibiting quantum hall effects [101]. In recent years, research into twisted bilayer graphene has continued to reveal intriguing collective electronic phases, such as correlated insulating states [102], superconductivity [103], and ferromagnetism [104], among others. Applications for graphene have been diverse, encompassing supercapacitor development [105, 106], incorporation into composite material [107], cancer treatment [108–110] and flexible sensors [111].

The impact of strain on a multitude of graphene properties has been extensively explored. For instance, it has been shown that tensile strain leads to softening of the in-plane phonon mode, which is the critical factor in decreasing graphene thermal conductivity [112]. This softening causes a reduction in phonon group velocities, with the most significant decrease observed under biaxial tensile strain. Conversely, tensile strain causes the stiffening of out-of-plane phonon modes with a decrease in phonon scattering, which is manifest in the thermal conductivity of strained graphene [113].

Strain can also affect the Raman spectra of graphene [114]. In the case of uniaxial strain, a reduction in graphene's symmetry would result in the splitting of the Raman modes, for example G band [38]. The two split G bands exhibit distinct shift rates relative to each other and also depend on the strain applied along either the armchair or zigzag direction [115]. In contrast, under biaxial strain, only redshifts have been observed due to the preservation of graphene's symmetries [116].

Additionally, theoretical predictions have indicated that combining charge carrier doping of $5 \times 10^{14} \text{ cm}^{-2}$ with a biaxial tensile strain of 12% can substantially enhance electron-phonon coupling by softening the phonon modes, thereby transforming graphene into a BCS superconductor with a critical temperature of $\sim 30 \text{ K}$ [117].

Alternatively, strain has been proposed as an effective approach to facilitate the self-assembly of adsorbed hydrogen atoms on graphene [118, 119]. Compressive strain-induced ripples in the graphene lattice increase the chemical reactivity of carbon atoms situated in regions with high curvature. These specific sites become preferential for hydrogen adsorption, and this principle can be extended to the self-assembly of other adatoms, including F, Cl, and O [120].

One of the drawbacks of graphene, however, is the lack of an inherent energy gap in graphene, which limits its use in semiconductor applications such as transistors and optoelectronic components. Consequently, generating a controllable gap in graphene has been a long-

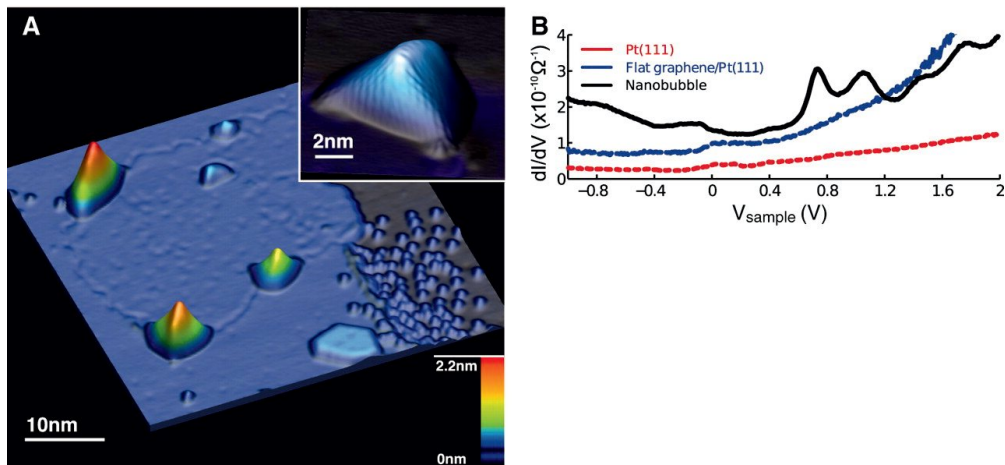


Figure 2.1: STM images and STS spectra of graphene nanobubbles. (a) Graphene monolayer patch on Pt(111) with four nanobubbles at the graphene-Pt border and one in the patch interior (Inset). (b) STS spectra of bare Pt(111), flat graphene on Pt(111), and the center of a graphene bubble. Reprinted from [65].

standing objective, pursued through various approaches, including substrate interactions [121, 122], surface adsorption [123, 124], defects [125, 126], or strain [127]. For the direct strain method, a significant uniaxial strain of $\sim 23\%$ along the zigzag direction is required to create a gap, which poses a practical challenge. An alternative strategy for introducing a gap in graphene involves designing a non-uniform strain distribution, which can lead to an effective gauge field in graphene, generating a pseudomagnetic field and subsequently resulting in Landau quantization and quantum Hall effect-like states [114, 128]. With finite doping, graphene transitions from semimetallic to semiconducting with an insulating bulk state when the Fermi level lies between the Landau levels. Initial experimental evidence of pseudomagnetic fields induced by nonuniform strain fields in graphene nanobubbles formed on a Pt(111) surface was obtained through STM/STS (Fig. 2.1) [65]. STS measurements over the nanobubble regions revealed a series of distinct peaks separated by over 100 meV. Fitting the STS spectra analogously to Landau levels in a real magnetic field yielded a uniform pseudomagnetic field of approximately ~ 350 T.

Subsequent advancements were achieved by placing graphene on engineered nanostructures [91, 129]. One of these demonstrations was made by transferring the graphene/hBN onto a silicon surface with Pd tetrahedron nanocrystal (Fig. 2.2). In principle, this technique can generate giant pseudomagnetic fields of up to ~ 800 T, slow carrier dynamics, valley polarization, and periodic one-dimensional topological channels for the protected propagation of chiral modes. In comparison to randomly formed bubbles or wrinkles due to thermal expansion mismatch, this method offers several advantages including room temperature compatibility, promising optimization of strain, and long-term stability. This strain engineering approach for manipulating graphene's pseudomagnetic field properties lays the foundation for scalable graphene-based electronics [130–133].

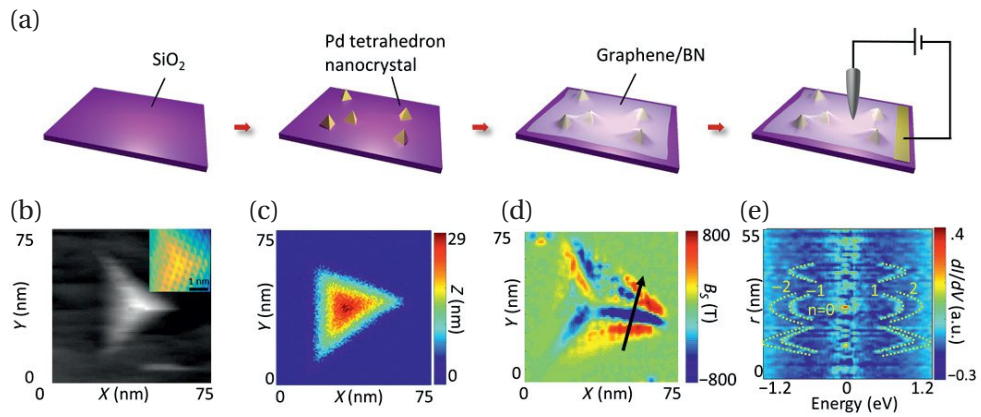


Figure 2.2: Graphene on engineered nanostructures. (a) Fabrication process. (b) AFM and atomic resolution STM (inset) images of the distorted graphene. (c) STM images of the distorted graphene. (d) Pseudo-magnetic field map calculated from the topography. (e) Tunneling conductance spectral difference relative to the Dirac spectrum of strain-free graphene. Reprinted from [91].

2.2.2 Monolayer MoS₂

In the process of trying to overcome the disadvantages of graphene, monolayer MoS₂ has emerged as a popular subject of research, primarily due to its bandgap. It features additional attractive properties, such as control over the bandgap, direct optical bandgap and strong spin-orbit coupling [5, 134] and so on. Its superior flexibility also makes it a promising candidate for strain engineering, with the ability to endure strain up to 10% before breaking [6]. Similar to graphene, strain can modulate the thermal conductivity of monolayer MoS₂ [9, 10]. Experimental and theoretical studies have demonstrated that monolayer MoS₂ under tensile strain displays an observable redshift in the in-plane phonon peaks and a positive Grüneisen parameter, which indicates a reduction in thermal conductivity [37]. Moreover, the strain-induced modification of the effective masses of charge carriers [11] in monolayer MoS₂ has been characterized for its potential application as a channel material in developing next-generation transistors. The reduced energy gap between conductive bands in Brillouin zone space induced by strain decreases the intervalley phonon scattering, which in turn enhances the mobility of the charge carriers [135].

The significant effect of strain on the interactions and hybridizations of the transition metal *d* orbitals and sulfur *p* orbitals has made it an effective strategy for engineering the bandgap structure and modulating the excitonic behavior [1, 136]. Specifically, the bandgap is observed to decrease under tensile strain [1]. Remarkably, since the direct gap in monolayer MoS₂ is only slightly lower in energy than the indirect gap, relatively small tensile strains (~2%) can induce a direct to indirect gap transition, as demonstrated by photoluminescence spectra [137].

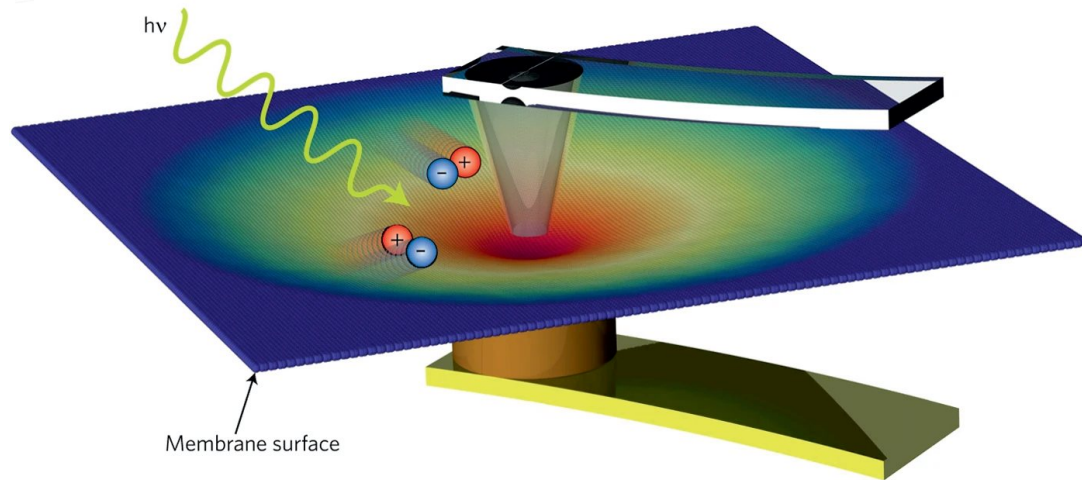


Figure 2.3: Photovoltaic device based on indented monolayer MoS_2 . Non-uniform strain is induced using an AFM probe at the center of the membrane. Incident light on the membrane creates photogenerated electron–hole pairs that drift towards the region of most strain where they are separated and travel to two electrodes, thus generating electricity. Reprinted from [138].

It has been proposed that this strain-tunable bandgap could be exploited in a broad spectrum solar energy funnel by using nanoindentation to apply non-uniform strain. Exploiting this [139], the non-uniform strain distribution induces a spatial variation in the bandgap, which facilitates the absorption of a wide range of solar photons (Fig. 2.3). Furthermore, the $1/r$ -like deformation potential results in a funneling effect so that neutral excitons are concentrated toward the center with a reduced probability of recombination. Such tunable artificial optoelectronic material is highly desirable for use in photovoltaics, photocatalysis and photodetection [140].

The concept of a strain-induced exciton funnel was later realized experimentally by employing capillary-pressure-induced nanoindentation in monolayer MoS_2 through a tailored nanopattern (Fig. 2.4) [39]. This technique generates a spatially varying biaxial strain within the monolayer MoS_2 . Under this strain distribution, the band gap of MoS_2 undergoes significant variations, expanding the absorption bandwidth from 677 nm (unstrained MoS_2) to 905 nm (highly strained MoS_2). This wider range covers the entire visible wavelength spectrum and most of the solar spectrum's intense wavelengths, thereby forming an artificial optoelectronic crystal. This innovative structure promotes broadband light absorption and optimizes the funneling of photogenerated excitons towards areas of maximum strain located at the nuclei of the artificial atoms. Although this achievement is already groundbreaking, it is worth noting that the strains have not yet reached their breaking limits, suggesting that even larger band gap variations could potentially be incorporated into such artificial crystals. This innovative approach represents a novel class of materials with potential applications in next-generation optoelectronics and photovoltaic technologies [23].

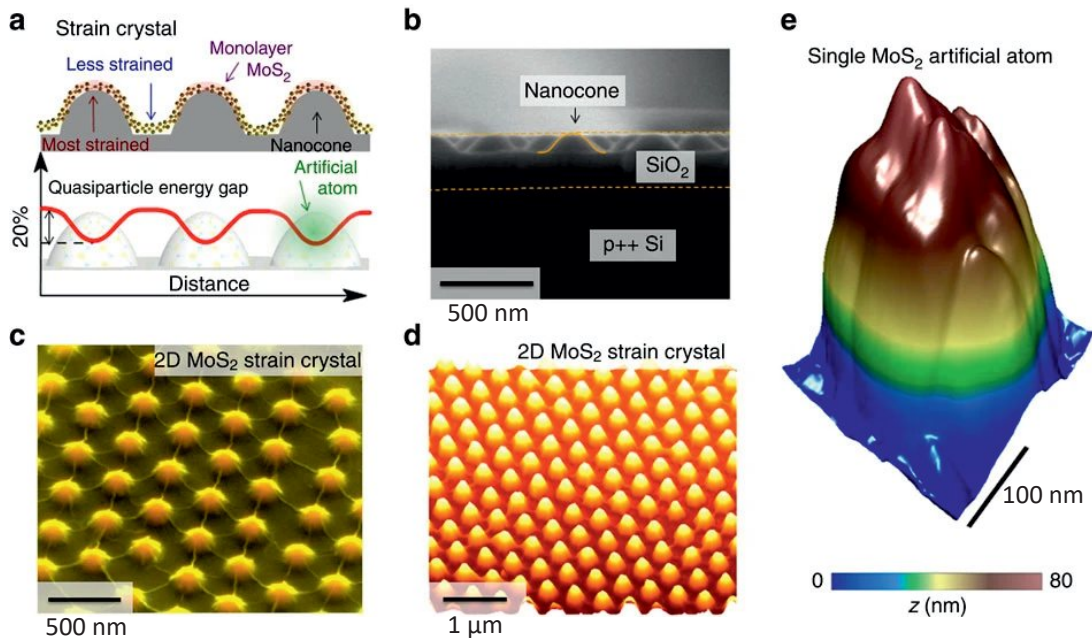


Figure 2.4: Artificial atom in strained MoS_2 indented by SiO_2 nanocones. (a) Schematic. (b) Cross-sectional scanning electron microscopy (SEM) image of the nanocone substrate. (c) Tilted false-color SEM image of the 2D strained MoS_2 crystal defined by the nanocone array. (d) AFM topography of the 2D MoS_2 strain crystal. (e) STM topography of a single 'artificial atom' building block within the crystal. Reprint from [39].

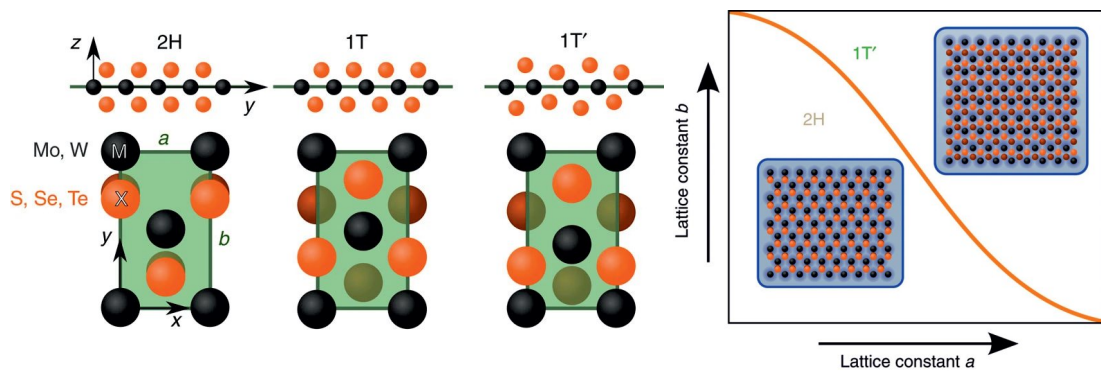


Figure 2.5: TMdCs structural phase transition induced by mechanical strain. All three phases consist of a metal (Mo or W) atom layer sandwiched between two chalcogenide (S, Se or Te) layers. Each can be represented in a rectangular unit cell with dimensions $a \times b$. (b) One way in which the lattice parameters a and b of an MX_2 monolayer may be tuned is by virtue of an underlying substrate. Reprint from [12].

Chapter 2. Background

Monolayer TMDs can exist in multiple crystal structures, such as 2H, 1T' [17], 1H' [18], or 1S phases [19]. Each phase has its unique properties, for instance, direct optical bandgap in 2H [20], chemical activity in 1T' [21], or non-trivial topological states in 1H' and 1S [17]. It has been theoretically shown that mechanical deformations provide a promising route to reversibly switching thermodynamic stability between a semiconducting and a metallic crystal structure (Fig. 2.5) [12]. Importantly, the value of the predicted strain is attainable in the existing strain methods. Combining the strain with electrostatic doping may drive the transition to other phases with a reduced barrier [13]. As a result, the potentially accessible multiple phases of monolayer MoS₂ open up further possibilities for elastic strain engineering [141].

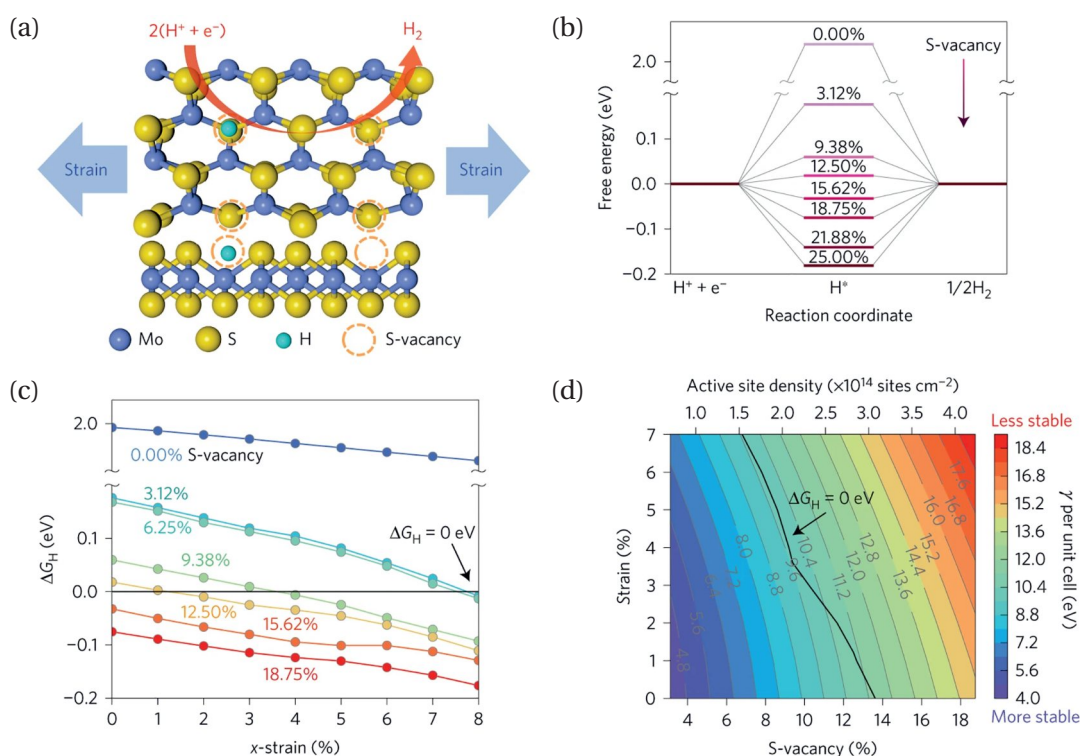


Figure 2.6: Strained sulfur vacancies in MoS₂ basal planes for hydrogen evolution. (a) Schematic of the top (upper panel) and side (lower panel) views of MoS₂ with strained S-vacancies on the basal plane, where S-vacancies serve as the active sites for hydrogen evolution and applied strain further tunes HER activity. (b) Free energy versus the reaction coordinate of HER for the S-vacancy range of 0-25%. (c) ΔG_H versus %x-strain for various %S-vacancy, ranging from 0.0% (pristine) to 18.75%. (d) Colored contour plot of surface energy per unit cell γ (with respect to the bulk MoS₂) as a function of S-vacancy and uniaxial strain. Color bar represents the value of γ . The black lines in c and d indicate combinations of S-vacancy and strain that yield $\Delta G_H = 0$ eV, the optimal thermodynamic requirement for HER activity. Reprinted from [14].

Monolayer MoS₂ has been the focus of considerable attention in the energy field due to its electronic and optoelectronic properties, as well as its potential as a catalyst for the hydrogen

evolution reaction (HER) [14, 15]. HER reaction is crucial for producing sustainable and environmentally friendly energy, necessitating the development of highly efficient and cost-effective catalysts to replace Pt-based materials [142]. The edges of MoS₂ have long been known as the active sites for HER [32, 33, 143–145]. In addition to edge sites, it has been theoretically predicted and experimentally verified that the basal plane can also be activated by introducing defects, and then the efficiency can be further optimized by elastic strain [14], acting as a highly active and tunable catalytic site (Fig. 2.6). This enhancement of catalytic activity is attributed to the introduction of new bands by S-vacancies and the reduction of the bandgap under strain. It has also been found that biaxial tensile strain can enhance HER activity more effectively than uniaxial tensile strain, while compressive strain decreases HER activity [146]. Taking advantage of the basal plane, previously thought inert, presents a huge breakthrough because it enables an increase in active site density with one additional dimension. By employing the strain as an additional tool for optimization, the structure can maintain long-term stability with only a negligible decrease in catalytic activity over numerous cycles. Additionally, 1T-phase MoS₂, which can be produced by chemical exfoliation or strain, has also proven to be effective for catalysis [34]. Therefore, the elastic strain engineering of catalytic activity of monolayer MoS₂ for the HER process offers significant potential for advancing efficient and cost-effective catalysts [147].

2.2.3 Remark

To date, the atomic scale examination of the effect of strain on various material properties has significantly enriched our understanding, although published work is limited. This insight has helped to inform the development of methodologies aimed at enhancing control over the diverse properties of these atomically thin layers.

In the forthcoming stage of research, it would be highly advantageous to acquire the capacity to perform direct characterization of the strain response in 2D materials at the atomic scale, extending elastically and reversibly up to their fracture limits. Although achieving this goal may be challenging due to the inherent difficulties in simultaneously maintaining flexibility and mechanical stability at low temperatures within UHV environments, such measurements would yield invaluable insights, paving the way for advancements in the field of elastic strain engineering.

3 Experimental Methods

This chapter provides the reader with design principles of the strain- and gate-controllable STM sample holder, the basics of STM, AFM, XPS, and Raman spectroscopy, which are used in this thesis, and detailed descriptions of our analysis method to derive strain from changes in local lattice parameters and curvatures.

3.1 Scanning Tunneling Microscopy

Basics

The working principle of STM relies on a simple concept: a single-atom-sharp metallic tip is positioned in close proximity to a sample surface with a V_b applied between the tip and the sample. As the tip-sample distance approaches atomic dimensions (a few Å), electrons jump between the tip and the sample, generating a tunneling current. This current is highly sensitive to the tip-sample distance, exhibiting an exponential dependence. For instance, in a clean vacuum tunnel junction, the tunneling current decreases by one order of magnitude when the tip-sample distance is increased by 1 Å. This characteristic endows STM with its atomic-scale lateral spatial resolution, as most of the tunneling current originates from the terminal atom at the tip apex. Consequently, STM is also highly vulnerable to vibration and electronic noise due to the small measured current (a few pA to nA).

By maintaining a constant tunneling current while scanning an unknown surface and adjusting the tip's height through a feedback loop, STM generates a 3D surface image. However, interpreting STM images is not a straightforward process because the tunneling current is influenced by both (1) the exponential dependence of the tip-sample distance and (2) the contribution of the LDOS from the sample and the tip. As such, the tunneling current conveys convoluted information about the actual surface contour and the electronic configuration of the tip-sample system. Therefore, it is crucial to compare the observed features with known crystal structures or theoretical models of the material under investigation for image interpretation.

Another notable feature of STM is its unique capability of performing local spectroscopy, commonly called scanning tunneling spectroscopy (STS). STS can be conducted by fixing the tip at a specific position on the surface and measuring the current as a function of V_b . The differential conductance (dI/dV) curve represents the samples' electronic structure, reflecting electron tunneling to the unoccupied electronic states above the Fermi level or tunneling from the occupied electronic states below the Fermi level. Therefore, STS is a powerful tool for investigating the LDOS of a sample. Operating the STM at lower temperatures leads to STS with enhanced energy resolution, owing to the reduced thermal broadening of electrons in both the tip and the sample and improved stability.

For a comprehensive review of STM, please refer to [148–151].

Setup

Our home-built UHV STM working at ~ 4.8 K is constructed in Precision Laboratory in Max Planck Institute for Solid State Research, Stuttgart, Germany, with a hugely reduced vibration noise [148]. STM is communicated by Nanonis (Generic 5) and is operated in the constant current mode throughout this thesis. The dI/dV spectra are recorded using a lock-in technique with a modulation amplitude and frequency of 10 nV and 317 Hz, respectively. STM tip is fabricated from the straight W wire with a diameter of 0.25 mm using an electrochemical etching method [152]. Before introduction into STM, the tip is outgassed and then e-beam heated to remove surface oxide in the preparation chamber. In-situ tip treatment is performed before STM data acquisition.

3.1.1 Strain- and Gate-Controllable Sample Holder

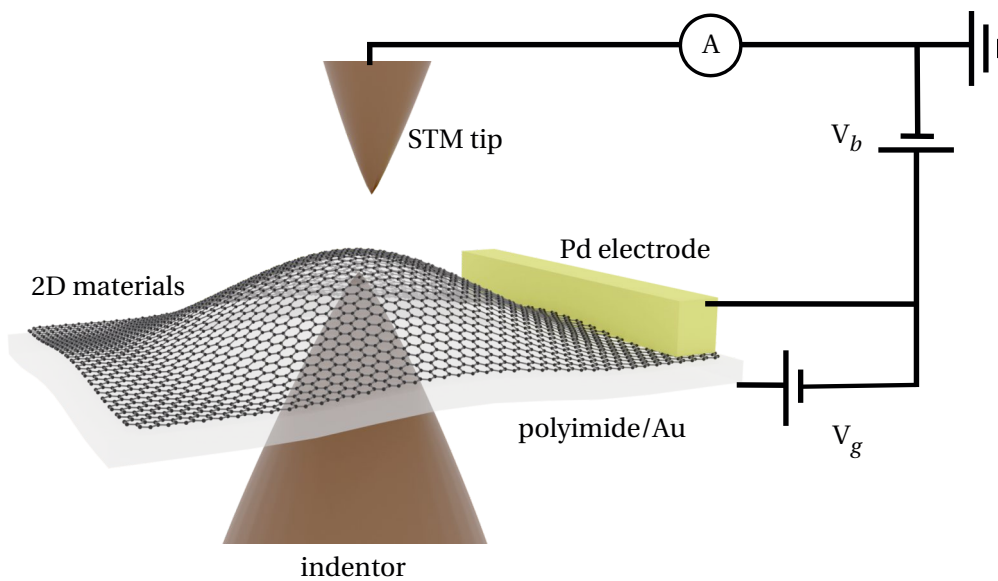


Figure 3.1: Design concept of a strain- and gate-controllable STM.

I have designed and developed a new STM sample holder to subject 2D crystals to controllable strain and gating. Its working principle is based on the nanoindentation method [92, 153] (Fig. 3.1). 2D materials are transferred using the wet etching method [154] onto a flexible polyimide film and fixed, and then controllably deformed by the application of an indenter. The polyimide film with a thickness of $\sim 1 \mu\text{m}$ also served as the dielectric to enable the electrical gating of the 2D materials. To form a gate structure, a Au layer is deposited at the bottom of the polyimide film as a back contact, and a Pd electrode is deposited at the edge of 2D material.

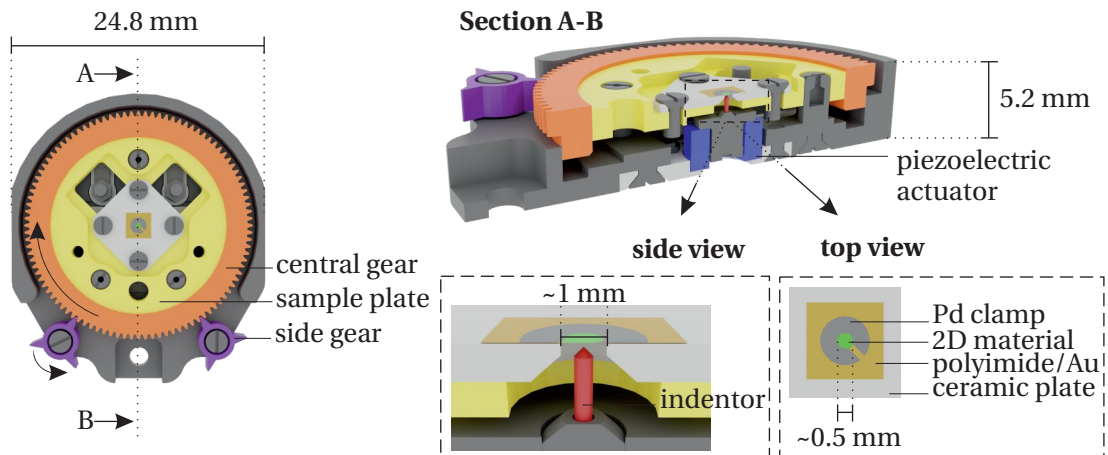


Figure 3.2: Design of strain- and gate-controllable STM sample holder.

Fig. 3.2 shows the CAD schematic overview of our strain- and gate-controllable STM sample holder. The basic principle of the strain application follows. An electrochemically etched W tip is mechanically ground with an apex radius of a few μm (red) and used as an indenter to exert force on the 2D material (green). The 2D material is first transferred onto a polyimide film with a thickness of $\sim 1 \mu\text{m}$. Then, the 2D material/polyimide film is transferred and glued to the ceramic sample plate with a central $\sim 1 \text{ mm}$ diameter circular aperture. The height of the sample plate is controlled by the gearbox, while the height of the indenter is controlled by the piezoelectric actuator. The strain is applied by controlling the relative positions between the sample and the indenter by either lowering the sample plate or raising the indenter. The keyhole-like Pd clamp with an inner diameter of $\sim 0.5 \text{ mm}$ and a thickness of $\sim 30 \text{ nm}$ deposited at the edges of the 2D material enables efficient strain transfer from the polyimide film [78].

Combining a gearbox and a piezoelectric actuator enables a large travel distance with high precision. A gearbox (orange and purple) is positioned inside the sample holder body (grey). The gearbox design is based on a "differential adjusting" concept, as shown in Fig. 3.3. The central gear (orange) has 100 teeth; its thread pitch at the outer and inner sides are 0.30 and 0.25 mm/revolution, respectively. As the sample plate (yellow) is not rotatable, the central gear moves unequally in the opposite direction to the sample plate. Therefore, the sample height, which depends on the difference between the central gear's inner and outer thread pitch, can be precisely controlled.

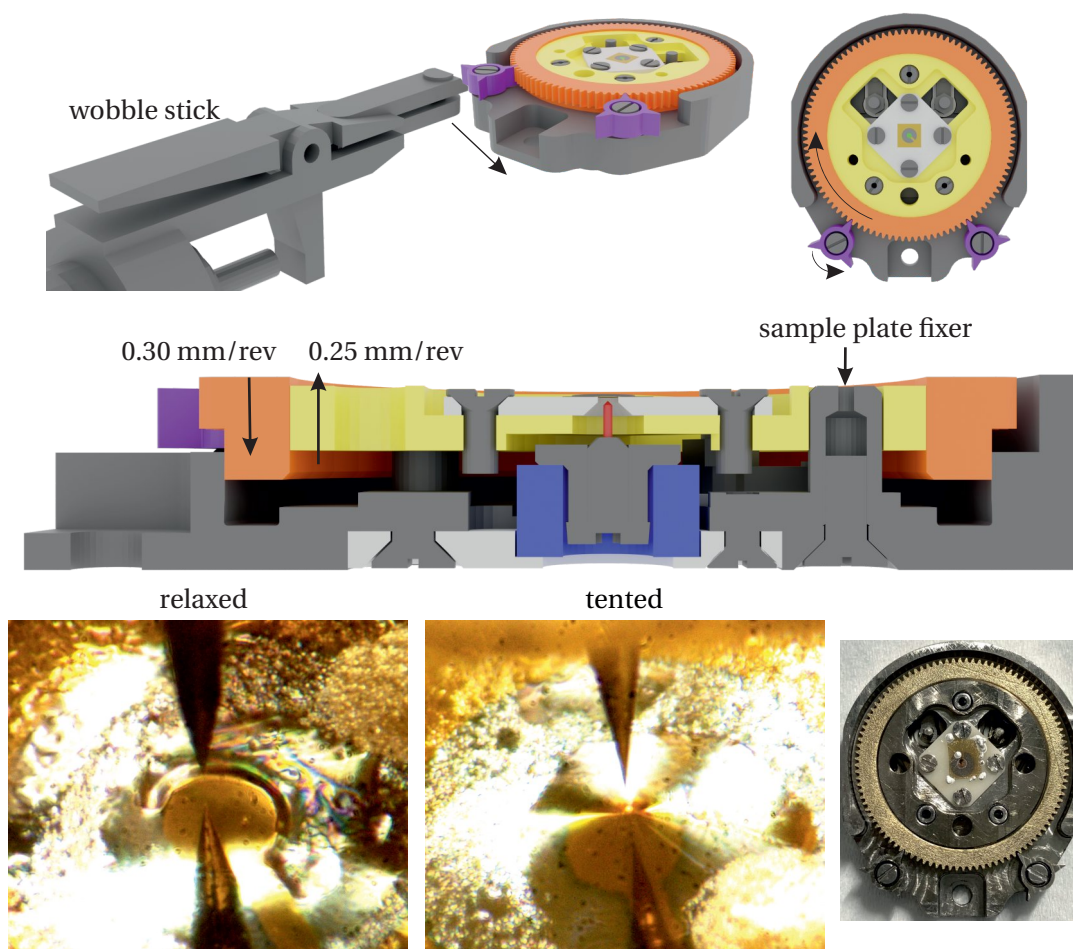


Figure 3.3: Design concept of the gearbox. The concept of differential adjusting is adopted to enhance the precision of control. Rotation of the gearbox system is controlled by using a wobble stick in situ inside the chamber. Relaxed and tented sample conditions at ~ 4.8 K. The photograph of the assembled sample holder is shown in the bottom right.

Two side gears (purple), with three separated teeth that partly protrude outside the sample holder body, are designed for the in-situ rotation using the wobble stick inside the UHV chamber. Each separated tooth of the side gears enables the precise angular control of the central gear tooth-by-tooth. As a result, the height of the sample plate can be positioned with a travel range of $\sim 120 \mu\text{m}$ and a precision of $\sim 1.4 \mu\text{m}$. Additionally, a circular piezoelectric actuator (blue) is integrated and provides a travel range of $\sim 1.8 \mu\text{m}$ with < 1 nm precision at room temperature. Such combination of gearbox and piezoelectric actuator allows for controlling the distance between the indenter and sample continuously with sub-nanometer precision.

Fig. 3.3 shows the photographs of relaxed graphene/polyimide film with relatively low strain and one with a teepee tent-like shape (referred to as "tented" below) in high strain, applied using the gearbox-based control system. To go from the relaxed structure to the tent shape, the

central gear is rotated by one tooth of a side gear ~ 5 times. The photograph of the assembled sample holder is shown in the bottom right of Fig. 3.3.

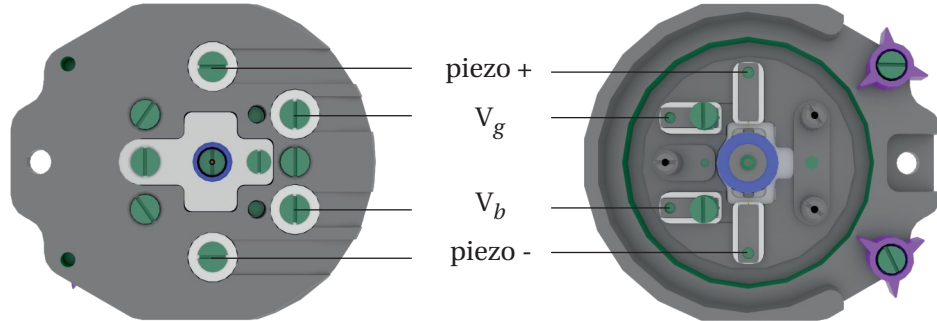


Figure 3.4: Electrical contact pins for connecting the piezoelectric actuator, V_b , and V_g .

Four electrode pins are connected to the piezoelectric actuator (plus and minus, Fig. 3.4), Pd clamp (for V_b), and the deposited Au film at the bottom of polyimide (for V_g), respectively.

3.1.2 Data Analysis

Two different methods are utilized to determine the strain experienced by 2D materials in atomically-resolved STM images: changes in lattice parameters and local curvatures.

The first approach focuses on determining the strain by examining changes in the position of local lattice points. The main task is detecting and fitting the local lattice points in the images converted by Fourier transformation. The second approach employs a pure bending approximation to model the bending strain on the 2D material induced by the local curvatures. Therefore, the calculation of local curvatures by utilizing an appropriate mathematical formulation has been developed. Further elaboration can be found in the text below.

To ensure reproducibility and reliability in data analysis, I have established a homemade code based on MATLAB. The systematic characterization of strain using two approaches can establish their cross-correlations, thereby providing a more comprehensive understanding of the strain experienced by 2D materials.

A. Lattice Parameters

To obtain the local lattice parameters, the image is first divided into smaller areas, typically with the physical size of $\sim 1 \text{ nm} \times 1 \text{ nm}$ ($\sim 30 \text{ pixel} \times 30 \text{ pixel}$). The choice of area size depends on each image's quality, which is determined by balancing the clarity of the reciprocal lattice points with the resolution of the local strain. 2D fast Fourier transformation (FFT) converts each area into reciprocal space. Before the FFT, the image is padded with zero to enlarge

the converted image size, which improves the accuracy in the following fitting step. The Hann function is used as the window for FFT to enhance frequency resolution and reduce spectral leakage. Then, a Gaussian blurring on the FFT-converted image is performed to reduce electronic noise for better detecting the lattice points. Bright spots in a smoothed image are identified as lattice points when their intensities exceed a certain threshold. A sub-image containing the bright spot is cropped and fit by a 2D Gaussian function with five fitting parameters: the amplitude and two lateral widths and positions to determine the position of lattice points with subpixel accuracy.

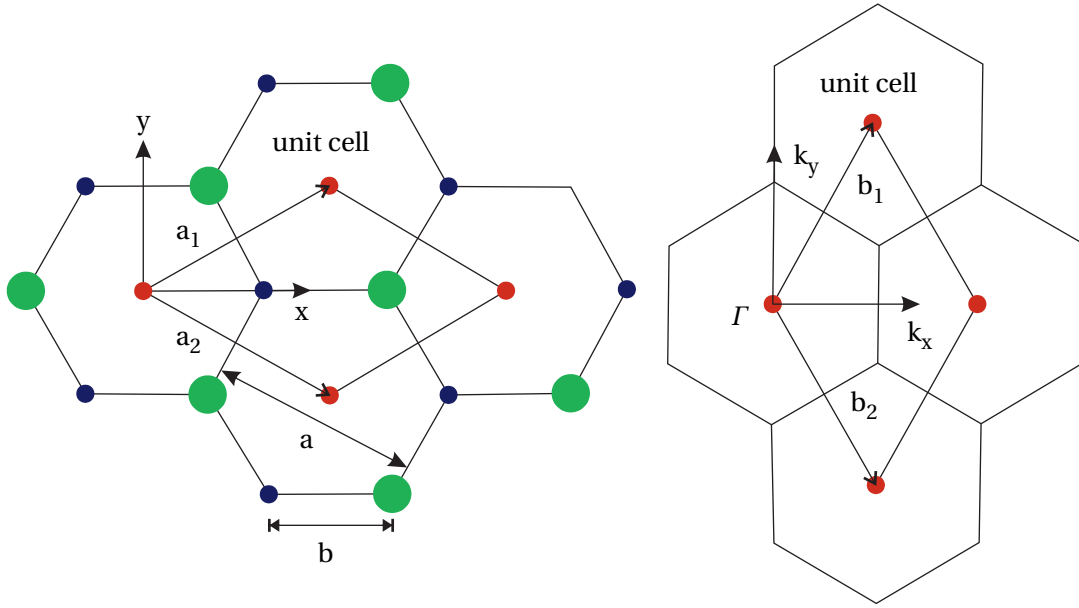


Figure 3.5: Structure of the hexagonal lattice. Bravais lattice (left) and reciprocal space (right). The green and black dots represent the Mo and S atoms, respectively.

For 2D materials with the structure of hexagonal lattice, such as graphene and monolayer MoS₂ studied in this thesis, the locations of lattice points can be used to calculate local lattice constants (a) in real space according to the equation: $b = 4\pi/(\sqrt{3}a)$, where b is the length of the reciprocal lattice vector. This equation can be understood by looking at Fig. 3.5, showing the Bravais and reciprocal lattice structure of MoS₂ as an example. The two basis lattice vectors describing the unit cell of MoS₂ Bravais lattice are:

$$a_1 = a \left(\frac{\sqrt{3}}{2}, \frac{1}{2} \right), a_2 = a \left(\frac{\sqrt{3}}{2}, -\frac{1}{2} \right). \quad (3.1)$$

Similarly, the unit cell of MoS₂ in reciprocal k -space can be described by the two basis reciprocal lattice vectors:

$$b_1 = \frac{4\pi}{\sqrt{3}a} \left(\frac{1}{2}, \frac{\sqrt{3}}{2} \right), b_2 = \frac{4\pi}{\sqrt{3}a} \left(\frac{1}{2}, -\frac{\sqrt{3}}{2} \right), \quad (3.2)$$

with the length magnitude of $4\pi/(\sqrt{3}a)$. They have the following relationship with each other:

$$a_i \cdot b_j = 2\pi\delta_{ij}, \quad (3.3)$$

which leads to the equation used to calculate lattice constants. Note that there are three lattice constants along three different directions in each local area.

After getting the lattice constants, they can be converted into the strains by referencing to the intrinsic lattice constant. The intrinsic lattice constant, a_0 , is experimentally defined as the local lattice constant at the unstrained area that has the largest magnitude of the radius of curvature. The obtained intrinsic lattice constant will be around the median value in the histogram of the lattice constant map because of the Gaussian distribution of local curvature.

Then, the strain, ϵ , for each local area is calculated by:

$$\epsilon = \frac{a - a_0}{a_0} \times 100\%, \quad (3.4)$$

which is equal to the changes in a compared to a_0 , expressed in the unit of %.

In practice, the image contains non-negligible noise that significantly decreases the visibility of atomic corrugation. Therefore, the treatment for noise reduction is required. For this purpose, two image processing methods before the analysis, including line-shift aligning and FFT filtering, are performed. The shifts in the scan lines are calculated by taking the median in each line. Then, the abrupt changes are identified in the median curve using penalized contrasts. The values in those changing points are smoothed using the moving average filter. The height offset in the misaligned scan lines is tuned according to the new median curve. Finally, a band-pass filtering is applied to the whole image for noise reduction, which keeps only the frequency components around the lattice points.

B. Principal Curvature

The maximum and minimum principal curvatures, k_{max} and k_{min} , respectively, of the image are calculated as follows:

$$\begin{aligned} k_{max} &= H + \sqrt{H^2 + K}, \\ k_{min} &= H - \sqrt{H^2 + K}, \end{aligned} \quad (3.5)$$

where $H = \frac{1}{2}\text{tr}(S(p))$ is mean curvature and $K = \det(S(p))$ is Gaussian curvature, p , and $S(p)$ is shape operator at a point, p . The local radius of curvature (R) is chosen to be $1/k_{max}$ or $1/k_{min}$, depending on the absolute magnitude in which one is smaller, which has the higher contribution to the bending effect for the 2D material.

The radius of curvatures is converted into the strains, expressed in the unit of %, by using the equation:

$$\epsilon = \frac{t/2}{R - t/2} \times 100\%, \quad (3.6)$$

where t is the thickness of the sample. In this thesis, t is chosen to be $1 \mu\text{m}$ for the polyimide film and 0.65 nm for monolayer MoS_2 and 0.345 nm for graphene, which are the interlayer distances of their bulk counterparts.

Analogous to the analysis of lattice parameters, the image processing before the curvature analysis is required, including line-shift aligning, median filtering, and low-pass Gaussian filtering. Image processing aims to reduce local surface corrugation coming from atomic protrusion, defects, or adsorbates. Briefly, line-shift aligning is first performed to make the surface smooth and continuous, similar to that done in lattice analysis. A median filtering with a proper area size is applied to every pixel in the raw image to remove locally distorted patterns such as defects and adsorbates. Each pixel value takes the median of neighboring pixels within $\sim 3 \text{ nm}$ in diameter. Therefore, the spikes and high-frequency noise are reduced, keeping only the surface morphology with low-frequency components. Finally, a low-pass Gaussian filtering with a standard deviation of $\sim 2 \text{ nm}^{-1}$ can be optionally performed to reduce the high-frequency components further.

C. Cross Correlation

To compare the similarity between images of the STM topography, the calculated local lattice parameter and curvature, the 2D cross-correlations are used based on the equation:

$$\gamma(u, v) = \frac{\sum_{x,y} [f(x, y) - \bar{f}_{u,v}] [t(x - u, y - v) - \bar{t}]}{(\sum_{x,y} [f(x, y) - \bar{f}_{u,v}]^2 \sum_{x,y} [t(x - u, y - v) - \bar{t}]^2)^{0.5}}, \quad (3.7)$$

where $\gamma(u, v)$ is the correlation matrix, f and t are the two images to be calculated, \bar{t} is the mean of t , and \bar{f} is the mean of $f(x, y)$ in the region under t . Note that the cross-correlation coefficients are normalized to -1 and 1, corresponding to the perfect negative and positive correlation, respectively.

3.2 Atomic Force Microscopy

Basics

As STM is limited to probing conductive surfaces, AFM was developed to measure non-conductive surfaces [155]. AFM shares several fundamental aspects and components with STM, such as vibrational isolation, scanning processes, and approaching mechanisms. AFM tip, which is mounted at the end of a flexible cantilever, senses the force from tip-sample interactions, resulting in a cantilever deflection and subsequently magnified through an optical lever system [156]. AFM can be operated in intermittent contact mode, i.e. tapping

mode, by using cantilevers with amplitude modulation. The tapping mode reduces the tip-sample contact duration, thus minimizing perturbations to the sample. However, the tapping mode does not entirely eliminate tip-sample force interactions. In each oscillation cycle, the tip apex remains in close proximity to and in contact with the sample surface for a brief period. Consequently, the tip undergoes attractive and repulsive forces. It has been shown that the phase shift ($\Delta\phi_0$) in the oscillation of the cantilever, caused by the tip-sample force interactions, can be expressed as [157]:

$$\Delta\phi_0 \approx \frac{Q\sigma}{k}, \quad (3.8)$$

where k is the cantilever spring constant, Q is the quality factor, and $\sigma = \sum_i \partial F_i / \partial z$ is the sum of the force derivatives for all the force F_i acting on the cantilever. A positive (negative) phase shift occurs when the overall force acting on the tip is repulsive (attractive). When the overall force derivative is predominantly influenced by surface stiffness and the tip is much harder than the sample, the magnitude of phase shift is:

$$\Delta\phi_0 \approx \epsilon \bar{a} E_s \frac{Q}{k}, \quad (3.9)$$

where E_s is sample Young's modulus, ϵ is a number between 1.9 and 2.4, and \bar{a} is the time-averaged radius of contact area. Therefore, the phase images in tapping mode AFM can be used to distinguish surface features of different stiffness.

Setup

Our AFM (Bruker, Dimension Icon, OLYMPUS tip, OMCL-AC200TS-R3) measurements were conducted in tapping mode in air at room temperature. The image analysis was done by using Gwyddion [158].

3.3 X-ray Photoelectron Spectroscopy

Basics

X-ray photoelectron spectroscopy (XPS) is a surface-sensitive analytical technique. It works by bombarding a sample with X-rays, which causes the electrons in the sample to be emitted, called photoelectrons. The kinetic energy of the photoelectron (E_{kin}) can be used to calculate the binding energy of the electrons in the sample (E_B) by: $E_B = h\nu - E_{kin} - \phi$, given the knowledge of X-ray energy ($h\nu$) and spectrometer work function (ϕ). As E_B is unique for each element in different chemical states, by measuring the kinetic energy and intensity of the photoelectrons, XPS can determine the elemental composition, chemical environment, and electronic structures. The surface sensitivity can also be controlled by adjusting the sample surface angle relative to the detector. For example, when the sample surface is perpendicular to the detection pathway, the surface sensitivity is reduced because more photoelectrons can

come from the deeper region below the surface with a minimized scattering path.

Special care must be taken to avoid surface charging, which occurs more significantly when the sample is bombarded with X-rays in a UHV environment. As the photoelectrons are emitted, they leave net positive charges on the surface. These positive charges can attract electrons from the surrounding vacuum, resulting in the reduced kinetic energy of photoelectrons, which affects the data accuracy. The magnitude of shift depends on the properties of the sample and the conditions of the measurement. For conductive samples, usually a proper ground connection is sufficient. For less conductive samples, the charging effect must be compensated using a low-energy electron flood gun that neutralizes the surface charge. Nonetheless, when analyzing XPS spectra, it is important to select an appropriate charging reference peak for energy scale correction. The peak should be from a highly abundant element in the sample and well-resolved with a high signal-to-noise ratio, such as peaks coming from the decorated Au pad on the sample surface instead of adventitious carbon coming from the surface contamination [159].

To interpret a XPS spectrum, peak deconvolution is required, which can be complex and require a good understanding of the sample configuration and technique to ensure accurate data analysis. Peak deconvolution is necessary because, in the region of interest, the XPS spectrum could have overlapping peaks from different elements present in the sample.

Here are some general steps to perform peak deconvolution:

1. Identify the origin of peaks of interest, including the elements, oxide state, and surrounding environments.
2. Fix the conditions of fitting parameters, such as the relative peak separation and intensity between spin-split peaks and the relative peak intensity between peaks from different elements using the knowledge of sample configuration.
3. Adjust the parameters of peak shapes, such as the position, width, and intensity of the peaks, until the best fit is obtained.
4. Repeat the process for each peak in the spectrum and adjust the parameters of peaks until the entire spectrum is well-fitted.
5. Once the peaks are fitted, the individual peak areas can be used to calculate the relative concentrations of the elements in the sample.

It's important to note that the peak deconvolution process is complex and can be quite time-consuming. The accuracy of results would depend on the data quality and the operator's skill. Throughout this thesis, CasaXPS software is used to perform peak deconvolution.

Setup

Our XPS (SPECS) measurements on monolayer MoS₂ were performed with a non-monochromatic Mg K α X-ray source (XR50, $h\nu=1253.64$ eV, 220W, 10 kV) and a hemispherical electrostatic analyzer (PHOIBOS 150 with MCD-9 spectrometer). The analysis chamber was maintained at base pressure $\sim 5 \times 10^{-10}$ mbar. The spectra were acquired in the sequential mode from the whole sample area. High-resolution spectra of Mo 3d/S 2s (238-224 eV), S 2p (167-159 eV), and Au 4f (92-80 eV) were recorded at a step of 0.05 eV, pass energy of 10 eV, a dwell time of 0.1 s, and total scans of 2-6k times. Iris size in the detection path was tuned according to the sample size to be 3-5 mm in diameter. Au 4f_{7/2} at 84 eV was used as our charging reference for all samples. For those samples where the substrate did not contain Au, an additional Au layer was deposited next to the MoS₂. The calibration and linearity of the binding energy scale were confirmed by fixing the positions of Au4f_{7/2} and Au4d_{5/2} peaks to 84 eV and 335.1 eV, respectively, using a Au(111) single crystal (MaTeck, Germany). FWHM of Au4f_{7/2} measured by using a pass energy of 10 eV is ~ 0.94 eV. The Pd and Au deposited polyimide films and HOPG were connected to the electrical ground by a top metal fixing plate. Before loading into the load-lock chamber, the monolayer MoS₂ without PMMA was air-exposed <30 mins when assembled on the sample holder. The load-lock chamber was then evacuated overnight to reach a pressure $\sim 3 \times 10^{-8}$ mbar before transferring the sample into the analysis chamber.

3.3.1 Compatibility with Strain- and Gate-Controllable Sample Holder

To use the strain- and gate-controllable sample holder inside the XPS system, I have modified the measurement stage with four extra electrode pins insulated from the ground, as shown in the top left of Fig. 3.6. Besides, an e-beam heating stage with the in-situ filament exchange mechanism is implemented, allowing for surface cleaning of strain- and gate-controllable sample holder and various samples, including metal crystals for XPS calibration (bottom of Fig. 3.6).

3.4 Raman Spectroscopy

Basics

Raman spectroscopy is a widely used spectroscopic technique that enables the determination of the vibrational information of materials by measuring the inelastic scattering of light [160]. Typically, a laser light is focused on the materials, which then interact with various excitations modes. The scattered light resulting from the vibrational interactions is then measured, providing valuable structural fingerprints of the materials. Nowadays, Raman spectroscopy has emerged as a fast, convenient, and nondestructive technique for characterizing the fundamental properties of 2D materials. Raman characterization covers a wide range of issues, including strain, doping concentration, temperature, layer number, defect density, crystal-

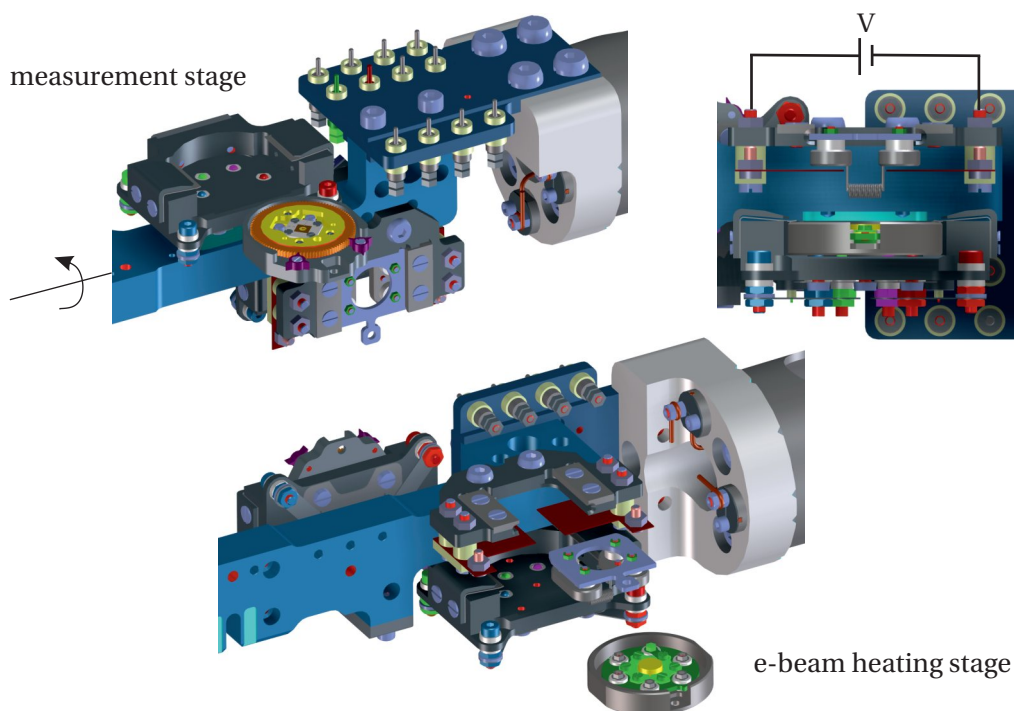


Figure 3.6: Compatibility of XPS with the strain- and gate-controllable sample holder.

lographic orientations, phase transition, and many more. Notably, Raman spectroscopy is non-destructive to the sample and does not require a complex sample preparation process as long as the laser intensity is kept below the threshold. However, two significant drawbacks of common Raman spectroscopy are the relatively weak signal response and limited spatial resolution, although advanced Raman spectroscopy techniques, such as coherent anti-Stokes spectroscopy, stimulated Raman scattering, and tip-enhanced Raman spectroscopy have been developed [161].

A more comprehensive description of the Raman spectroscopy for the 2D materials can be found in [36, 161, 162].

Setup

Our Raman spectroscopy (S&I GmbH) was operated in air at room temperature. For the suspended MoS_2 /polyimide sample, a 488 nm laser focused by 10 \times objectives with a spot size of ~ 10 μm was used. For supported MoS_2 /metal samples, a 512 nm laser focused by 100 \times objectives with a spot size of ~ 1 μm was used. The incident laser intensity was kept < 0.12 $\text{mW}/\mu\text{m}^2$ to prevent thermal-induced artifacts [163]. 1800 lines mm^{-1} grating was used. The typical acquisition time was ~ 5 mins.

4 Materials and Sample Preparation

In this chapter, I will cover the different protocols that I employed for sample preparation. This includes the procedures for transferring polyimide film, ensuring its compatibility with UHV conditions, transferring 2D materials, depositing metal, and assembling and utilizing the strain- and gate-controllable sample holder.

4.1 Polyimide Film

The polyimide film is synthesized from 3,3',4,4'-biphenyltetracarboxylic dianhydride (BPDA) with p-phenylene diamine (PDA), serving as a flexible substrate for carrying 2D materials in the strain- and gate-controllable sample holder. The fabrication of the polyimide film was carried out by spin-coating a Dupont PI2610 solution at 6000 rpm onto a glass substrate with dimensions of $\sim 5 \times 5 \text{ cm}^2$. This process was carried out by experts from the Natural and Medical Sciences Institute at the University of Tübingen. The thickness of BPDA-PDA polyimide film is measured to be $\sim 1 \mu\text{m}$ using a stylus profilometer (Veeco Dektak-8).

4.1.1 Transfer

The polyimide film can be separated from the glass by adding water to its edges, as shown in Fig. 4.1. Before separation, the polyimide film is cut into a smaller domain with a size of $\sim 3 \times 3 \text{ mm}^2$. The detached polyimide film, which suspends on the water surface, is picked up by using a blunt blade to prevent causing damage, which is critical for gate performance. Then, the polyimide film carried on top of the blade can be landed on other substrates, for example, silicon or ceramic plate with a hole at the center.

In order to incorporate a metal coating onto the polyimide bottom for the gate structure (as depicted in Fig. 3.2), a layer of $\sim 20 \text{ nm}$ of gold is initially deposited onto the polyimide film. Following this, the polyimide film is detached from the glass substrate and flipped over during the transfer process.

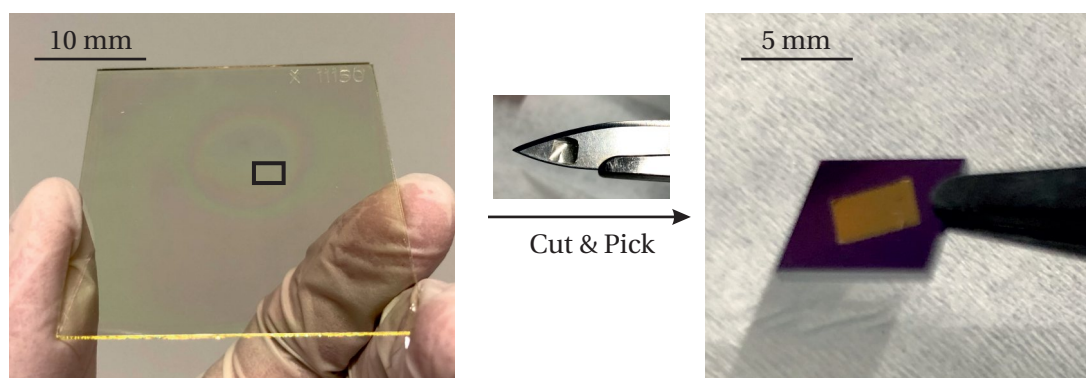


Figure 4.1: Transfer of the polyimide film. The polyimide film is first coated on glass and then transferred onto the silicon substrate by using a blunt blade with water intercalation.

4.1.2 UHV Compatibility of Polyimide Film

In order to acquire atomic-resolution STM images, it is necessary to subject the sample to an outgassing process within a UHV environment. This is done to eliminate any surface adsorption that may have accumulated when the sample was transferred and assembled in the air. To prevent any additional carbohydrates from evaporating from the heated polyimide film and contaminating the sample surface or the chamber, the mass spectrum of the polyimide film was measured at various temperatures (Fig. 4.2). The polyimide film, which has a thickness of $\sim 1 \mu\text{m}$ and size of $\sim 5 \times 5 \text{ cm}^2$, was heated using a UHV evaporator located within a chamber equipped with a mass spectrometer. The base pressure within the chamber was $\sim 6 \times 10^{-9}$ mbar. Prior to the introduction of the polyimide film, the evaporator was outgassed up to 600°C for cleaning purposes. In Fig. 4.2, the mass spectrum of the polyimide film is displayed. The temperature is increased from room temperature to 96°C , 142°C , and 176°C . Prior to each increase in temperature, the sample was cooled back down to room temperature to assess the stability of the polyimide film and the reproducibility of its spectrum. The mass spectrum exhibited only minor changes as the temperature increased to 96°C . However, at 142°C , the peak at m/z of approximately 72 and 91 slightly increased. As the temperature increased further to 176°C , the peak at m/z of approximately 44, 56, 84, and 98 significantly increased, with an interval of 14 (CH_2) between the values, indicating that these peaks may originate from hydrocarbon components. Therefore, during the outgassing process, the temperature is maintained below 100°C .

4.2 Transfer of Graphene and Monolayer MoS_2

The CVD-grown graphene on Cu and MoS_2 monolayer on SiO_2/Si were purchased from 2D Semiconductors (CVD-Graphene-Cu and CVD-MoS2-ML-S) and were transferred to other target substrates, such as polyimide film, silicon, metal surfaces, and HOPG, using the wet etching method, as adapted from [154]. To transfer, polymethyl methacrylate (PMMA, 950k, 2.5% in Chlorobenzene) was spun onto the 2D material with four edges taped (Scotch tapes)

4.2 Transfer of Graphene and Monolayer MoS₂

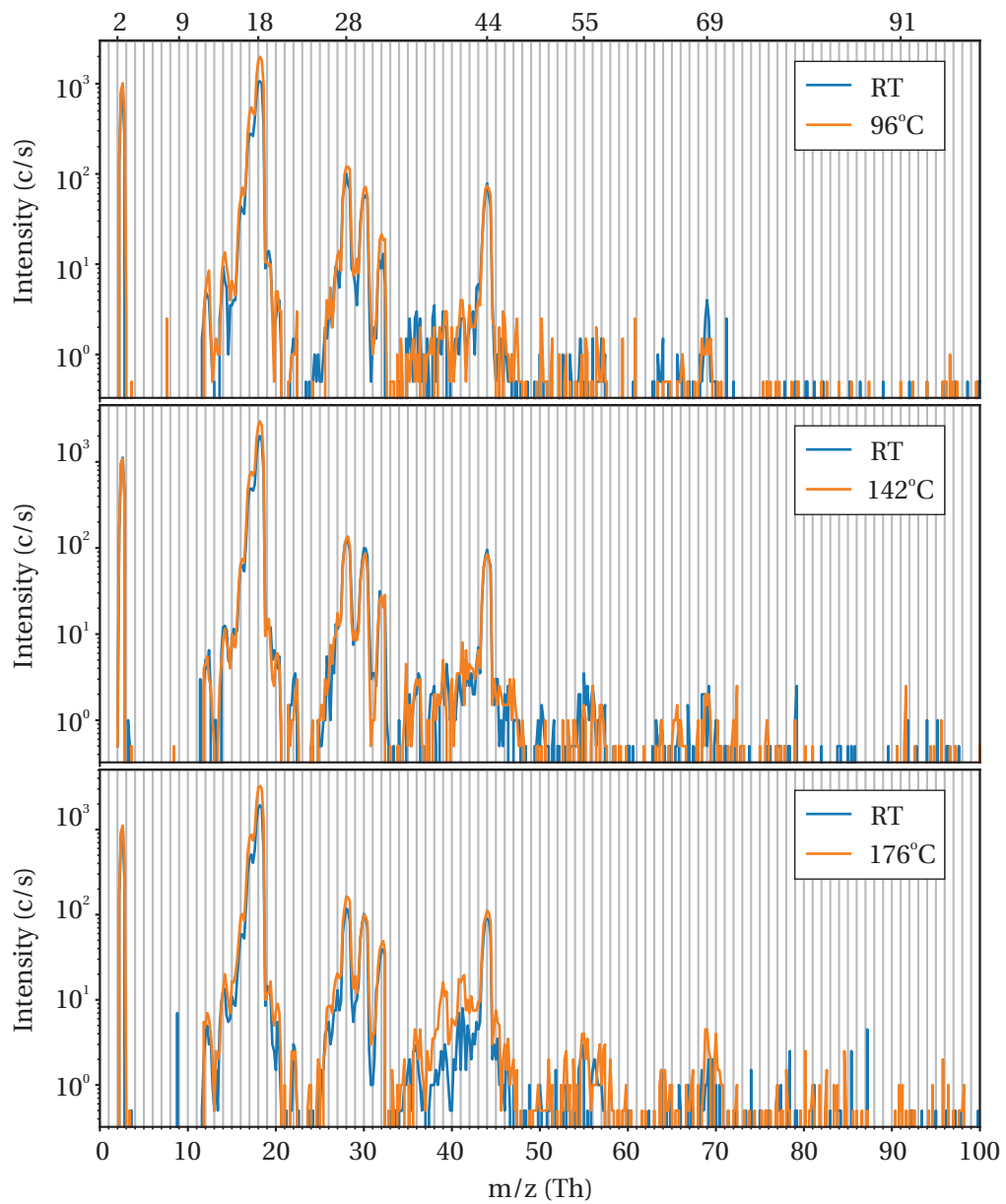


Figure 4.2: Mass spectrum on polyimide film were obtained at 96°C, 142°C, and 176°C, respectively. The temperature was increased from room temperature (RT) to the aforementioned temperatures to obtain the mass spectrum.

at 3,000 rpm for 60 s and then cured at 80 °C for 3 mins. The 2D material coated with PMMA film was then cut into domains of $\sim 2 \times 2 \text{ mm}^2$ before Cu or SiO_2 was removed by using $\sim 1 \text{ M}$ ammonium persulfate (Sigma-Aldrich) and $\sim 2 \text{ M}$ KOH (Merck, SKU 1.05029), respectively. Detached films suspended on the etchant were transferred to DI water more than 3 times to remove etchant residues on the bottom. Finally, a tweezer was used to catch the suspended film with the target substrate and slowly lift them from the water below. Freshly transferred samples were heated and blown to remove the water trapped at the interfaces. Before measurement, the sample was dipped into acetone for over 30 mins to remove PMMA and subsequently cleaned with isopropynol.

4.3 Deposition of Metal Contacts

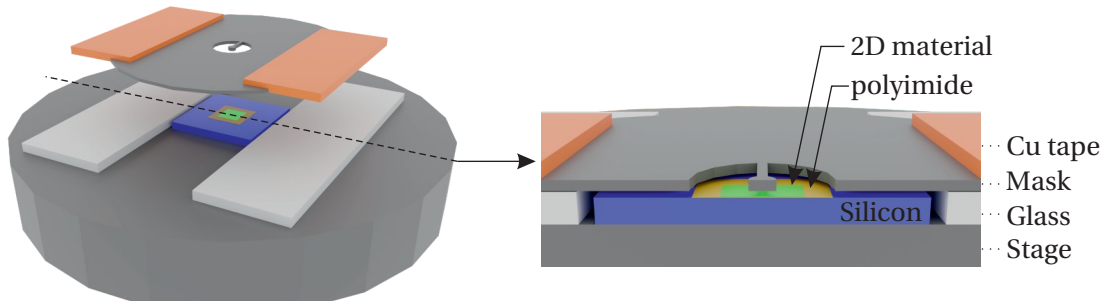


Figure 4.3: Schematic of deposition of metal contacts using a shadow mask.

Once the 2D material had been successfully transferred onto the polyimide film, a keyhole-shaped clamp of $\sim 30 \text{ nm}$ thickness composed of Pd was deposited onto the edge of the 2D material to enhance strain transfer. A schematic of the home-built deposition stage is presented in Fig. 4.3. The metal mask used in the process has a thickness of 0.2 mm . The location of the mask can be adjusted by hand on two glass slides affixed to the deposition stage. Once the mask is situated in the desired location, it is secured in place on the glass using Cu tape on two sides. The narrow gap between the mask and the sample surface, approximately 0.1 mm , enables the deposition of metal contact with sharp edges.

Fig. 4.4 shows the before and after images of a keyhole-shaped Pd clamp deposition on the monolayer MoS_2 /polyimide. The metal deposition was carried out using a metal depositor (Leybold, Univex 450) in a cleanroom with a flux of 1 \AA s^{-1} and a base pressure of less than $1 \times 10^{-6} \text{ mbar}$. The edge of the monolayer MoS_2 is depicted as a dashed line. The area inside the keyhole-shaped clamp is designated for indentation application, while the area outside serves as a reference area where the sample is flat and supported on the ceramic plate. A zoom-in image of the clamp's interior is presented in Fig. 4.4, where the monolayer MoS_2 /polyimide is smooth and free of visible cracks, wrinkles or bubbles. This ensures effective strain transfer from the polyimide film to the monolayer MoS_2 .

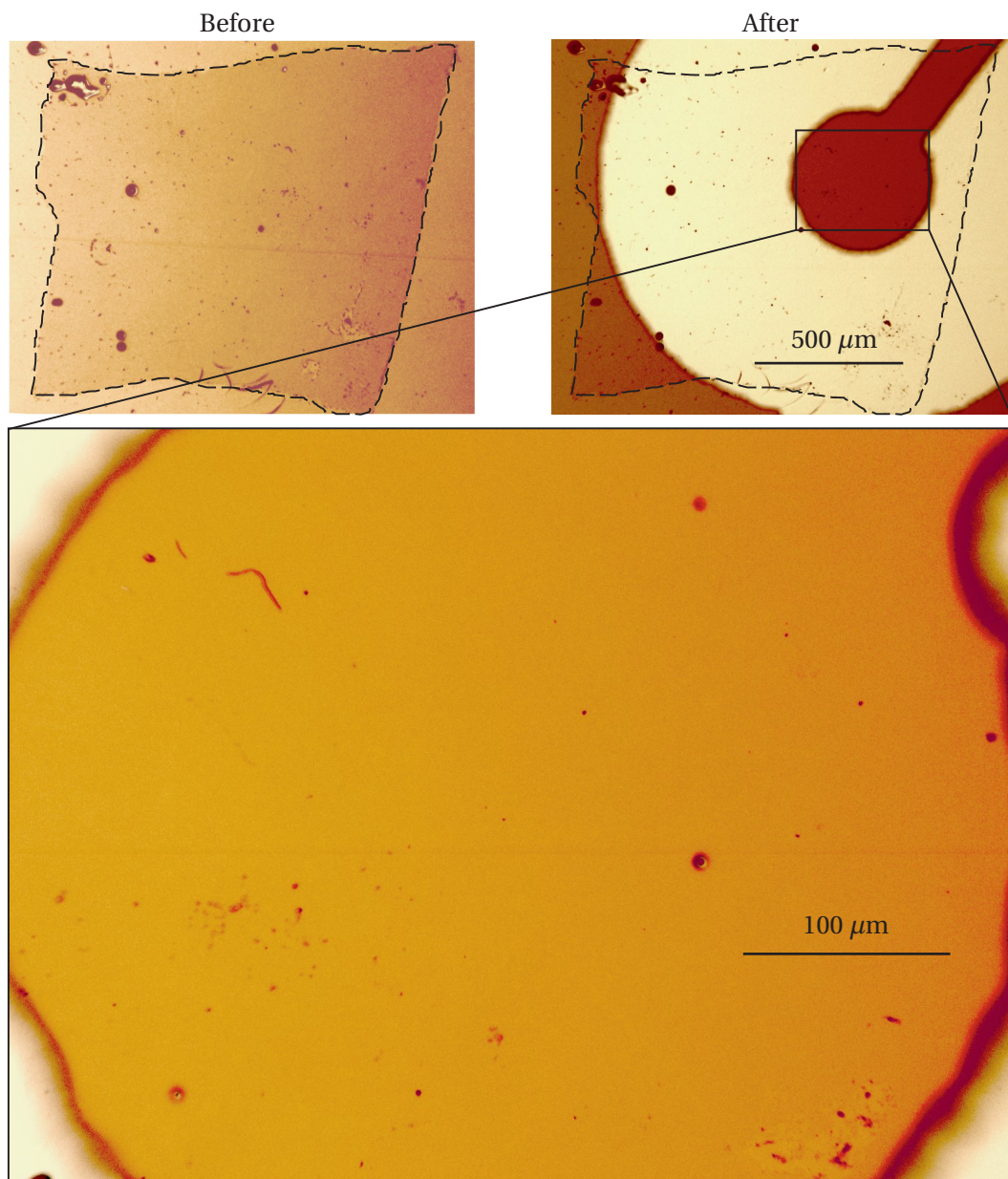


Figure 4.4: Before and after deposition of Pd clamp on monolayer MoS₂/polyimide. The edge of monolayer MoS₂ is marked as a dashed line. Inside the clamp, the monolayer MoS₂ has no visible cracks, and the polyimide surface is smooth without visible wrinkles or bubbles.

4.4 Strain- and Gate-Controllable Sample Holder

In this section, a comprehensive account of the strain- and gate-controllable sample holder is presented, covering its assembly, the procedure for indenter approaching, and loading it into the UHV chamber.

4.4.1 Assembly

Detailed installation instructions for the strain and gate-controllable sample holder are presented in Fig. 4.5. The installation process can be divided into six primary steps. Before assembly, all components were sonicated in acetone and isopropanol for 30 minutes to remove any surface contamination.

Step 1 – Metal cylinders & Side gears

The first step involves fixing the three metal cylinders (plate fixers) that prevent the sample plate from rotating. These fixers should be installed first because they require a stronger force to tighten the screws. After the side gears are installed, it's essential to test whether they can be smoothly rotated using a tweezer, as they'll later need to be turned by a wobble stick in the vacuum chamber.

Step 2 – Piezo & Pins

The piezoelectric actuator (PD050.3x, PI GmbH) is glued onto a ceramic support using epoxy glue (EPO-TEK, E4110). Its travel range is $\sim 1.8 \mu\text{m}$ at room temperature. The plus and minus sides of the piezoelectric actuator coatings are connected to two electrode pins by Au wires with a diameter of $\sim 50 \mu\text{m}$. Before its deployment in UHV chamber, the piezoelectric movement can be evaluated by placing the actuator on a motorized stage and focusing a laser spot onto its surface with a 100x objective lens. Upon applying voltage to the actuator, the observed divergence in the laser spot serves as an indicator of the actuator's movement. The piezoelectric movement can subsequently be measured and compensated for by adjusting the motorized stage accordingly.

Step 3 – Indenter

The indenter is fabricated by electrochemical etching of a straight W wire with a diameter of $\sim 0.25 \text{ mm}$. Then, the W tip is ground to have an apex radius of a few μm . The indenter is then glued into the hole of the indenter screw at the center, and the screw is rotated into the center of a hat-shaped metal, which is glued at the center of the piezoelectric actuator.

Step 4 – Gearbox

To ensure low-friction rotation, the sample holder body and sample plate are made of Ti grade 2 (pure Ti), while the central gear is made of a W-Cu alloy (80/20). W-Cu alloy (80/20) has a thermal expansion coefficient close to that of Ti grade 2, ensuring that the gearbox can work at low temperature ($\sim 4.8 \text{ K}$) and room temperature. The ceramic plate is first mounted on the sample plate to prevent hitting the indenter when tightening the screws. After the central gear,

sample plate, and ceramic plate are assembled, the central gear is rotated carefully into the thread of the sample holder body. It is essential to ensure a smooth and parallel movement of the components to prevent damage to their threads. In the event that they do not rotate smoothly and become stuck, any small particles that may have accumulated inside the threads can be removed using methods such as sonication, air-blowing, or tweezers.

Step 5 – Sample

After the gearbox is installed, the indenter position is tuned to be slightly below the ceramic plate, which will minimize the travel distance of the indenter. The position of the indenter apex is marked for aligning the sample with the indenter. The 2D material/polyimide film is transferred to the ceramic plate using a blunt blade. At this moment, the water layer is intercalated between 2D material/polyimide and ceramic plate. Shortly before the water between the 2D materials/polyimide and the ceramic plate is completely dried out, the conductive epoxy (EPO-TEK, E4110) is dropped at the four edges of the polyimide film. Epoxy would then flow into the gap between the polyimide film and the ceramic plate. For solidification, the epoxy is heated up to $\sim 80^{\circ}\text{C}$ for ~ 30 mins.

Step 6 – Wires

Finally, two Au wires with a diameter of $\sim 17\ \mu\text{m}$ are used to establish electrical connections of the Pd and Au contacts to electrode pins for applying V_b and V_g . The joints are made of conductive epoxy, which solidifies later. This size of Au wire is flexible enough to be bent and used to connect Pd and Au contacts between two electrodes at specific locations. However, it is important to be aware that exposure of the sample to temperature changes between 100°C (during outgassing) and $4.8\ \text{K}$ (during measurement) could cause the joints to disconnect due to the different thermal expansion. If this happens, it could cause the STM tip to fail to approach properly and result in a bent tip. To avoid this, it is crucial to apply the right amount of epoxy to the joints, not too little or too much.

4.4.2 Indentor Approaching

Once the 2D material/polyimide is firmly affixed, the central gear should be turned counter-clockwise by two full rotations, equivalent to $\sim 100\ \mu\text{m}$, to increase the separation between the sample and the indenter. The indenter's position should then be raised by turning the indenter screw around $1/4$ rotations, equivalent to $\sim 60\ \mu\text{m}$, to approach the sample. The sample can be gradually moved towards the indenter using the side gears. These steps should be repeated until the sample and indenter are in contact, which can be observed under a microscope as depicted in Fig. 4.6. It is important to note that the indenter's position may shift slightly during the rotation of the indenter screw, as the indenter may not be perfectly perpendicular to the sample.

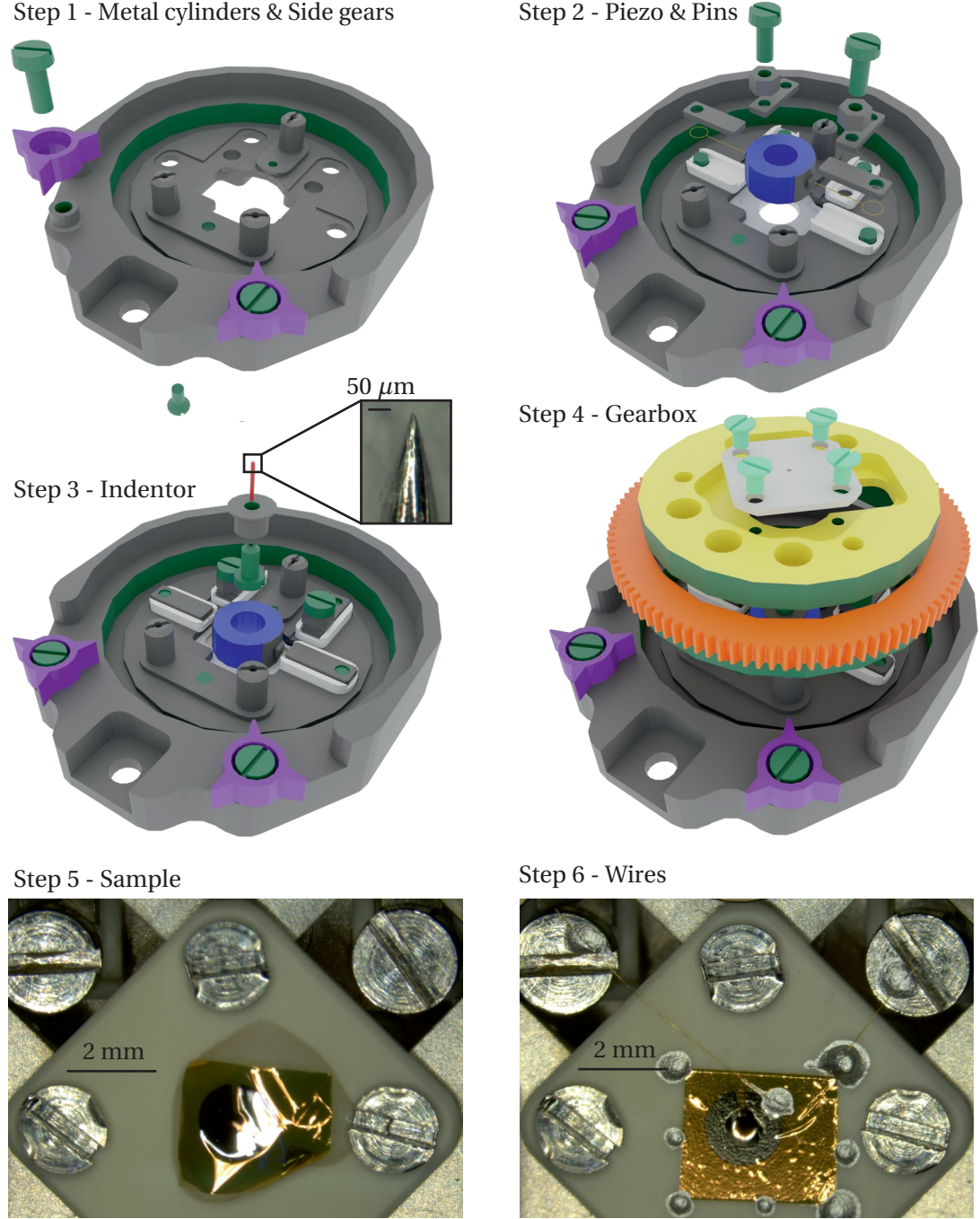


Figure 4.5: Exploded view of step-by-step installation instructions of the strain and gate-controllable sample holder. The green-colored surfaces in Step 1-4 are threaded parts.

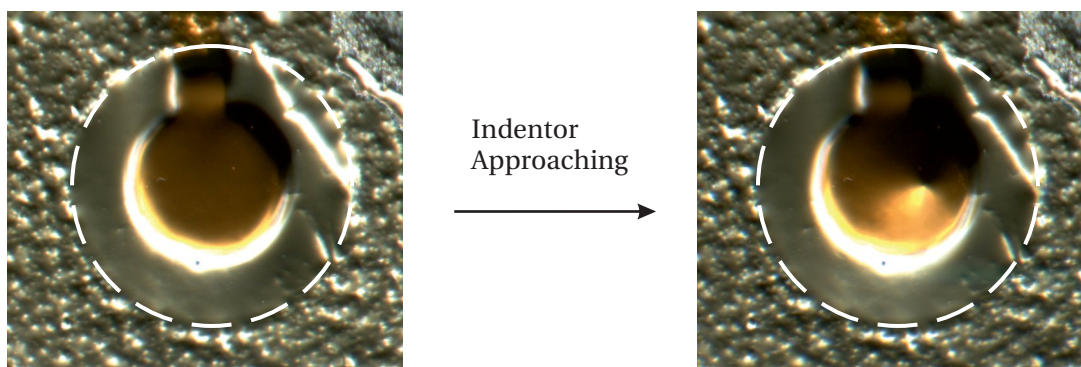


Figure 4.6: Photograph of the sample surface before and after indenter approaching. The dashed circle is the suspended area with a ~ 1 mm diameter. After indenter approaching, a tent shape is visible inside of Pd clamp.

4.4.3 Loading to STM

After approaching the indenter, the sample holder is transferred to the UHV chamber equipped with a heating stage for outgassing. The outgassing process requires careful consideration due to the temperature limitation of the piezoelectric actuator (150 °C) and the outgassing of polyimide (100 °C). The 2D material is heated up to around 100 °C for 1-2 days to ensure thorough cleaning. Following outgassing, the sample holder is inserted into the STM for measurement. During the cooling process in the STM cryostat, the indenter position may shift due to the different thermal expansion coefficients of the various constituent materials of the sample holder. To avoid any potential damage caused by the high friction between the gear teeth at low temperatures, the gear rotation is controlled on the sample stage outside the cryostat at room temperature.

5 In-situ Atomic Level Observation of the Strain Response of Graphene Lattice

This chapter demonstrates the performance of the strain- and gate-controllable STM sample by characterizing (1) the polyimide film deformation at the macroscopic scale using AFM, (2) the strain transferred on monolayer MoS₂ using Raman spectroscopy, and (3) the strain response of graphene lattice at the atomic scale using STM.

5.1 Macroscopic Scale Insight

AFM measurements are conducted to characterize the height controllability of the sample plate and indenter using the gearbox and the piezoelectric actuator, respectively. Fig. 5.1(a-b) shows how the polyimide film, before transferring the 2D material, is deformed by moving the sample plate down using the gearbox. Due to the limited lateral range of the AFM (max~40×40 μm²), the entire deformed polyimide film inside the circularly clamped area (~1 mm in diameter) cannot be imaged in a single AFM image. Therefore, the relative height change (Δh), the difference between the highest and lowest points in the image, is used to compare the shape of deformed surfaces with a range of sample and indenter heights. The change in Δh is monitored while the sample plate is moved downwards step-by-step using the gearbox-based control system. With increasing gear steps from +0 (after contact) to +4, Δh increases from 0.77 to 0.93, 1.06, 1.19, and 1.40 μm. An increasing tent-like deformation can be seen in the topographies and line profiles [164]. When the applied strain is increased further by increasing the number of gear steps to +8, the relative change in Δh increases dramatically, indicating that the deformation of polyimide film is more sensitive to the sample plate height under conditions of a higher strain. Moreover, the topography changes from a tent-like structure to a bubble-like structure at an applied strain equivalent to +8 gear steps [164]. Fig. 5.1(c) shows the dependence of Δh on the position of the indenter under the control of the piezoelectric actuator. The indenter height can be controlled with nanometer precision via the applied

¹This chapter is based on publication #8 from the publication list.

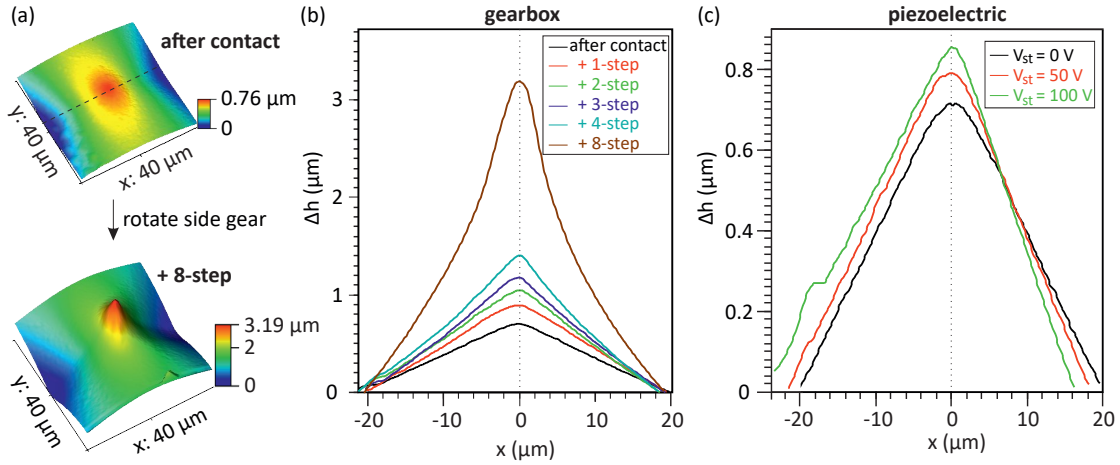


Figure 5.1: Height controllability of the sample plate and the indenter using gearbox and piezoelectric actuator. (a) AFM topography images of polyimide surfaces taken before and after moving the polyimide film down by 8-steps using the gearbox. A step is defined as the height change when one tooth of a side gear is moved. (b) Height changes by gearbox control. Line profiles are taken from the center of the deformed area, shown as the black dotted line in (a). Δh is the height difference between the highest and lowest points in the image. The position with the maximum height is defined as the center point ($x=0$). (c) Height changes by piezoelectric control. The maximum travel range of the piezoelectric actuator is $\sim 1.8 \mu\text{m}$ under an applied voltage (V_{st}) of 100 V at room temperature.

voltage to the actuator (V_{st}). As the maximum travel range of the piezoelectric actuator ($\sim 1.8 \mu\text{m}$) is larger than the gearbox precision ($\sim 1.4 \mu\text{m}$), the indenter-sample distance can be tuned continuously over a range of $\sim 120 \mu\text{m}$ while maintaining nanometer precision.

To verify how much strain can be applied and its distribution in the indentation process, the curvature-induced strain distribution on the bare polyimide film before transferring the 2D material (i.e. Fig. 5.1) is analyzed, as shown in Fig. 5.2(a). As the number of gear steps increases, the maximum strain gradually increases from 1.1% (after-contact) to 9.9% (+ 8-step), and the strained area becomes broader. Indentation-induced deformation is localized and heterogeneous. The region on top of the indenter is under tensile stress and is surrounded by the area under compressive stress. The curvature-induced strain approaches zero with increasing distance from the contact region.

It is reported that the maximum strain (ϵ_{max}) that can be applied on 2D materials through the supported polymer substrate is only 0.6-3.2%. Beyond this critical strain, 2D layers begin to slip and decouple from the substrate [37, 38, 75–81]. Therefore, to verify how much strain can be transferred from the polyimide film to the 2D material in our indentation system, Raman spectroscopy measurements were conducted. To identify the peak shifts due to strain, monolayer MoS₂ is used as the test 2D material here due to its stronger optical contrast and Raman signals than, for example, graphene on the polyimide film. As the sample surface is not flat in the process of indentation, a 10 \times objective is used, which has a longer depth of

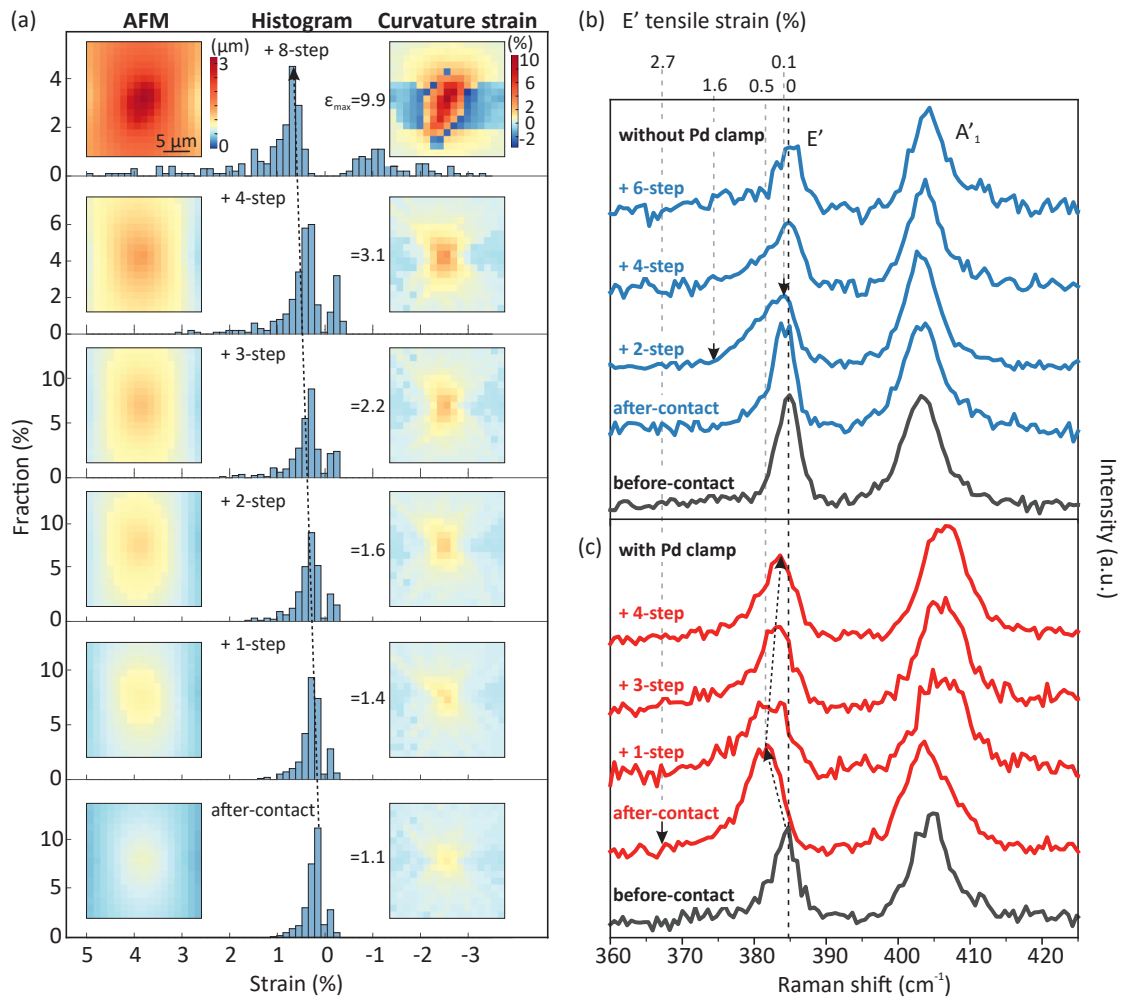


Figure 5.2: Characterization of strain distribution. (a) Calculation of the curvature-induced strain distribution based on the AFM topography images measured on the polyimide film before transferring the 2D material that were shown in Fig. 5.1. (b-c) Raman spectra taken at the indented center of monolayer MoS_2 transferred on polyimide film with increasing the number of gear steps. (b) is with and (c) is without a Pd clamp.

focus, to focus a 488 nm laser beam on the indented center with a $1/e^2$ spot size of $\sim 10 \mu\text{m}$ to maximize the Raman signals.

Fig. 5.2(b) shows the Raman spectra of monolayer MoS_2 /polyimide film. Before engaging the indenter, the monolayer MoS_2 shows the E' mode peak located at 384.8 cm^{-1} and the A' mode peak located at 403.2 cm^{-1} . Since the peak position of the E' mode is more sensitive to the strain applied through bending ($5.2 \text{ cm}^{-1}/\%$) than the A' mode ($1.7 \text{ cm}^{-1}/\%$) [69], the shift of the E' mode is used to characterize the curvature-induced strain (ϵ) transferred from the polyimide film to monolayer MoS_2 and compared with the indentation depth.

Taking the peak position before contact as our zero-strain reference, the E' peak shows a redshift of $\sim 0.6 \text{ cm}^{-1}$ when the gearbox is rotated + 2-step, which corresponds to $\epsilon \sim 0.1\%$. It is worth noting that the E' has an asymmetric distribution with the tail of the peak extending to $\sim 375 \text{ cm}^{-1}$, and its asymmetry increases with increasing gear steps. However, as the observed asymmetry of the E' peak can be induced together by the non-uniform strain distribution and the splitting of peaks [37], it is challenging to define the maximum strain from the peak fitting or its tail position. When the gearbox is rotated ≥ 4 steps, the E' peak returns toward the reference position, indicating the strain relaxation possibly due to the formation of wrinkles or cracks [165].

To enhance the strain transfer, the monolayer MoS_2 is clamped onto the polyimide film by evaporating the Pd layer on the edge of monolayer MoS_2 through a circular-shaped shadow mask [78]. Fig. 5.2(c) shows the Raman spectra of monolayer MoS_2 with an additional circular Pd clamp deposited on top. By the additional clamping, the E' peak in the after-contact case shows a larger redshift of $\sim 3 \text{ cm}^{-1}$, corresponding to $\epsilon \sim 0.5\%$, and the peak tail extends further to $\sim 368 \text{ cm}^{-1}$, which confirms that the Pd clamp enables more efficient strain transfer from polyimide film to monolayer MoS_2 . The shift of the E' peak position back to the reference position with increasing gear steps is again noted, showing a similar behavior of gradual relaxation.

In short summary, as the indentation depth increases, the curvature-induced strain increases inhomogeneously, observed in both the AFM and Raman results. The addition of a Pd top clamp can enhance strain transfer.

5.2 Atomic Scale Characterization

Our STM working at $\sim 4.8 \text{ K}$ is used to characterize the indentation response of the graphene at the atomic scale. Although the indentation depth can be controlled with nanometer precision, the induced deformation can not directly translate into the applied strain on 2D materials during STM measurement. Fig. 5.3(a-b) shows the schematics of graphene transferred onto polyimide film under relaxed and strained conditions during STM measurements. After contact and before gearbox rotation, i.e., in the relaxed case, the strain is localized on top of the indenter, and the remaining area of the film lies below the aperture (Fig. 3.3 and 5.3(a)).

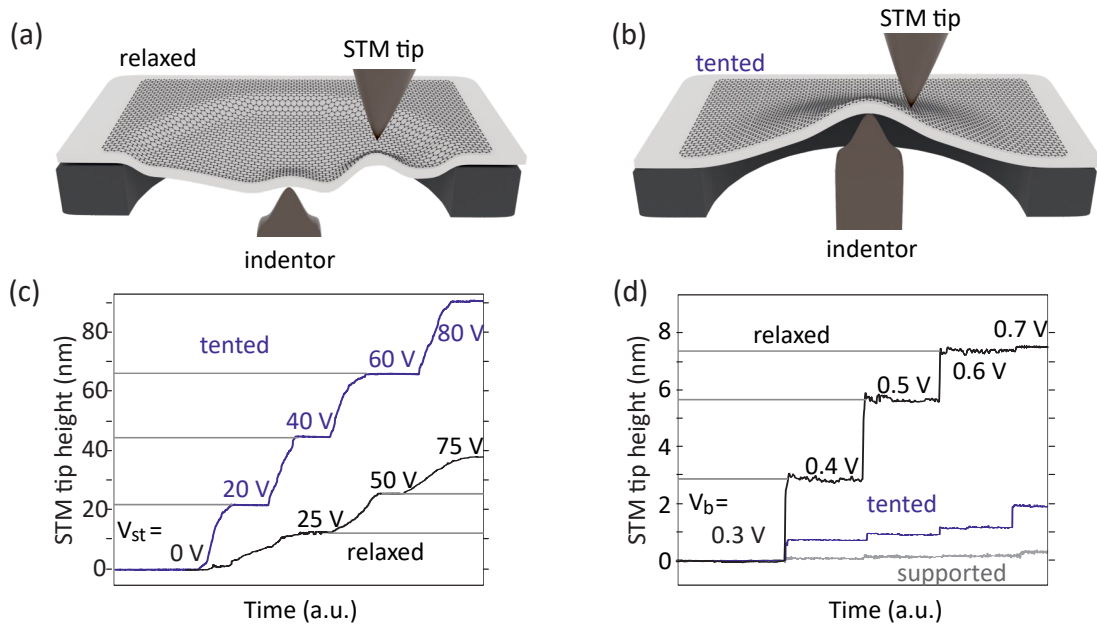


Figure 5.3: STM measurement on the graphene transferred on polyimide film. (a) Strain-free (relaxed) condition and (b) tented distortion induced by strain applied using the gearbox-based control system. The sample height dependence on the piezoelectric actuator voltage (V_{st}) and the sample bias voltage (V_b) are shown in (c) and (d), respectively.

In the high-strain case, after the gearbox rotation, the indenter exerts a force on the whole polyimide film, and a tent-like structure is formed (Fig. 3.3 and 5.3(b)). At such high strain, the film is tightened and becomes more sensitive to the indenter height.

The deformation of the 2D material depending on V_{st} is characterized by measuring the z movement of the STM tip in the constant current mode. When the indenter pushes up the graphene/polyimide film, the STM tip retracts accordingly to maintain the current constant, as shown in Fig. 5.3(c). For the relaxed condition, the STM-tip retracts (37 nm) when V_{st} increases from 0 V to 75 V. However, in the tented case, a larger V_{st} -dependent sample height change (85 nm) is observed when V_{st} increases from 0 V to 80 V. The sample height change dependence on V_{st} can be controlled reversibly (Fig. 5.4). The absence of hysteresis in the height change suggests that the polyimide film is still flexible even at ~ 4.8 K, and the slippage between indenter and polyimide film is negligible.

On the other hand, the relaxed graphene/polyimide film is easily affected by external stimuli in comparison with the tented case. Fig. 5.3(d) shows the change in STM-tip height with increasing V_b from 0.3 V to 0.7 V. The recorded heights are 0.2, 1.8, and 7.3 nm for the relaxed, tented, and supported cases. In comparison with the supported area where the STM-tip height is determined solely by the electrostatic force, a more considerable STM-tip height change in the suspended area is induced by the additional height change of the graphene/polyimide film pulled up by the STM-tip (via the van der Waals forces) [166]. A much more significant

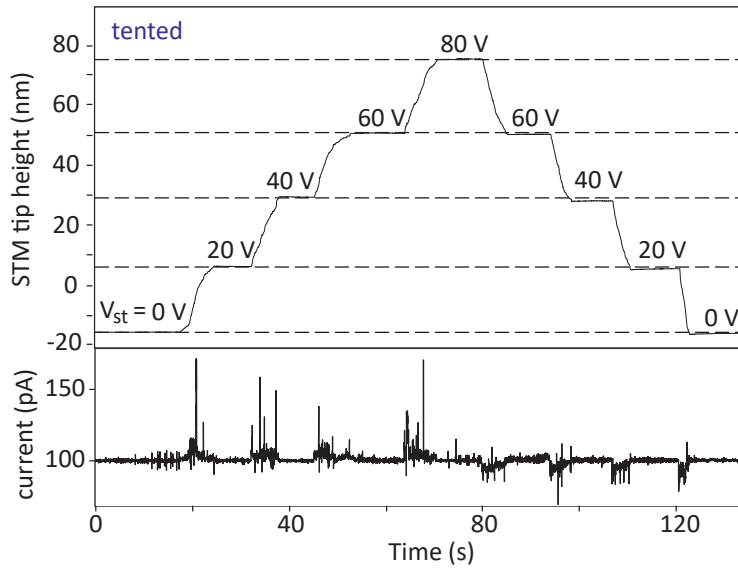
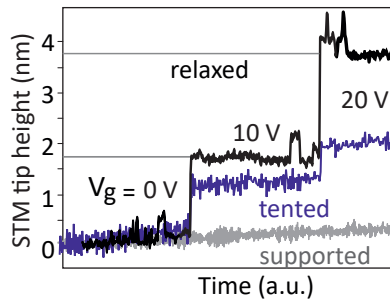


Figure 5.4: Reversible graphene/polyimide height changes by increasing the voltage applied to the piezoelectric actuator carrying the indenter (V_{st}) in the tented condition. STM in a constant current mode (0.5 V, 100 pA).

Figure 5.5: Characterization of gate-controllability. STM-tip height feedbacks how the sample height is changed by increasing gate voltage (V_g).



height change is observed in the relaxed case since the polyimide film has a lower tension, as shown in Fig. 5.3(a-b).

The gate controllability is confirmed by measuring the dependence of the STM tip height on gate voltage (V_g). As V_g increases from 0 V to 20 V, the STM-tip retracts in a constant current mode indicating that charge has accumulated on the graphene surface (Fig. 5.5), reflecting successful gating. Similar to the V_b -dependent tip height, a large height change is observed in the relaxed case, indicating the polyimide film with less tension.

The change of surface morphology and its dependence on indenter height (V_{st}) also shows a similar behavior (Fig. 5.6). In the tented case, the obvious change in the surface morphology is observed by increasing V_{st} . In contrast, in the relaxed case, the surface morphology is barely changed, and only a rigid shift of feature is observed with increasing V_{st} . Additionally, the height difference between the maximum and minimum in the tented case is 1.3-1.9 nm, which is lower than that of 2.8-3.4 nm in the relaxed case. It indicates that the tented polyimide film

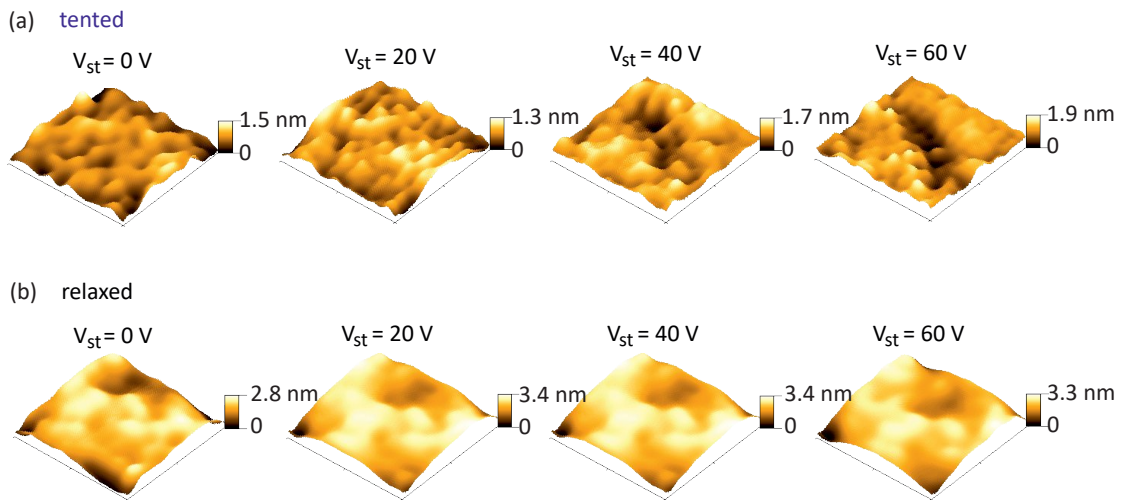


Figure 5.6: STM topography images with increasing indenter height (V_{st}). (a) tented and (b) relaxed cases. The size of the images is $15 \times 15 \text{ nm}^2$.

is more stretched and consequently flattened.

The sample holder is stable enough for the topography measurement at the atomic level, which enables us to analyze the distribution of lattice parameters for calculating the strain. Fig. 5.7(a) shows the atomic resolution STM image of the graphene/polyimide film in the relaxed case. The fast-Fourier transformation (FFT) converted image is shown in Fig. 5.7(b). The lattice points in three directions can be clearly seen. The map of local lattice constants (a_0) averaged over three directions is shown in Fig. 5.7(c). The center and width obtained by Gaussian-fitting the histogram of the lattice map are 2.27 \AA and 0.11 \AA , suggesting a range of strain of $\pm 4.8\%$ on graphene. The local curvature of substrate surface roughness has been reported to induce such fluctuation of a_0 by bending strain [1]. To verify this, the local curvature over the same small domains is calculated and its map is plotted in Fig. 5.7(d). The calculated curvature map captures the feature of hill and valley of the surface morphology measured in Fig. 5.7(a). Similarly, by calculating the cross-correlation coefficients, it is found that the maps of local a_0 and curvature are highly positively correlated, indicated by a maximum value located at the center of Fig. 5.7(e).

It is important to emphasize that the observed lattice changes, which depend on the strain, are in a range of $0.01\text{-}0.1 \text{ \AA}$. This is at the very limit of what the STM is capable of resolving. Furthermore, due to the influence of the substrate, the initial lattice spacing displays a rather broad distribution, exceeding 0.11 \AA . To analyze the dependence of lattice on V_{st} correctly, we have collected a substantial amount of data and represented it using a boxplot. The boxplot serves as a resourceful tool, adept at revealing shifts in central values as well as the spread of numerical datasets by showcasing the data quartiles. Fig. 5.8 offers an illustration of how a boxplot is presented, which consolidates a data set into five values: the minimum point, the first quartile (25%), the median, the third quartile (75%), and the maximum point. It is

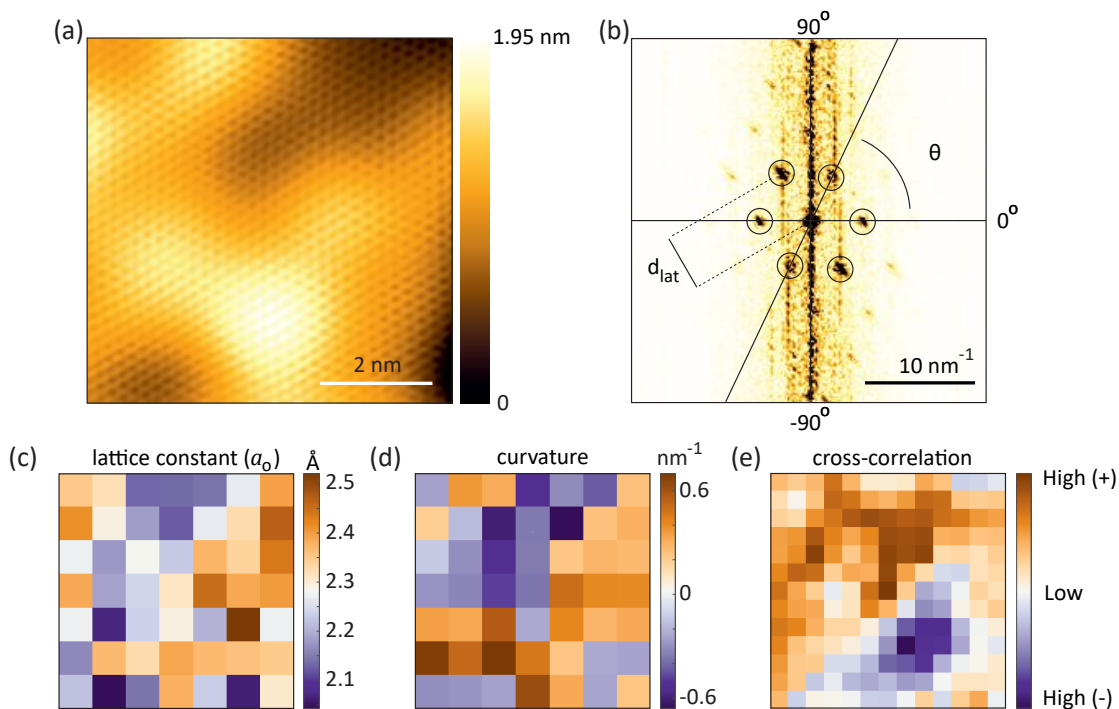


Figure 5.7: (a) Atomic-resolution image of graphene in the relaxed case and (b) its fast-Fourier transformation converted image with six clear lattice points. (c-e) The map of the local average graphene lattice constant (a_0) and local curvature calculated from (a) and their cross-correlation.

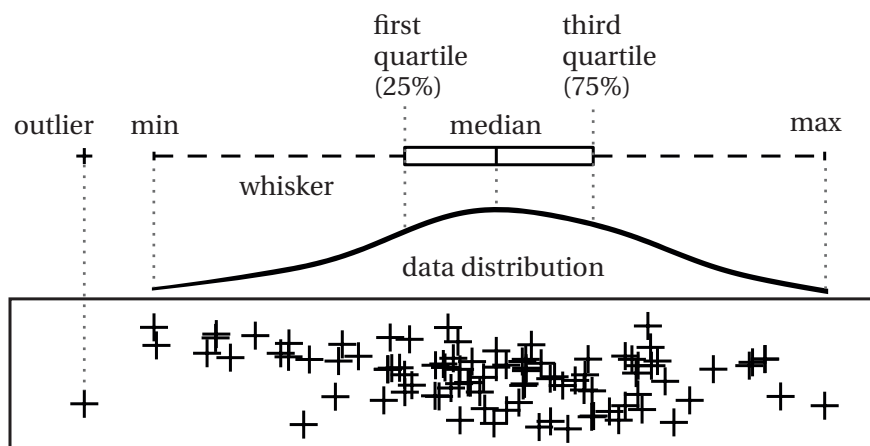


Figure 5.8: Boxplot interpretation.

imperative to clarify that the whiskers of the boxplot are not indicative of the error bars that are associated with a data set.

Fig. 5.9(a-b) shows the boxplots of local graphene lattice points in both relaxed and tented cases with increasing V_{st} , measured from the area with a size of $15 \text{ nm} \times 15 \text{ nm}$. For each lattice point, d_{lat} is the length of the reciprocal lattice vector, and θ is the angle defined by comparing with the horizon, 0° -line drawn in Fig. 5.9(c). The scatter plots with marginal kernel densities are shown in Fig. 5.10.

In the tented case, the median of d_{lat} -distribution in -3° direction shifts from $\sim 5.13 \text{ nm}^{-1}$ to $\sim 4.93 \text{ nm}^{-1}$ when V_{st} increases from 0 to 60 V, while its θ -distribution remain unchanged. Moreover, the median of d_{lat} -distribution in $+57^\circ$ (-66°) direction shifts from ~ 5.06 (5.34) nm^{-1} to ~ 5.22 (5.42) nm^{-1} , and the θ -distribution in $+57^\circ$ (-66°) direction rotates counterclockwise (clockwise) with $\sim 2^\circ$. On the other hand, in the relaxed case, except the median of d_{lat} -distribution in $+67^\circ$ direction and the median of θ -distribution in $+1^\circ$ direction slightly shifts with increasing V_{st} , other distributions remain roughly the same. These shifts in distributions suggest that most of the areas in the tented case are affected by strain transferred from polyimide film, in contrast to the relaxed case, where only a few local areas are changed so that no noticeable trend can be found.

To further verify the origin of the lattice parameter change, STM images of graphene in the tented condition with three different V_b of -0.5 V , 0.5 V , and 1 V at a different area are measured. It is found that the results of graphene surface morphologies and lattice constant distributions remain largely unchanged with different V_b , as shown in Fig. 5.11. This indicates that the tip-sample force is sufficient to lift the sample height, as seen in Fig. 5.3(d), but not enough to change the lattice parameters. Therefore, the change in d_{lat} and θ described above is mainly caused by stretching due to increased indentation depth, not by the tip-induced curvature change during scanning.

A schematic diagram is illustrated in Fig. 5.9(c) to describe the changes in graphene reciprocal lattices and corresponding structure in real space in the tented case with increasing V_{st} . The reciprocal lattices are drawn based on the medians extracted from Fig. 5.9(b) and then are converted into the real space lattice. The changes in the schematic are exaggerated for clarity. It is shown that after increasing V_{st} to 60 V, the graphene experiences an asymmetrical strain distribution, which stretches along $\sim -3^\circ$ (armchair) direction and compresses along $\sim 87^\circ$ (zigzag) direction. The changes in the graphene's reciprocal lattice, $G' = (I + \bar{\epsilon})^{-1}G$, can be used to extract the strain tensor ($\bar{\epsilon}$) [167]:

$$\bar{\epsilon} = \begin{pmatrix} \epsilon_A & \gamma_s \\ \gamma_s & \epsilon_Z \end{pmatrix}, \quad (5.1)$$

where γ_s is the shear strain, ϵ_A and ϵ_Z are the uniaxial strain applied along the armchair and zigzag direction, respectively. Based on the changes in the positions of medians in distributions when V_{st} increases from 0 to 60 V, it is found that $\epsilon_A \approx 4\%$, $\epsilon_Z \approx -4\%$ and $\gamma_s \approx 0$.

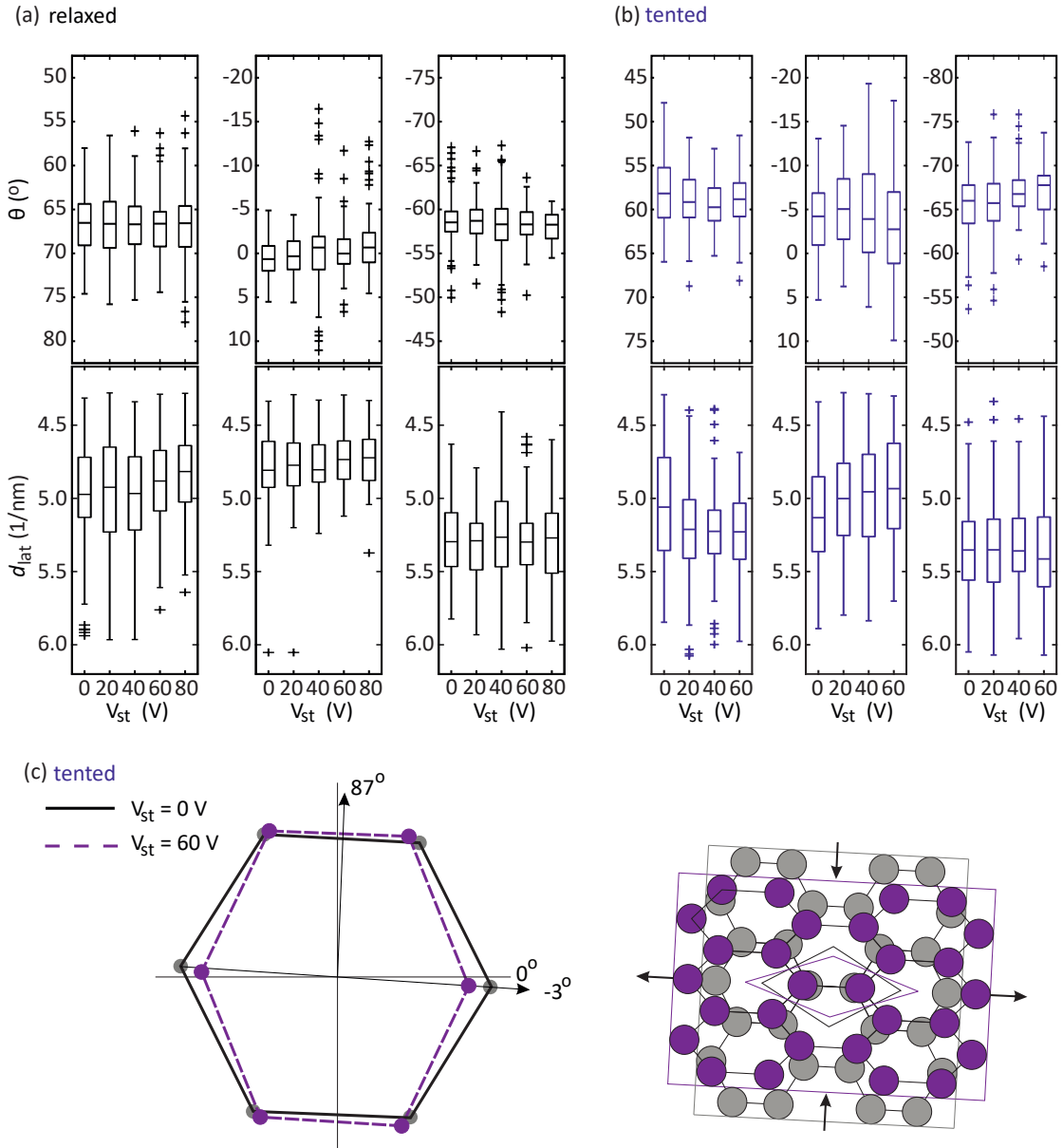


Figure 5.9: Characterization of strain-controllability. The boxplots of local graphene lattice points in (a) relaxed and (b) tented cases with increasing piezoelectric actuator voltage (V_{st}). For each lattice point, d_{lat} is the length of the reciprocal lattice vector, and θ is the angle defined by comparing with the horizon, 0° -line drawn in (c). (c) The schematic summarises how graphene is deformed in the tented case when increasing V_{st} , based on the shifts in the medians extracted from (b). The changes in the schematic are exaggerated for clarity.

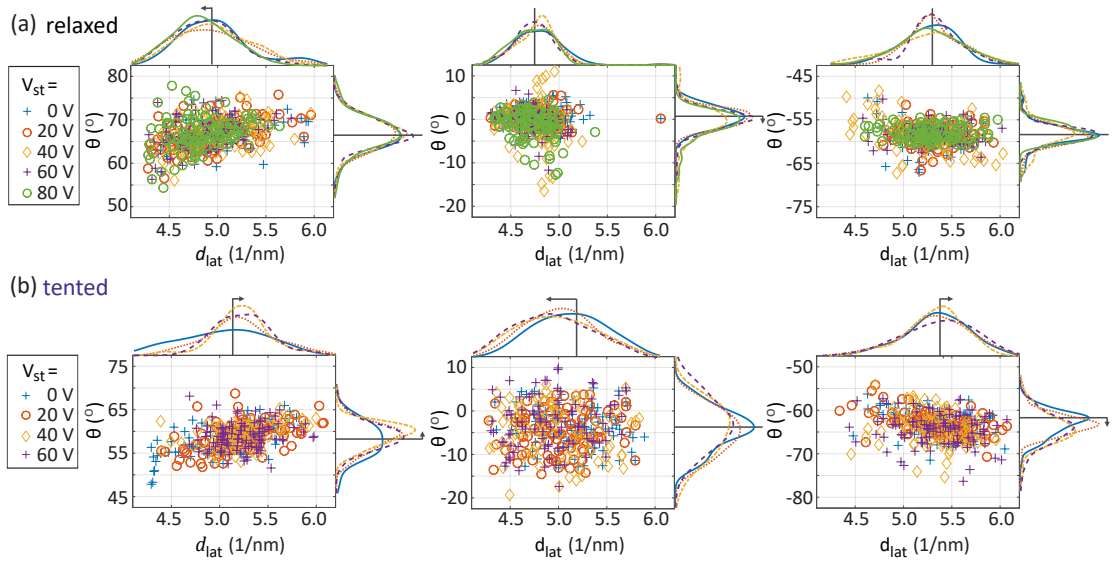


Figure 5.10: Scatter plots with marginal kernel densities of local graphene lattice points in (a) relaxed and (b) tented case with increasing the piezoelectric actuator voltage (V_{st}). For each lattice point, d_{lat} is the length of reciprocal lattice vector, and θ is the angle defined by comparing with the horizon, θ_0 -line drawn in Fig. 5.9(c).

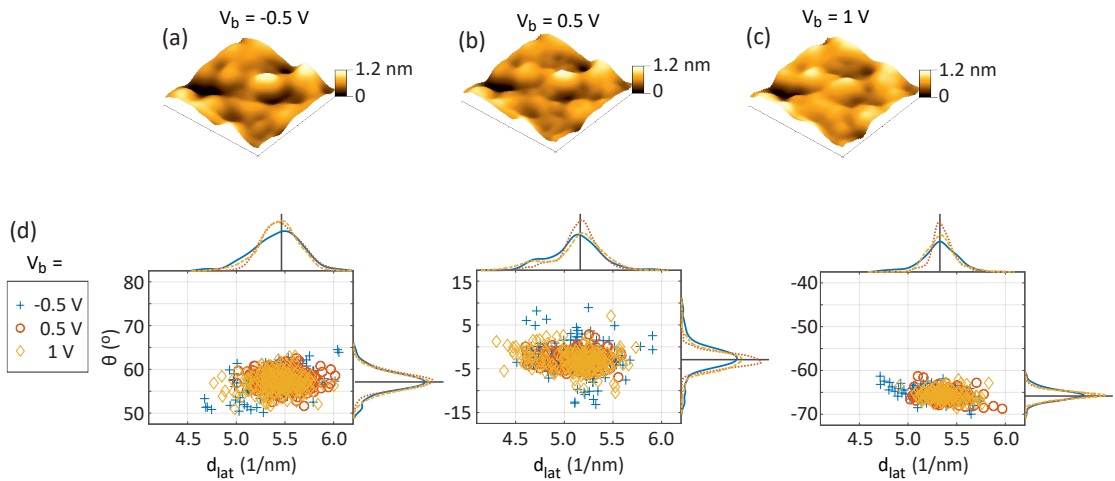


Figure 5.11: (a-c) STM topography images measured at the same area in the tented case with different bias voltages (V_b). (d) The scatter plots with marginal kernel densities of local graphene lattice points analyzed from (a-c). The size of the images is 15 nm x 15 nm.

Chapter 5. In-situ Atomic Level Observation of the Strain Response of Graphene Lattice

The statistical significance confirms that the volume of accumulated data is sufficient to bolster the fitting precision, thereby ensuring the reliability of the measured lattice position distributions. The z-scores, which account for positional variations in both the armchair and zigzag directions, can be calculated using the following equation:

$$z = \frac{\text{observed difference}}{\text{standard deviation}} = \frac{\text{strain}}{\text{fitting precision (\%)}} = \frac{4}{1.9} \approx 2.1. \quad (5.2)$$

This z-score corresponds to a one-tailed confidence level of 98.21%.

5.3 Conclusions

The performance of the strain- and gate- controllable STM sample holder, which employs an in-situ nanoindentation method, has been demonstrated. 2D materials supported by polyimide film with a thickness of $\sim 1 \mu\text{m}$ can be deformed by an indenter with a travel range of $\sim 120 \mu\text{m}$ with nanometer precision using a gearbox in combination with a piezoelectric actuator. Since the sample holder is compact with a size of $\sim 160 \text{ mm}^2 \times 5.2 \text{ mm}$, it can be used not only in STM but also for many other analytic tools, such as AFM and Raman spectroscopy for comprehensive analysis. A series of atomic resolution STM images were obtained to examine the strain response of the graphene lattice to the indentation depth. The variation of STM tip height in the constant current mode was used to trace the polyimide film deflection in the indenting process. The change in the distribution of reciprocal lattices indicated that the graphene in the measured area experienced a tensile strain of 4% in the armchair direction and a compressive strain of 4% in the zigzag direction, in addition to the bending strain induced by the polyimide surface roughness. Such direct observations of strain-induced structural change in reciprocal lattice distribution provide valuable information for future strain engineering applications in 2D materials.

6 Atomic-Scale Determination of Poisson's Ratio in Two-Dimensional Materials

Building on Chapter 5, where we employed a strain- and gate-controllable sample holder, this chapter discusses our experimental approach for measuring the Poisson's ratio of 2D materials, such as graphene and monolayer MoS₂, at the atomic scale. We achieved this by modifying the indenter's shape to induce uniaxial deformation in these materials.

6.1 Introduction

Poisson's ratio (ν) is an essential parameter defining a material's elastic deformation response [168]. It measures the transverse deformation resulting from a specific loading direction and is expressed as the negative ratio of transverse strain to axial strain: $\nu = -\epsilon_{trans}/\epsilon_{axial}$. Conventional materials typically exhibit positive Poisson's ratios ranging from $0.2 < \nu < 0.5$, as they contract perpendicularly to accommodate volume changes during expansion [169].

Interestingly, a variety of natural and synthetic materials with unique geometries, such as re-entrant structures or flexible hinges, can display a broad range of negative Poisson's ratios (NPR) and are classified as auxetic materials [170–172]. These materials exhibit counterintuitive behavior, expanding laterally when stretched and contracting laterally when compressed. Auxetic materials possess remarkable mechanical properties, including shear modulus [173], indentation resistance [174], and fracture toughness [175]. The auxetic effects and subsequent enhancements in other material properties provide immense potential for various applications [176], such as biomedicine [177], sensors [178], fasteners [179], and protective equipment [180].

Auxetic effects have also been observed in several 2D materials in recent studies. For instance, out-of-plane NPRs were found in phosphorene [181] and monolayer arsenic [182], while in-plane NPR was predicted in borophene [183]. Similar to bulk auxetic materials, the auxetic behavior in these 2D materials is primarily attributed to their puckered crystal structures

Chapter 6. Atomic-Scale Determination of Poisson's Ratio in Two-Dimensional Materials

[184]. Additionally, it has been reported that wavy graphene exhibits significant in-plane NPRs [185], and chemically modified graphene films can possess tunable in-plane NPRs due to the suppression of microstructural origins, such as wrinkled close-packed laminates, disordered stacks, and delamination areas, caused by stretching [186]. Likewise, introducing disorders to create a crumpled conformation of graphene can reduce in-plane Poisson's ratio and increase out-of-plane Poisson's ratio as a consequence of the de-wrinkling effect [187–189].

Intriguingly, NPR in 2D materials can also be induced solely by chemical composition and electronic structure effects rather than geometry. For example, it has been theoretically predicted that graphene exhibits intrinsic in-plane NPR when subjected to a uniaxial strain of approximately 20% along the armchair direction, resulting from the change in bonding configurations [190–192]. Beyond graphene, monolayer TMdCs in their 1T phase are also predicted to display intrinsic in-plane NPR due to strong orbital couplings [193].

To date, only a few studies have measured Poisson's ratio in 2D materials at the macroscopic scale [186, 194, 195]. However, for an accurate experimental determination of the Poisson's ratio of 2D materials, it is crucial to measure their strain response at the atomic scale to (1) avoid contributions from various defects and domain boundaries, (2) enable comparison between the direction of applied uniaxial strain and lattice orientation, and (3) precisely calculate the Poisson's ratio through changes in lattice parameters. Nonetheless, directly measuring lattice changes at the atomic scale while simultaneously applying uniaxial stress poses a significant challenge, given the difficulty of maintaining flexibility and stability at low temperatures under UHV conditions. As a result, there have been no experimental reports of Poisson's ratio for 2D materials at the atomic scale to date.

6.2 Experiment Design

To measure the Poisson's ratio of 2D materials at the atomic scale, we modified the indenter into a ridge-like shape, as depicted in Fig. 6.1. 2D materials were transferred onto a polyimide film and secured by two rod-shaped Pd clamps deposited along the edges. The polyimide film was attached on both sides using epoxy adhesive and deformed controllably by raising the indenter with a gearbox. STM measurements were performed near the apex of the deformed region. The bottom-right inset of Fig. 6.1 displays a photograph of the experimental setup.

This measurement design is primarily driven by two factors. First, STM tip should be positioned near the ridge's crest, which is due to the predominant uniaxial strain experienced by the polyimide film in the direction perpendicular to the ridge. As the indenter deforms the polyimide film, strain induced perpendicularly by Poisson's effect becomes negligible near the fixing point at the ridge's crest. Second, the 2D material near the ridge's crest demonstrates the most pronounced Poisson's effect, as it is located farthest from the two fixed edges.

Practically, as the STM tip reflection in this structure is invisible under the camera (Fig. 6.2), the tip approach is more challenging than in the sample structure presented in Chapter 5,

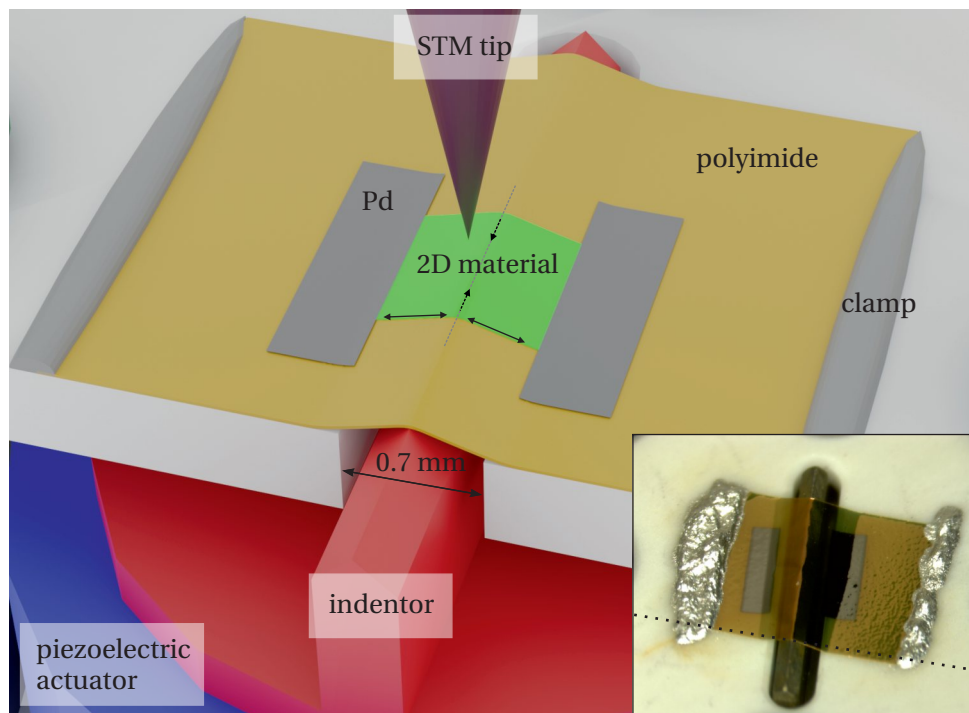


Figure 6.1: Experimental setup for measuring the Poisson's ratio of 2D materials. 2D materials are transferred onto a polyimide film, then deformed by an indenter to a ridge-like morphology. To secure the 2D materials, two rod-shaped Pd clamps are deposited along the edges. The polyimide film is attached on both sides using epoxy adhesive. STM measurements are performed near the apex of the deformed region. The bottom-right inset displays a photograph of the experimental system.

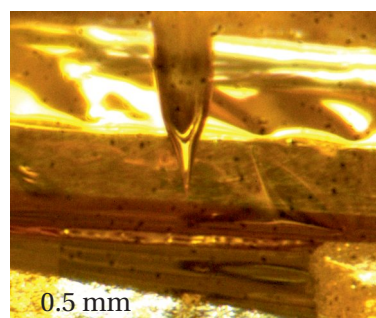


Figure 6.2: Photo of an STM tip-sample junction for Poisson's ratio measurement.

which featured lower height variation. The tip is first approached at the surrounding flat area and carefully moved to the deformed region. Additionally, due to the measured surface's steep slope, tilt correction must be applied to STM images to reliably calculate lattice parameters.

6.3 Results

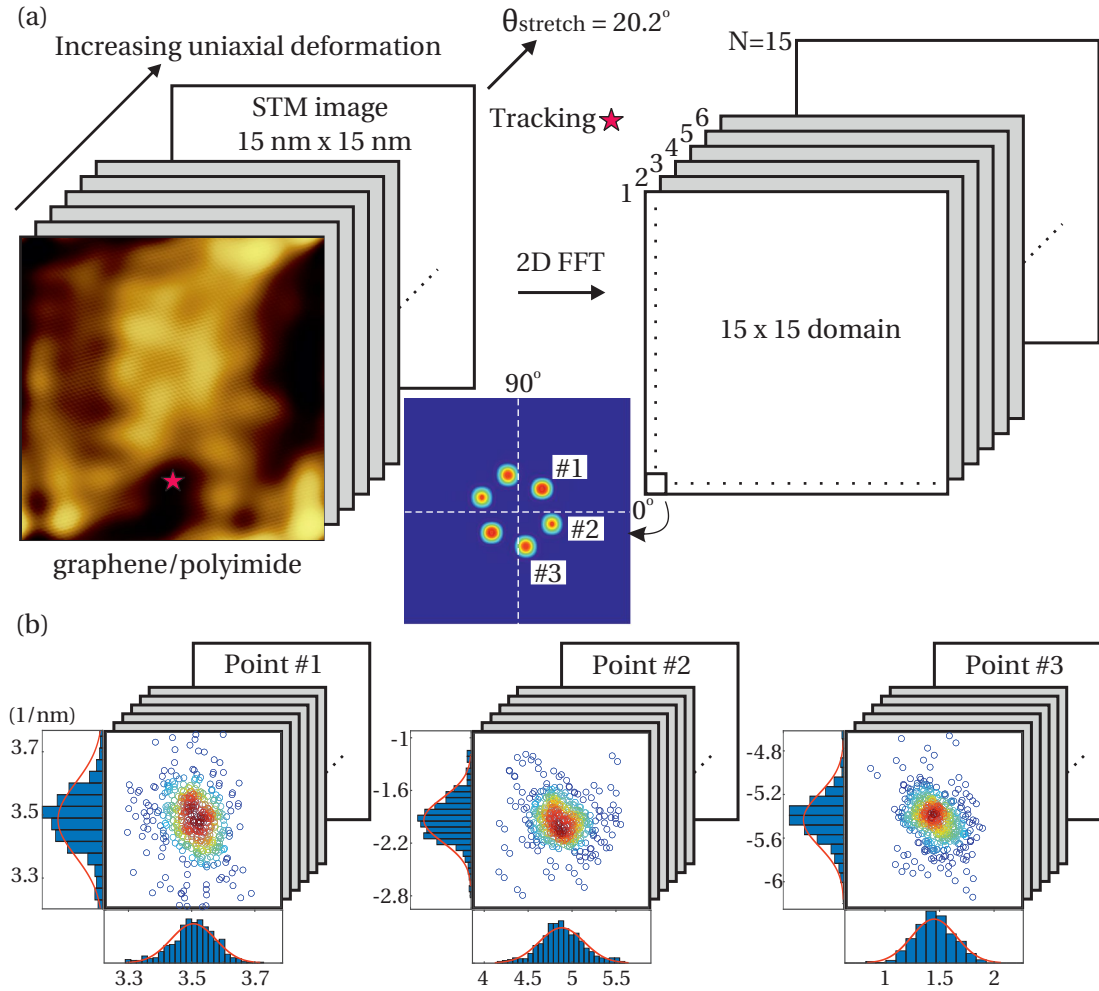


Figure 6.3: Evaluation of lattice parameter changes with increasing uniaxial strain. (a) Strain is increased by raising the indenter height using the piezoelectric stack. By tracking the topography feature marked by a red star, the stretching angle is determined to be 20.2° . To identify and obtain local lattice parameter positions, 2D FFT is employed to convert each local area ($1 \text{ nm} \times 1 \text{ nm}$) into reciprocal space. (b) Scatter histogram plot of local lattice points #1-3 from the entire image, with each point colored based on the spatial density of nearby points.

In order to obtain the Poisson's ratio within a single crystalline domain, a series of STM topography images were measured with increasing uniaxial deformation by increasing indenter height using the piezoelectric actuator. Fig. 6.3(a) shows the results for graphene transferred on the polyimide film. The images are numbered in the order of increasing strain. By tracking

the topography feature denoted by a red star, the stretching angle is determined to be 20.2° . However, to detect the length changes by fitting the atomic corrugations in real space is challenging because changes are in a range of a few pm considering the graphene lattice constant and the applied strain level. Therefore, we use the statistical information of reciprocal lattice points to calculate the Poisson's ratio based on the length changes in the directions parallel and perpendicular to the uniaxial strain.

To obtain the positions of reciprocal lattice points, 2D FFT is first used to convert each local area with a size of $1 \text{ nm} \times 1 \text{ nm}$ into reciprocal space and afterward, Gaussian fitting is applied with five fitting parameters: the amplitude and two lateral widths and positions. The positions of local reciprocal lattice points #1-3 obtained from each local area are then summarized into scatter histogram plots, as shown in Fig. 6.3(b), with broad distributions due to the local curvature induced bending strain [196, 197]. To extract the global stretching strain induced by the indenter height change, Gaussian fittings are used to determine their center positions.

Fig. 6.4 shows the atomic resolution STM image ($N=1$ in Fig. 6.3) of graphene/polyimide subjected to a uniaxial strain. Lattice constants, a_3 and a_1 , corresponding to the blue and orange zigzag directions, are 2.27 \AA and 2.12 \AA , respectively, calculated by the equation: $a_i \cdot \tilde{a}_j = 2\pi\delta_{ij}$ ($i, j = 1, 3$), using the mean positions of reciprocal lattice points #1 and #3 (\tilde{a}_1 and \tilde{a}_3) obtained in Fig. 6.3. The applied uniaxial stretching strain, which is marked as the black arrow, is along a direction 5.3° relative to the blue zigzag directions.

Unit lengths parallel and perpendicular to the stretch were obtained by projecting a_3 and a_1 , respectively. Fig. 6.5 displays the scatter plot of unit length changes of graphene/polyimide in these two directions with increasing uniaxial deformation (increasing image number). The error bar for each data point is approximately 1.9% in both directions (stretch and perpendicular to the stretch), derived from the precision of Gaussian fitting, which is omitted from the figure for visual clarity.

Interestingly, the unit length along the stretch does not consistently increase with increasing deformation. Instead, it exhibits an oscillating pattern of growth and decline in a linear manner. The linear fit applied to the scattered data points yields a slope of 1.8. By comparing the line's two endpoints, the relative strains parallel and perpendicular to the stretch direction are calculated to be 1.90% and 1.23%, with z-scores of 1 and 0.65, translating into one-tailed confidence levels of 84.13% and 74.22%, respectively. Consequently, the ratio of these two strains results in an in-plane Poisson's ratio of -0.65.

The experimental procedure for measuring the Poisson's ratio of graphene is repeated for monolayer MoS_2 . Fig. 6.6 displays the scatter plot of unit length changes of monolayer MoS_2 /polyimide parallel and perpendicular to the stretch with increasing uniaxial deformation (increasing image number). Similarly, by tracking distinct topography features, the stretch direction is determined to be 16.9° relative to one of the zigzag directions. Utilizing the fitting line's two endpoints, the relative strains parallel and perpendicular to the stretch direction are found to be 3.11 % and 2.96 %, with z-scores of 1.64 and 1.56, translating into one-tailed

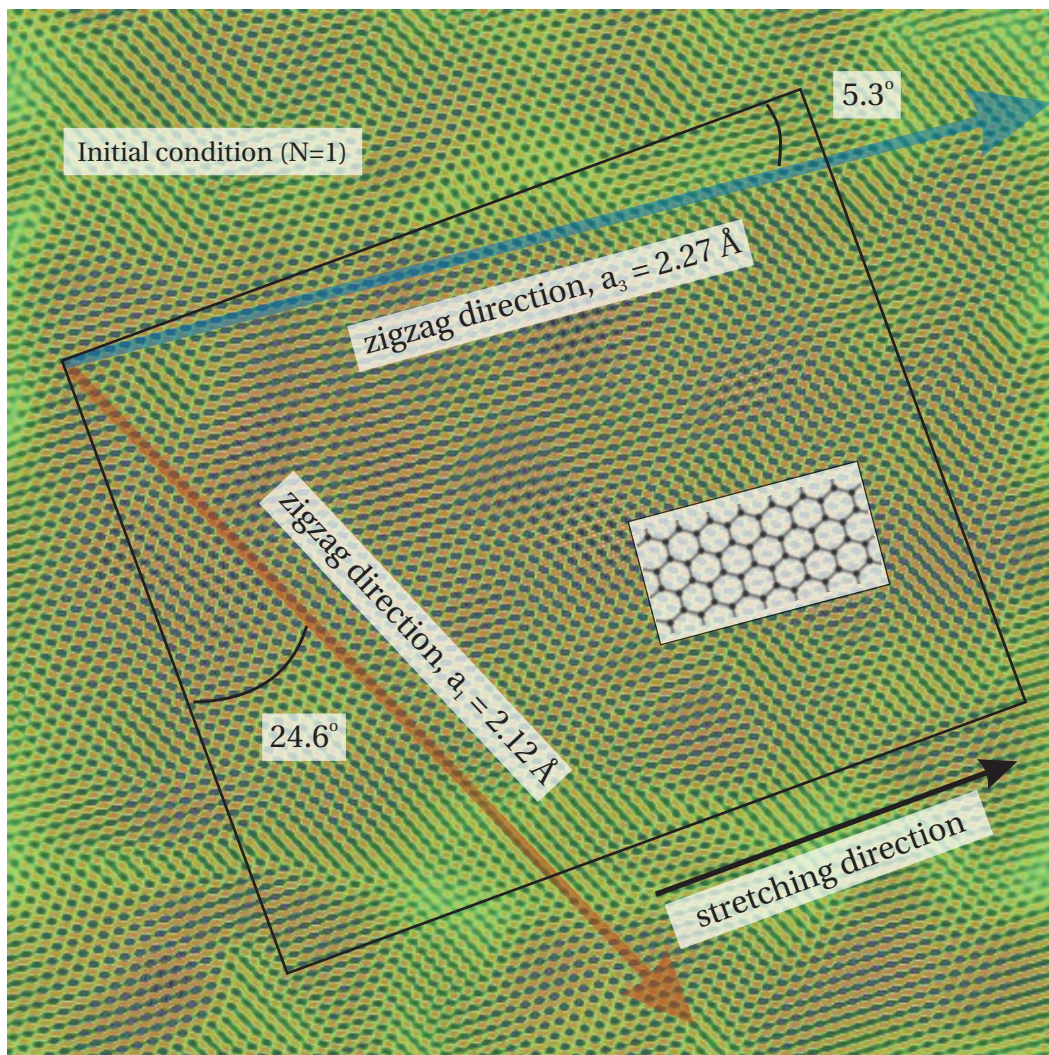


Figure 6.4: Atomic resolution STM image of graphene/polyimide under uniaxial strain. The image is processed by a high-pass filter to display the lattice points more clearly. The applied uniaxial strain is 5.3° relative to one of the zigzag directions. Two lattice constants corresponding to different zigzag directions (shown in blue and orange) are calculated using the positions of reciprocal lattice points obtained in Fig. 6.3. The inset illustrates the crystallographic orientation of the measured graphene.

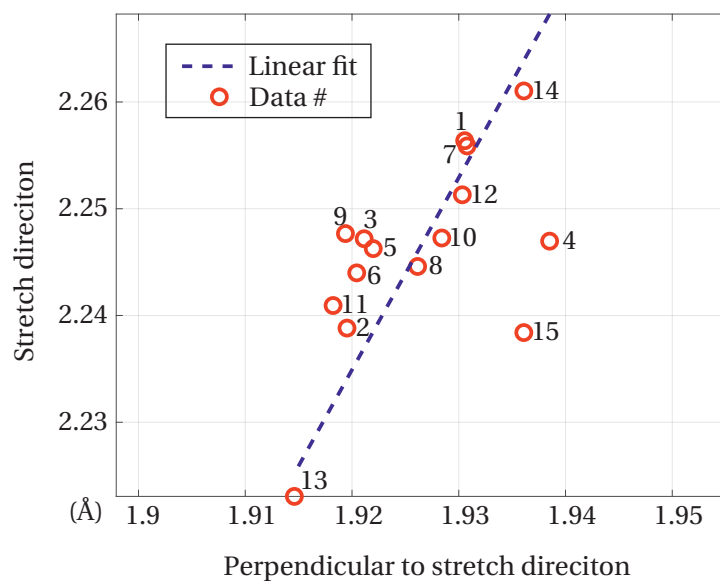


Figure 6.5: Unit length changes of graphene parallel and perpendicular to stretching. Scattered data points are labeled with the number from each image. The stretch is along a direction of 5.3° to one of the zigzag directions.

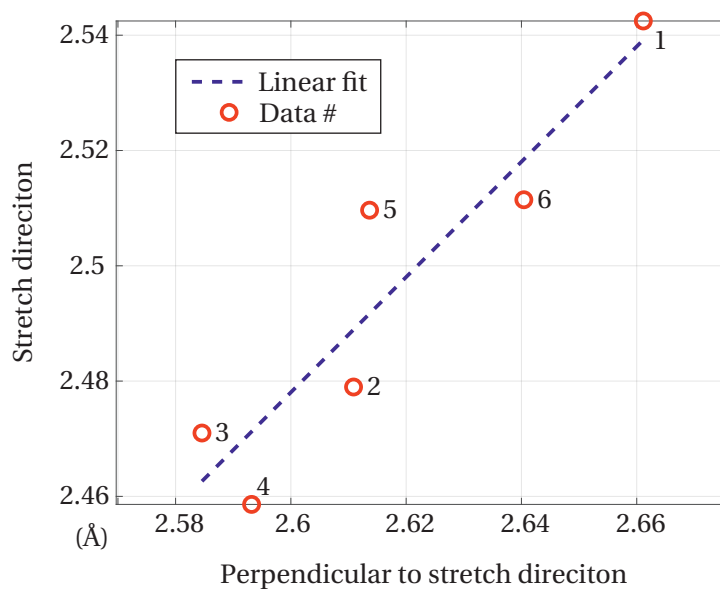


Figure 6.6: Unit length changes of monolayer MoS_2 parallel and perpendicular to stretching. Scattered data points are labeled with the number from each image. The stretch is along a direction of 16.9° to one of the zigzag directions.

Chapter 6. Atomic-Scale Determination of Poisson's Ratio in Two-Dimensional Materials

confidence levels of 94.95% and 94.06%, respectively. The result leads to an in-plane Poisson's ratio of -0.95.

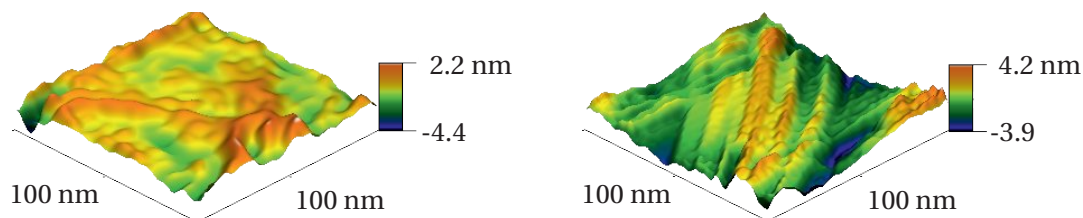


Figure 6.7: 3D view of local wrinkles in STM topography images of graphene/polyimide.

First-principles calculations and molecular dynamics simulations have reported positive in-plane Poisson's ratios (0.1-0.3) for graphene [188, 191, 198, 199] and monolayer MoS₂ [200–204] in the elastic regime at small strains (<3%). The strain dependence of Poisson's ratios differs based on the direction of applied uniaxial strain [192, 198, 199]. In graphene, increasing strain along the armchair direction gradually decreases Poisson's ratio, transitioning from positive to negative at approximately 20% strain due to increased bond angles. However, in the zigzag direction, a higher strain of approximately 65% is required to induce negative Poisson's ratios due to increased bond lengths. Alternatively, NPRs can be obtained by creating porous structures, utilizing the rotation of the relative rigid domain [205]. It has also been shown that when the out-of-plane corrugations, such as ripples, are controllably introduced by defects [185, 188], oxidation [198] or hydrogenation [189], the Poisson's ratio can be widely tuned and become negative, owing to the de-wrinkling effect [187, 198].

As our Poisson's ratio measurement is conducted under the conditions of small strains and free of defects and domain boundaries, the de-wrinkling effect plays the dominant role in our observed in-plane NPR. In both Fig. 6.5 and Fig. 6.6, it can be seen that when uniaxial strain increases, the measurements first show a trend of reducing lattice constants, indicating the formation of local wrinkles, followed by a de-wrinkling process that increases the lattice constants. This alternating wrinkling and de-wrinkling process results in the oscillating trend of observed unit length changes.

The measurement area of 15 nm × 15 nm provides sufficient statistical information for Poisson's ratio determination and avoids distortion from the STM piezo scanner. Although the Poisson's ratio calculated from this measurement size is less affected by the de-wrinkling effect at the micrometer scale, it is significantly influenced by the formation of local wrinkles at the nanometer scale. STM topography images in Fig. 6.7 confirm the presence of local graphene wrinkles with a size of approximately 10 nm in the surrounding area. It has been reported that the formation of such local wrinkles in 2D materials can be triggered by various mechanisms, including the transfer process of 2D material [206, 207], temperature changes due to different thermal expansion coefficients between the 2D material and supporting substrates [208, 209], and strain relaxation during the application of uniaxial stress [41].

6.4 Conclusions

For the first time, the measurement of the Poisson's ratio of 2D materials, including graphene and monolayer MoS₂, has been reported at the atomic scale. The experiment was achieved by modifying the indenter and sample configuration within the strain- and gate-controllable sample holder. It was observed that both graphene and monolayer MoS₂ exhibited negative Poisson's ratios, which may be attributed to the previously proposed de-wrinkling effects. Additionally, the findings revealed a pattern of alternating wrinkling and de-wrinkling processes as uniaxial deformation increased. This suggests that the formation of local out-of-plane corrugations, such as wrinkles or ripples, can be inevitable and should be considered when using supported 2D materials for practical strain engineering applications. Characterizing Poisson's ratios of 2D materials at the atomic scale and experimentally observing wrinkling behavior would provide a deeper understanding of the elastic deformation behavior of supported 2D materials.

7 Characterization of Strain Engineered Metal Contact on Monolayer MoS₂

This chapter represents the strain engineering on the MoS₂-metal interfacial interactions by controlling the interface roughness. The interface interactions and the contact behavior of monolayer MoS₂ are characterized by using XPS, AFM, and Raman spectroscopy.

7.1 Introduction

One of the major challenges of semiconductor device research is the contact between the semiconductor and metal electrodes for the efficient injection of charge carriers into the conduction channel. Therefore, understanding and designing the semiconductor-metal interface has been an important issue [210], underpinning the performance of transistors [16], batteries [211], and catalysis [212]. Moreover, as the size of electronic devices scales down to sub-20 nm, the metal contact resistance starts to dominate the total device resistance [213]. Particularly for 2D semiconductors, the contacts of 2D devices usually possess a large Schottky barrier and rarely follow the Schottky-Mott model because of interfacial effects. As high parasitic contact resistance has been identified as a critical limiting factor in TMdCs-based device performance, understanding the interface properties between 2D materials and metal is critical.

Extensive research has been conducted into the interaction between 2D TMdCs and metal electrodes. For metals that are prone to oxidation, such as Ir, Cr, Sc, Ti, and Y, the interaction with the S atoms is strong, [214–216] and alters the atomic structure of the MoS₂, resulting in extensive disorder. For inert metals, such as Au, it has been shown that the Au interacts with the MoS₂ through van der Waals forces [217–219], or covalent-like quasi-bonding [220]. Although the intrinsic MoS₂ structure is not affected through contact with Au, the orbital hybridization between MoS₂ and Au was still observed, leading to modification of the bandgap and conductivity of the MoS₂ [218, 219, 221].

However, the reported values of contact resistance and charge carrier injection efficiency vary from sample to sample and depend on the measurement method. One of the reasons

for this is the extreme sensitivity of 2D materials to surface adsorbates or environments, which can seriously limit the realization of Ohmic contacts in 2D devices. The complicated interfacial states induced by defects, adsorbates, orbital hybridization, or chemical disorders can also be easily formed at 2D/metal contact interfaces. Furthermore, the atomically thin nature of 2D materials enables their crystal structure to be easily damaged during standard device fabrication processing, such as e-beam lithography and physical vapor deposition of metals, resulting in significant Schottky barrier or interfacial states at the 2D/metal interface. Strain is another critical extrinsic stimulus. Strain is inevitable in 2D materials, regardless of whether the film is suspended or supported. Furthermore, strain is known to alter the physical and chemical properties, such as the band gap, charge carrier effective masses, dielectric properties, chemical reactivity, and many more. For example, at the interface between MoS₂ and Au, the combination of charge and strain induce the 2H-to-1T phase transition of MoS₂ [222], which largely changes the properties of monolayer MoS₂ from semiconducting to metallic.

This chapter investigates the dependence of 2D-metal interface interactions on contact material in conjunction with the strain effect. The experiment is carefully designed to isolate and examine only the intended effects of material and strain while excluding any other potential influences. The contact interfaces between monolayer MoS₂ and several inert metals, such as Au, Pd, and HOPG, are studied using XPS, Raman spectroscopy, and AFM. These metals are chosen as they are the most widely used contact materials. The 2D semiconductor-metal interfaces are formed by transferring monolayer MoS₂ onto pre-fabricated metal surfaces to avoid fabrication-induced disorder [223]. Transferring the as-grown monolayer MoS₂ onto targeted metal surfaces also reduces the area of multilayer regions, which are commonly seen in exfoliation methods that could affect the interpretation of the experimental data [224, 225]. Furthermore, the interfaces are easily accessed without the limitation of metal film thickness since MoS₂ is on top of the metal substrate [215, 224]. MoS₂ transferred on HOPG is used as a reference to distinguish the contact material effects from the other effects, such as defects and grain boundaries. Using XPS, it is found that when monolayer MoS₂ is brought in contact with Au or Pd, the additional interface states emerge due to the metal-S interaction. Additionally, the strain dependence of interface states is studied by transferring monolayer MoS₂ onto the pre-fabricated metal surfaces with different roughness. XPS spectra indicate that the peak positions of interface states depend on the degree of strain. Analyzing Raman spectra and AFM images together shows that the MoS₂ strain increases with metal surface roughness. However, once the metal surface roughness is over a certain threshold, the strain and doping concentration on MoS₂ are reduced due to delamination.

7.2 Metal-S Interactions

A number of different metals have been explored for use as contacts in MoS₂ based devices. To exclude the effect of substrate roughness, in this study, the highly oriented pyrolytic graphite (HOPG) is used as the substrate, upon which the metal film with a thickness of 50 nm is

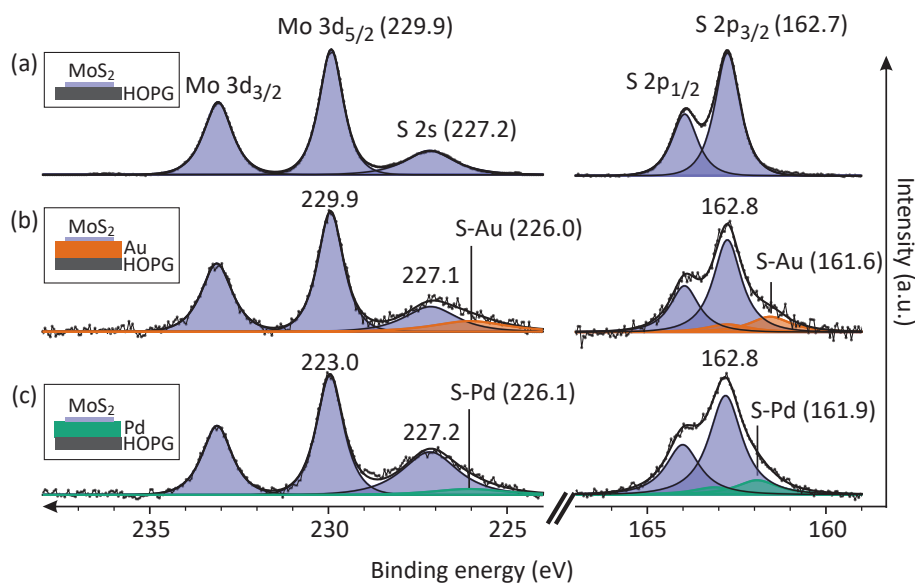


Figure 7.1: MoS₂/Au and MoS₂/Pd interfacial interaction. Normalized XPS spectra of the Mo 3d, S 2s, and S 2p core levels of monolayer MoS₂ on three different substrates: (a) HOPG, (b) Au-deposited HOPG, and (c) Pd-deposited HOPG. Peaks from MoS₂ are marked as purple. S 2s (2p) peaks for S-Au and S-Pd interaction are marked as orange and green, respectively.

deposited. Since a bottom contact structure is used, with the metallic substrate beneath the MoS₂ layer, XPS could be used to characterize the interfacial interaction. As shown in Fig 1, three different MoS₂- metal interfaces were studied by transferring monolayer MoS₂ onto: HOPG (MoS₂/HOPG), Au-deposited HOPG (MoS₂/Au/HOPG), and Pd-deposited HOPG (MoS₂/Pd/HOPG).

Fig. 7.1(a) shows the core-levels spectra of MoS₂/HOPG with visible peaks of Mo 3d_{3/2} (233.1 eV), Mo 3d_{5/2} (229.9 eV), S 2s (227.2 eV), S 2p_{1/2} (163.9 eV), S 2p_{3/2} (162.7 eV), consistent with previous findings [226]. Using the relative sensitivity factor of 5.77 for Mo 3d_{5/2} and 1.25 for S 2s, the Mo:S ratio is found to be ~1:2. Together with the absence of Mo-oxide doublet peaks (236 eV) [227], it suggests that our sample has a low defect concentration and is not degraded during the transfer process.

Fig. 7.1(b) shows the spectra for MoS₂/Au/HOPG, both S 2p and S 2s spectra are broad compared to the peaks of the MoS₂/HOPG spectra [218, 219, 228, 229]. The broadening is attributed to the emergence of new S-Au peaks in S 2s and S 2p in the MoS₂/Au/HOPG, which show a uniform shift toward lower binding energies compared to those of the MoS₂/HOPG film. The new S 2p and S 2s appear at 162.7 and 226.1 eV, ~1.1 and ~1.2 eV lower than that of the S-Mo peak in S 2p and S 2s spectra, respectively. There is almost no obvious difference in the binding energies of Mo 3d peaks between the MoS₂/HOPG and MoS₂/Au/HOPG. Similar peaks were observed in the MoS₂/Pd/HOPG (Fig. 7.1(c)), S-Pd peaks were observed at 161.9 and 226.1 eV, which have less separation to the S-Mo peak in S 2p and S 2s spectra than that of the S-Au peaks.

The presence of additional S-Au (Pd) peaks is attributed to the metal-S interaction at the interface. The metal-S interaction forms a weak covalent bond between the bottom S and metal atom, which induces electron accumulation. The accumulated electron around S will reduce the binding energy [159]. The difference in binding energy shift between the S-Pd and S-Au peaks can be explained by the Mulliken population analysis done by Kang, J. et al., which indicates the covalency in chemical bonding [133]. The maximum bond Mulliken populations are 0.67, 0.39, and 0.19 for S-Mo, S-Pd, and S-Au, respectively. A higher Mulliken population indicates stronger covalent bonding. Since S-Pd and S-Au peaks feature lower values of maximum bond Mulliken populations compared to the intrinsic S-Mo peak, the S peaks are expected to be located at lower binding energy. This trend is consistent with our observations that the order of these peak positions follows S-Mo, S-Pd, and S-Au. On the other hand, the broadening of Mo peaks is also found because of the simultaneous environment change of Mo atoms. The FWHM of Mo 3d_{3/2} and Mo 3d_{5/2} peaks of MoS₂/Au/HOPG and MoS₂/Pd/HOPG is increased from ~0.9 and ~0.8 eV to ~1.1 and ~1.0 eV, respectively, which aligns well with the shift of the S 2S and S 2p peaks. However, assigning new components of Mo 3d peak was not possible due to the limited XPS resolution.

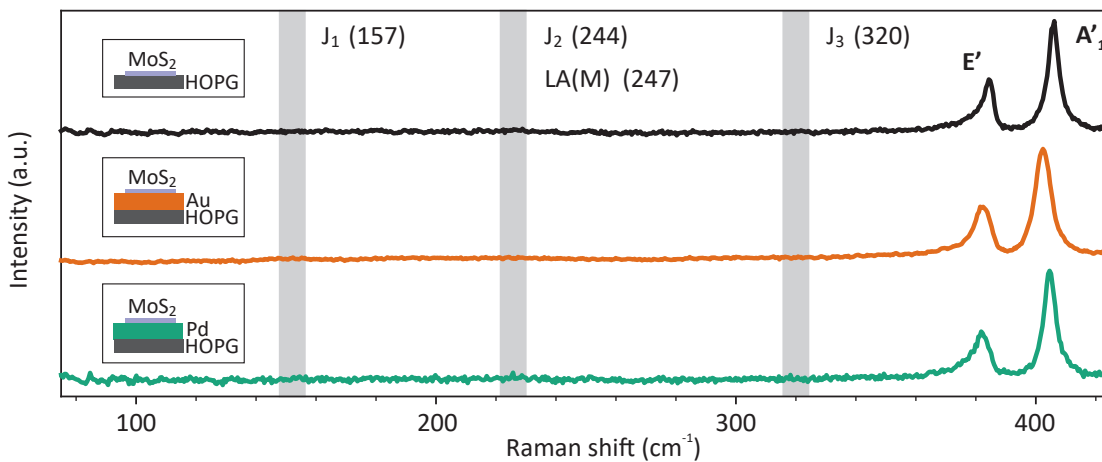


Figure 7.2: Absence of modes for 1T phase and defects in the normalized representative Raman spectra of MoS₂/HOPG, MoS₂/Au/HOPG, and MoS₂/Pd/HOPG.

It was reported that defects [230–232] and phase transition [233–237] can also trigger peaks emerging at lower binding energy shoulders in XPS spectra. To verify this, Raman spectroscopy is performed to examine the defect density and whether the main features of the 1T' octahedral structure exist, as shown in Fig. 7.2. The absence of LA(M) mode gives an upper bound on the defect density of $<10^{13} \text{ cm}^{-2}$ in our sample condition (inter-defect distance $<3.2 \text{ nm}$) [238]. Moreover, except for E' and A₁' peaks, the other three characteristic peaks of 1T phase at ~157 (J₁), ~224 (J₂), and ~320 cm⁻¹ (J₃) are not observed. Therefore, the defects and the phase transition are excluded as the origin of the new peaks.

7.3 Engineering Interface Roughness

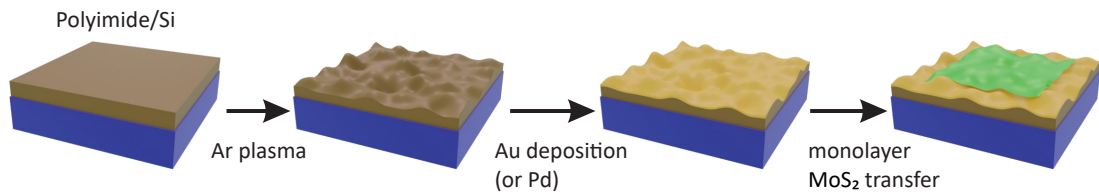


Figure 7.3: Schematic of our method to investigate monolayer MoS₂/metal interactions with increasing interface roughness. The monolayer MoS₂ is transferred onto the Au-deposited or Pd-deposited polyimides treated with increasing Ar plasma time.

To elucidate the surface roughness effect on the MoS₂-metal interface, a polyimide/Si substrate is used. A polyimide substrate was chosen because the surface roughness can be controlled via exposure to an Ar plasma. As shown in Fig. 7.3, the polyimide film supported by the silicon substrate is exposed to Ar plasma, which roughens the surface, with a controlled reaction time ranging from 0 min to 14 mins. Then, Au or Pd films with a thickness of ~50 nm was evaporated on the as-treated polyimide film with the increased surface roughness. Finally, the monolayer MoS₂ is transferred onto the metal coated polyimide films using a wet etching method [154]. The following experiments are performed both on the MoS₂/Au/polyimide and MoS₂/Pd/polyimide. Since both experiments point to the same conclusion, the results for Au and Pd are presented in the manuscript and the supplementary information, respectively.

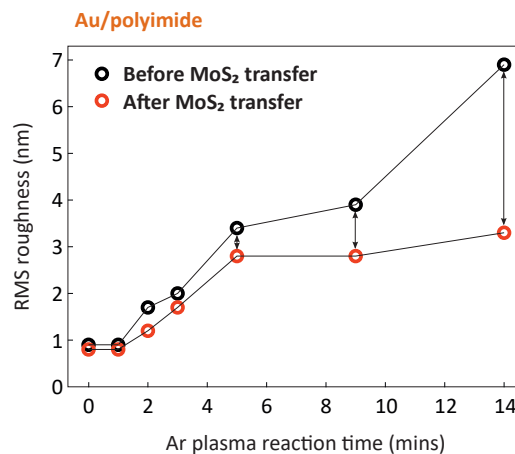


Figure 7.4: Surface roughness of Au-deposited with increasing Ar plasma reaction time before and after transferring monolayer. Root-mean-square (RMS).

Fig. 7.4 shows the root-mean-square (RMS) surface roughness of Au/polyimide and MoS₂ Au/polyimide with increasing Ar plasma reaction time, which is calculated from AFM topography images (AFM figures are in Fig. 7.6). RMS roughness of both surfaces has a positive correlation with Ar plasma reaction time. However, the difference in roughness between the two films increases as the Ar plasma reaction time increases. As the Ar plasma time increases,

the roughness of Au/polyimide continues to increase, while that of MoS₂/Au/polyimide does not increase significantly and is almost constant from 5 min onwards.

To map the topography of the Au/polyimide before and after transferring MoS₂, as shown in Fig. 7.5(a), tapping mode AFM was used. When the 50 nm Au film is evaporated on the polyimide surface, it forms a homogeneous granular structure. After transferring MoS₂ on the Au surface (Fig. 7.5(b)-(c)), the surface structure does not follow the granular structure of the Au film but shows an inhomogeneous surface structure. The difference in morphology before and after MoS₂ transfer is more pronounced as the polyimide substrate becomes rougher, consistent with the results in Fig. 7.5. Fig. 7.5(c) and (d) show enlarged AFM topography and phase images. Phase imaging in AFM captures the phase shift signal of the cantilever oscillation in tapping mode, which is sensitive to variation in material composition, adhesion, friction, viscoelasticity as well as other factors[157]. As shown in Fig. 7.5(d), the morphology change of MoS₂ surface is more clearly visible in the phase images. As plasma treatment time increases by more than 3 min, black dot-like features emerged. The black dot in the phase image is located at protruded areas in the topography image, where the MoS₂ is strongly contacted with the Au film (marked with green arrows, see the overlay in Fig. 7.7). The density of these areas reduces as the plasma duration increases, reflecting a reduction in the MoS₂ area that is intimately coupled to the metal surface, i.e. more of the MoS₂ is suspended. This suspension of MoS₂ on metal surfaces was previously reported when MoS₂ is exfoliated by metal surfaces [225]. In contrast to the MoS₂/Au/polyimide morphology, the phase images of Au/polyimide show only granular features and do not change even as plasma duration increases (Fig. 7.8). The formation of cracks is observed after MoS₂ transfer onto the rough surface after 14 min of plasma treatment on polyimide, marked with purple arrows in Fig. 7.5(b) (an enlarged image is shown in Fig. 7.9). Inside the cracks, the exposed metal film with a granular structure can be seen. The density of these cracks increases with surface roughness, as shown in the optical microscopy image in Fig. 7.5(e).

7.4 Strain Dependent Interfacial Interactions

Having demonstrated the dependence of the morphology change of transferred MoS₂ on the substrate roughness, Raman spectroscopy is used to characterize its effect on the interface interaction. Fig. 7.10(a) shows the normalized Raman spectra of monolayer MoS₂/Au/polyimide with increasing Ar plasma reaction time. The in-plane E' and the out-of-plane A₁' vibrational modes were observed at 385.1 cm⁻¹ and 404.2 cm⁻¹, respectively. Their intensity is normalized by the A₁' peak. For each condition, ten spots on each sample were measured and averaged. The peak at 385.9 cm⁻¹ is used as our zero-strain reference [225]. The strain is measured by using shifts in E' peak with its linear relationship of -5.2 cm⁻¹/‰ to strain [69]. For estimation of doping concentration, the strain-induced peak shift in A₁' mode is first corrected by the linear relationship (1.7 cm⁻¹/‰), and then the doping concentration is calculated by its linear relationship to A₁' peak shift (-2.2 cm⁻¹/10¹³ cm⁻²) [239], where the peak at 406.5 cm⁻¹ in the MoS₂/HOPG is used as our zero-doping reference. Strain and doping values extracted from

7.4 Strain Dependent Interfacial Interactions

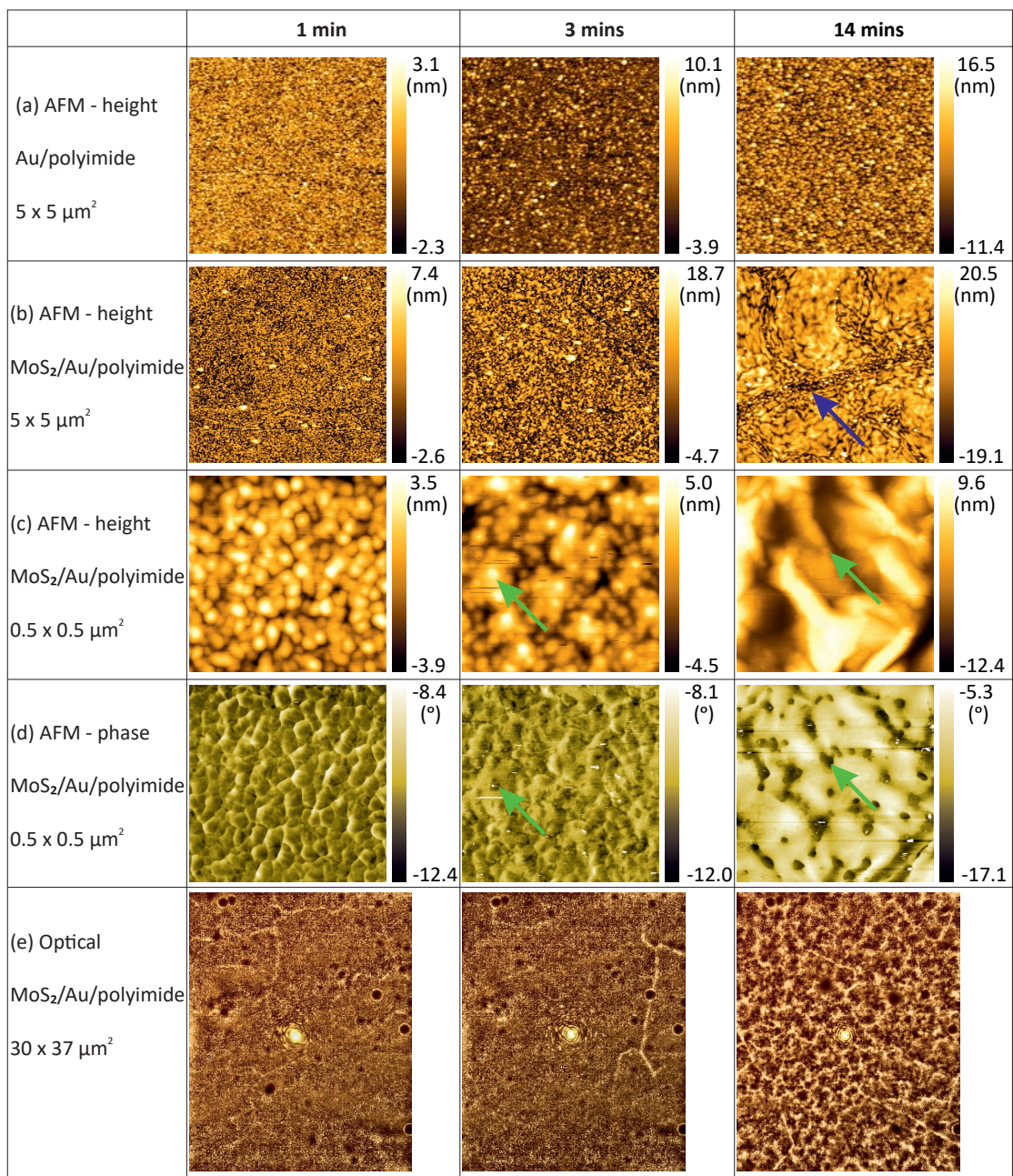


Figure 7.5: Representative AFM topography images of Au/polyimide (a) before and (b) after transferring the monolayer MoS₂ with increasing Ar plasma reaction time from 1 min, 3 mins, to 14 mins. Higher resolution AFM (c) topography and (d) simultaneously measured phase images of MoS₂/Au/polyimide. (e) Optical images. Focused green laser spots are centered in each image.

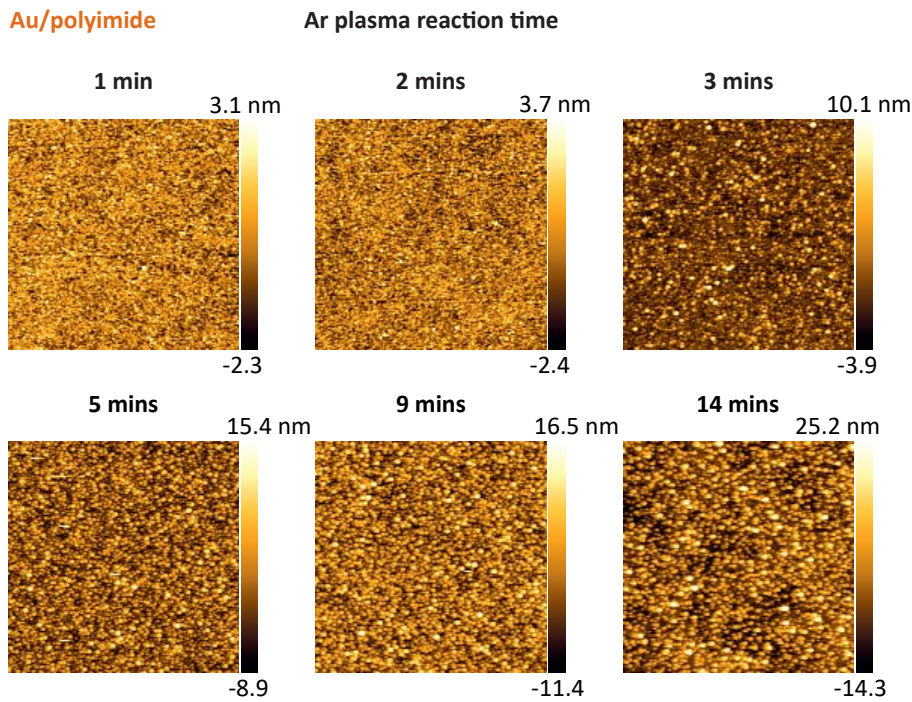


Figure 7.6: Representative AFM topography image of Au/polyimides with increasing Ar reaction time. The image size is $3 \times 3 \mu\text{m}^2$.

Sample	Ar plasma		Raman spectra		N-type Doping (10^{12} cm^{-2})
	Time (mins)	E' (cm^{-1})	A ₁ ' (cm^{-1})	Strain (%)	
MoS ₂ /Au/PI #1	0	385.1±0.5	404.2±0.2	0.16	9.4
MoS ₂ /Au/PI #2	1	384.6±0.4	403.8±0.2	0.25	10.4
MoS ₂ /Au/PI #3	2	384.2±0.4	403.8±0.2	0.33	9.8
MoS ₂ /Au/PI #4	3	384.0±0.5	404.7±0.1	0.37	5.6
MoS ₂ /Au/PI #5	5	385.2±0.2	405.3±0.2	0.13	4.7
MoS ₂ /Au/PI #6	9	385.2±0.2	404.8±0.2	0.13	5.1
MoS ₂ /Au/PI #7	14	385.9±0.1	405.4±0.1	0	5.0
MoS ₂ /Pd/PI #1	0	384.2±0.3	404.7±0.1	0.32	5.6
MoS ₂ /Pd/PI #2	1	383.8±0.2	404.8±0.1	0.41	5.0
MoS ₂ /Pd/PI #3	1.5	385.2±0.3	405.0±0.1	0.14	5.8
MoS ₂ /Pd/PI #4	2	385.1±0.1	405.0±0.2	0.15	5.7
MoS ₂ /Pd/PI #5	9	385.3±0.3	405.2±0.2	0.11	5.1

Table 7.1: Summary of the parameters extracted from Raman spectra measured on monolayer MoS₂/Au/polyimide and MoS₂/Pd/polyimide with various Ar plasma reaction time. Polyimide (PI).

7.4 Strain Dependent Interfacial Interactions

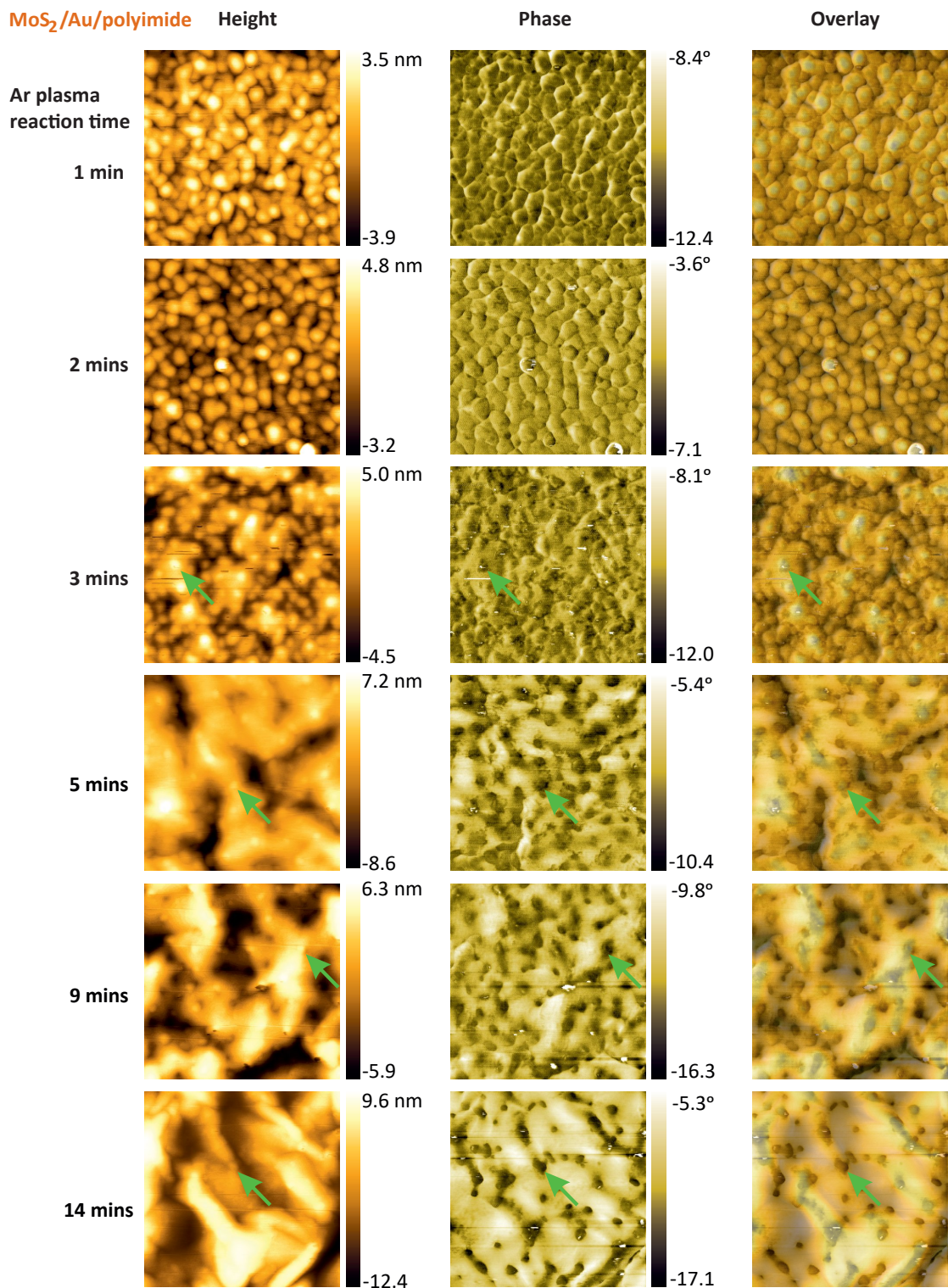


Figure 7.7: Overlay images of AFM topography and phase images of MoS₂/Au/polyimide. The black dot area seen in the phase images matches the supported area in the height images. The image size is $0.5 \times 0.5 \mu\text{m}^2$.

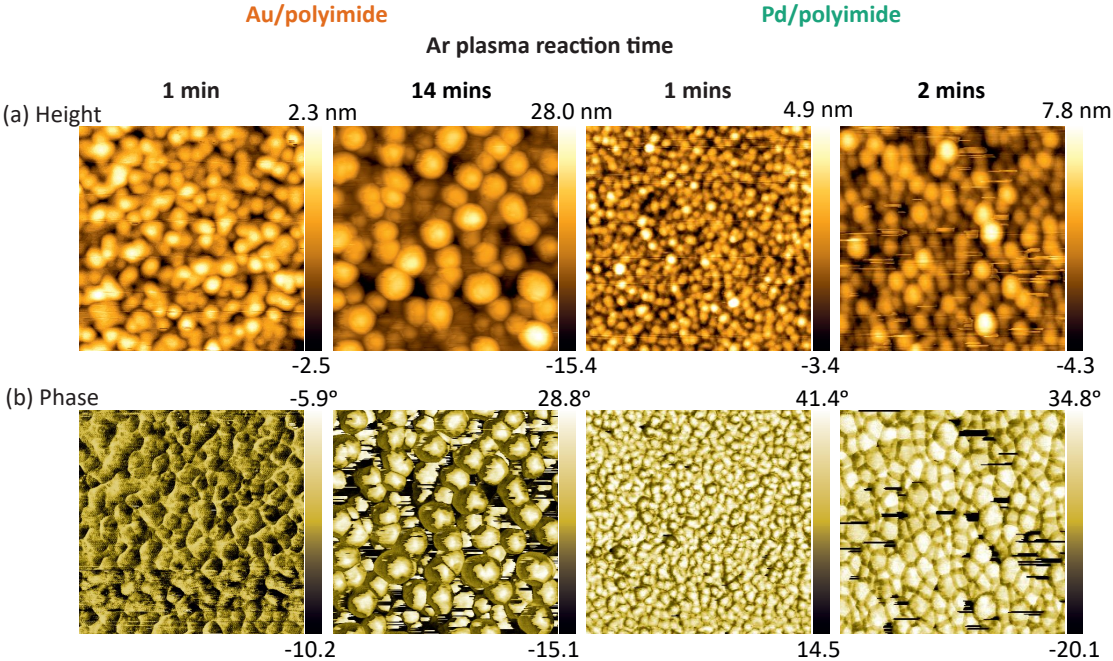


Figure 7.8: Representative AFM (a) topography and (b) phase images of Au/polyimide and Pd/polyimide with increasing Ar plasma reaction times. The image size is 0.5 × 0.5 μm².

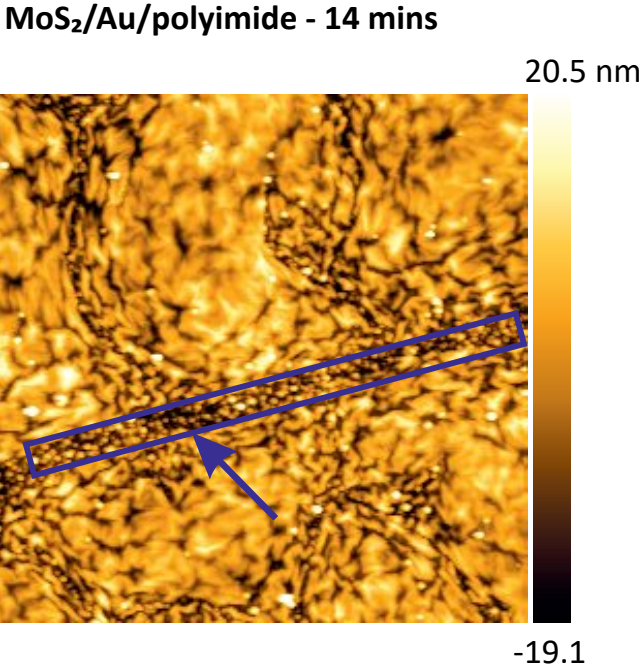


Figure 7.9: Representative AFM topography images of MoS₂/Au/polyimide treated with Ar plasma for 14 mins. The image size is 5 × 5 μm². The visible cracks are marked by purple.

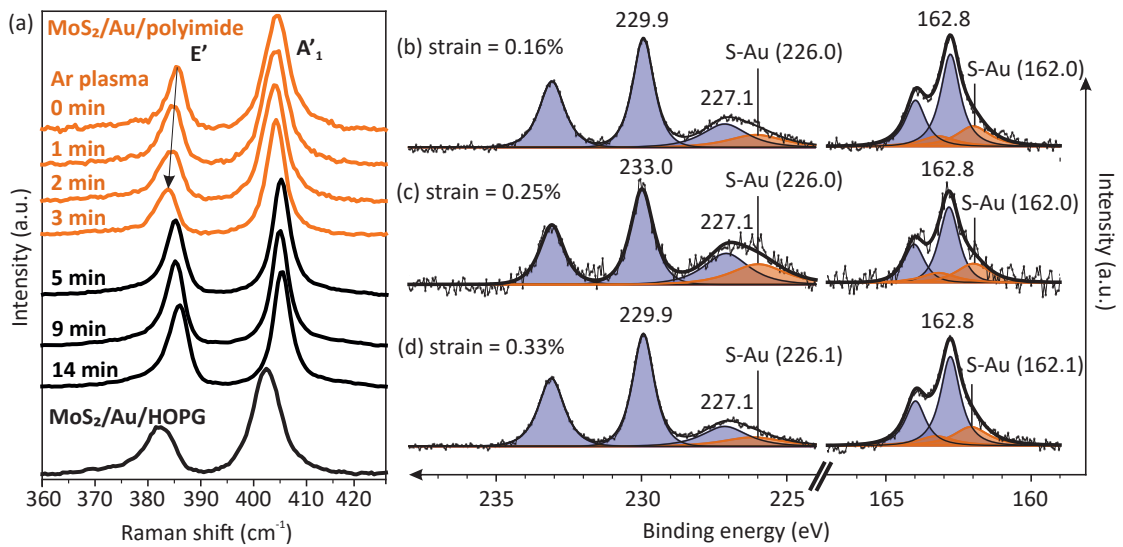


Figure 7.10: Strain dependence of MoS_2/Au interfacial interaction. (a) Normalized representative Raman spectra of monolayer $\text{MoS}_2/\text{Au}/\text{polyimide}$ treated with increasing Ar plasma reaction time. (b-d) Normalized XPS spectra of the Mo 3d, S 2s, and S 2p core levels of monolayer $\text{MoS}_2/\text{Au}/\text{polyimide}$ with increasing strain, which are extracted from their Raman spectra, as shown in Table 7.1. Peaks from intrinsic MoS_2 are marked as purple. S 2s and S 2p peaks for S-Au and are marked as orange.

Raman spectra are summarized in Table 7.1.

For $\text{MoS}_2/\text{Au}/\text{polyimide}$, the strain increases from 0.16% to 0.37% when Ar plasma reaction time increases from 0 min to 3 mins. However, when the Ar plasma reaction time is increased by more than 3 mins, the strain falls to below 0.13%. Interestingly, the doping concentration also reduces from $\sim 1 \times 10^{13} \text{ cm}^{-2}$ to $\sim 6 \times 10^{12} \text{ cm}^{-2}$ when the Ar plasma reaction time reaches 3 mins. This is consistent with AFM results in Fig. 7.4 and 7.5, which indicate the MoS_2 film is partially suspended after 3 mins plasma treatment (Fig. 7.5(c)). This suspended area, separated from Au film, may be the origin of the reduction of doping concentration (Table 7.1). When MoS_2 is transferred to a rougher surface, the monolayer is broken and partially delaminated from the underlying metal surface, resulting in strain relaxation.

XPS is also used to characterize the strain dependence of the metal-S interactions (Fig. 7.10(b)). The XPS measurements were performed on the $\text{MoS}_2/\text{Au}/\text{polyimide}$ with various surface roughness. To minimize the edge effect, the surface roughness below the threshold of delamination is used. The strain is calculated from the individual Raman spectra, as shown in Table 7.1. With increasing strain from 0.16% to 0.33%, the peak separation between S-Au and S-Mo peaks in S 2p spectra reduced from 0.8 eV to 0.7 eV, and S-Au peaks in S 2s spectra also shifted to the lower position by 0.1 eV. Since strain changes the bond distances and angles, it induces charge redistribution around S atoms [240], which appears as a peak shift in XPS data. The results show that the interfacial metal-S interaction is shifted toward the S-Mo peak, which suggests the metal-induced charge localization effect is reduced due to the strain effect.

Chapter 7. Characterization of Strain Engineered Metal Contact on Monolayer MoS₂

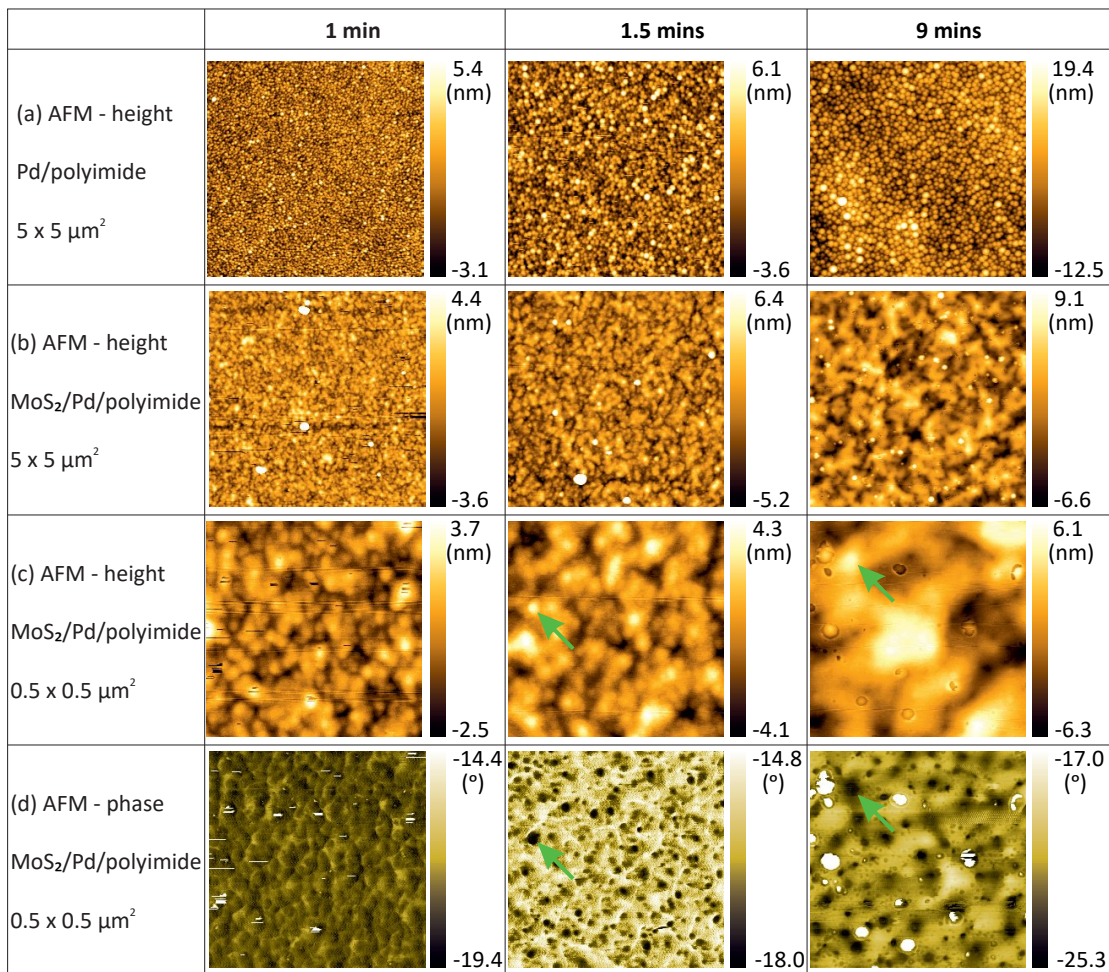


Figure 7.11: Representative AFM topography images of Pd/polyimide (a) before and (b) after transferring the monolayer MoS₂ with increasing Ar plasma reaction time from 1 min, 1.5 mins, to 9 mins. Higher resolution AFM (c) topography and (d) simultaneously measured phase images of MoS₂/Pd/polyimide.

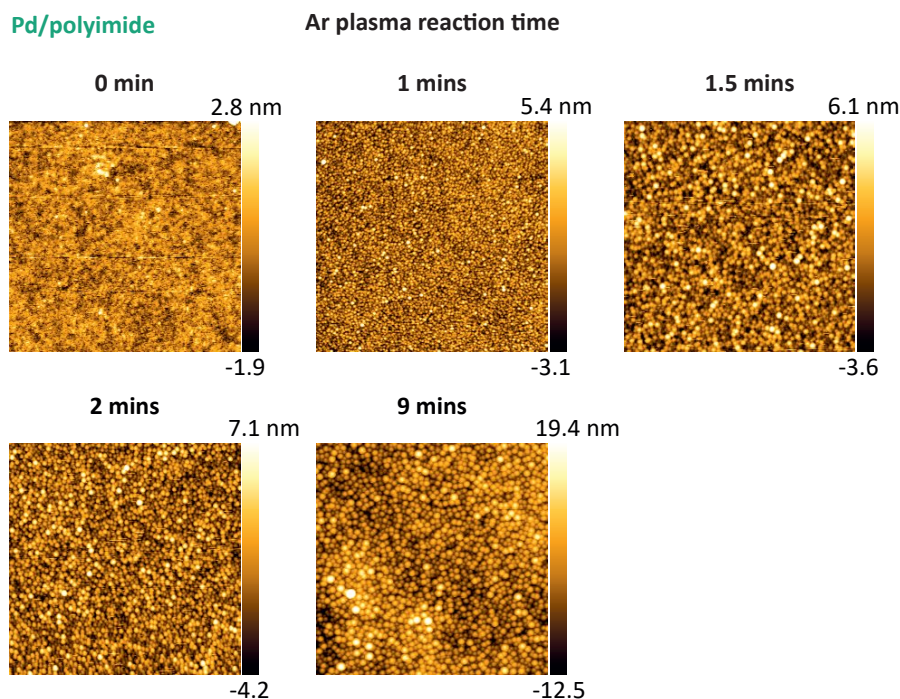


Figure 7.12: Representative AFM topography image of Pd/polyimides with increasing Ar reaction time. The image size is $3 \times 3 \mu\text{m}^2$.

The experiment repeated for $\text{MoS}_2/\text{Pd}/\text{polyimide}$ points to the same conclusion, as shown in Fig. 7.11-7.14. The delamination-induced strain relaxation is also found but with a reduced threshold of Ar plasma reaction time (1 min), while the doping concentration is found to be insensitive to roughness changes. Since the interaction strength between MoS_2 and Pd is stronger [133], the threshold for the delamination would happen earlier than the case of $\text{MoS}_2/\text{Au}/\text{polyimide}$. Similarly, the strain-induced S-Pd peak shifts are also observed in the XPS spectra.

7.5 Conclusions

The interaction at the interfaces between monolayer MoS_2 and various metals, including Au, Pd, and HOPG, is investigated. In contrast to the MoS_2/HOPG interface, interface states were observed at the S-Au and S-Pd interface. The interface states of S-Au are shifted toward lower binding energy than those of S-Pd, due to the weaker covalent bonding. The shift also depends on the strain. As strain increases, the peak shifts are found to be reduced, suggesting that the strain redistributes the charge toward the metal atoms. On the other hand, Raman spectroscopy and atomic force microscopy results indicate that when MoS_2 is transferred onto the Au or Pd substrate, the strain on the MoS_2 increases with increasing metal surface roughness. However, once the metal surface RMS roughness increases over the threshold, the MoS_2 film tends to delaminate and release the strain.

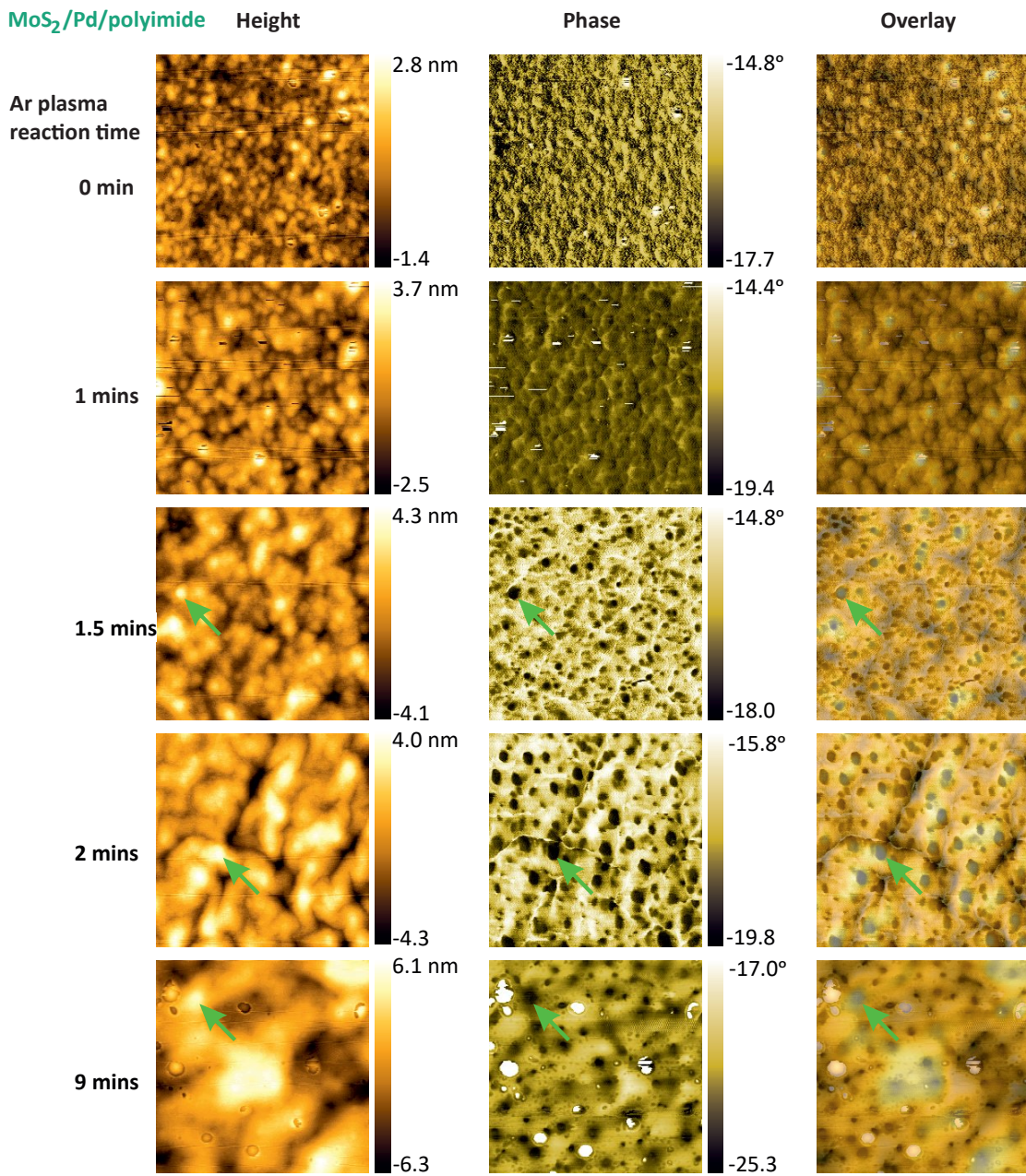


Figure 7.13: Overlay images of AFM topography and phase images of MoS₂/Pd/polyimide. The black dot area seen in the phase images matches the supported area in the height images. The image size is $0.5 \times 0.5 \mu\text{m}^2$.

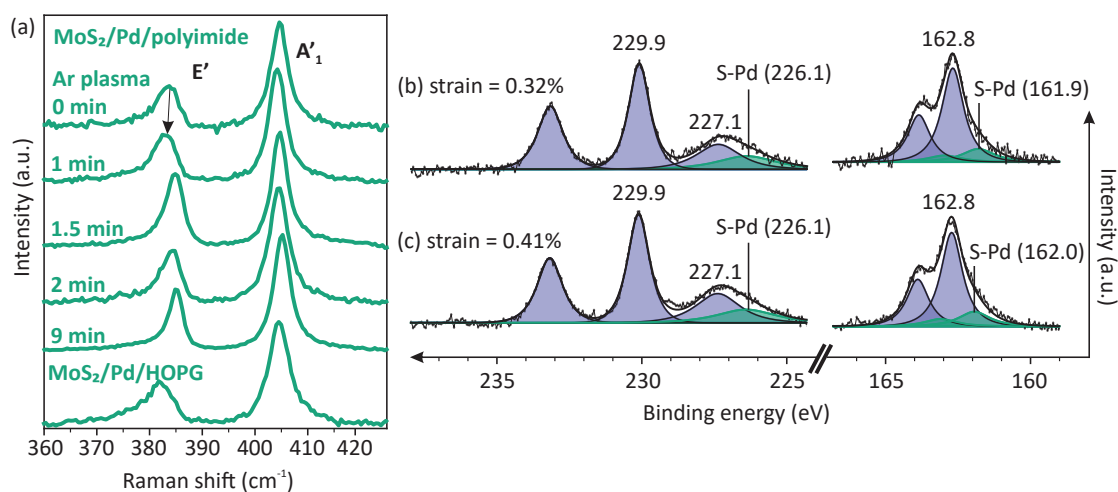


Figure 7.14: Strain dependence of MoS₂/Pd interfacial interaction. (a) Normalized representative Raman spectra of monolayer MoS₂/Pd/polyimides treated with increasing Ar plasma reaction time. (b-c) Normalized XPS spectra of the Mo 3d, S 2s, and S 2p core levels of monolayer MoS₂/Pd/polyimide with increasing strain, which are extracted from their Raman spectra, as shown in Table 7.1. Peaks from intrinsic MoS₂ are marked as purple. S 2s and S 2p peaks for S-Pd and are marked as green.

8 Conclusions

In this study, a strain- and gate-controllable STM sample holder for 2D materials is developed. The holder uses an in situ nanoindentation technique to deform the 2D materials, which are supported by a polyimide film with a thickness of approximately $1\ \mu\text{m}$. The indenter has a travel range of approximately $120\ \mu\text{m}$ and nanometer precision, achieved through a gearbox and a piezoelectric stack. A Pd clamp is used to enhance strain transfer efficiency.

The indentation-induced deflection on the 2D materials/polyimide is tracked by measuring the variation of STM tip height in constant current mode, and the gate controllability is confirmed by measuring the dependence of the tip height on gate voltage. By analyzing the lattice parameters in a series of atomic resolution STM images with increasing indentation depth, the strain response in 2D materials such as graphene and monolayer MoS_2 is examined. In tented structures with high strain, the change in the distribution of reciprocal lattice parameters is sensitive to indentation, allowing the extraction of the magnitude and directions of stretching strain, in addition to the curvature-induced local bending strain.

The indenter is further modified into a ridge-like shape, enabling the measurement of Poisson's ratio of 2D materials at the atomic scale for the first time. In-plane negative Poisson's ratios are reported for both graphene and monolayer MoS_2 , indicating a universal mechanism involving the alternating process of wrinkling and de-wrinkling in supported 2D materials when subjected to increasing uniaxial strain. These observations provide valuable insights for future elastic strain engineering applications in 2D materials.

In addition, the XPS study characterizes the strain dependence of interface interactions by transferring monolayer MoS_2 onto pre-fabricated metal surfaces with controlled roughness. The emergence of additional peaks due to metal-S interaction is observed for both the S-Au and S-Pd interfaces, in contrast to the MoS_2/HOPG interface. The S-Au peaks exhibit higher binding energy compared to those of S-Pd, indicating weaker covalent bonding between Au and MoS_2 than between Pd and MoS_2 . As strain increases, the interface peaks have reduced shifts, implying that the strain redistributes the charge. Additionally, Raman spectroscopy and AFM results indicate that the strain on the MoS_2 increases with increasing Au or Pd roughness. However, delamination of the MoS_2 film is observed when the roughness surpasses a certain threshold, resulting in strain relaxation.

9 Outlook

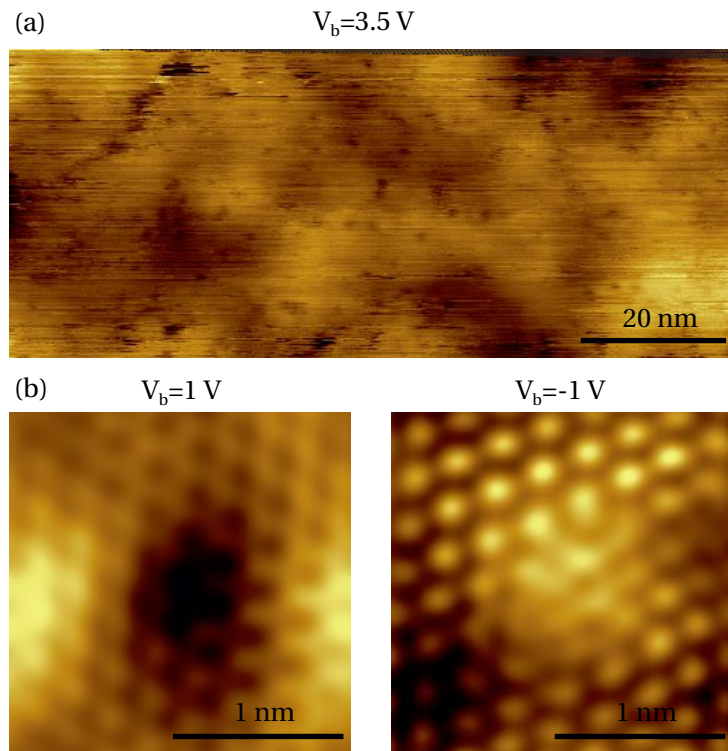


Figure 9.1: STM images of defects in monolayer MoS_2 /polyimide. (a) Large area image. (b) Atomic resolution images of a defect with V_b dependence. For these three images, the tunneling current is set to 100 pA.

After numerous modifications to our sample holder structure and imaging techniques, we successfully attained the stability necessary for capturing atomic resolution STM images. Fig. 9.1 presents these atomic-resolution images, revealing both filled and empty states of the defect structure. The results are consistent with prior STM images of Mo vacancies, which are characterized by depressions and three-lobed protrusions [241]. In contrast, the more common S vacancies appear solely as depressions, irrespective of V_b . Mo vacancies possess

three in-gap states below the Fermi level.

Ongoing STS research into the electronic structure of Mo and S vacancies, along with other disorder types like edge sites, is crucial for applications of MoS₂ in catalysis [242] and quantum computing [243–245]. Theoretical predictions suggest that strain can shift S vacancy-induced gap states toward the Fermi level, thus optimizing catalytic performance [14]. Additionally, gating could potentially manipulate gap states to further enhance performance [246]. However, direct evidence is not reported yet due to technical challenges. Our STS characterization was not completed due to reproducibility issues (see below).

Throughout this thesis, significant efforts were dedicated to enabling local spectroscopy. However, the sample's inherent flexibility caused changes in tip-sample distance during bias sweeping in STS measurements, leading to occasional tunneling current saturation. This issue was more prevalent when STS was performed immediately following STM tip movement, as the flexible 2D material may require time to stabilize after external stimuli are altered. This is similar to observations when adjusting indentation depth (see Fig. 5.4 in chapter 5). This instability underscores the importance of maintaining a low scanning speed, as previously reported in STM measurements on suspended graphene [166].

Furthermore, after the initial STS measurement, current saturation often recurred in subsequent measurements due to an abrupt V_b jump associated with a software issue in Nanonis. As V_b changes can impact STM tip height, this indicates that during STS measurements with the feedback loop off, the tip-sample distance continuously changes while sweeping V_b . This contrasts with conventional STS measurements on rigid substrates. To understand the phenomena occurring during STS measurements and to extract pristine LDOS from 2D materials while excluding the effect of tip-sample distance variations, developing theoretical models or simulations may be necessary.

Experimentally, tip-sample distance fluctuations could be reduced by measuring the sample in a tented structure with high strain, as the overall structure exhibits greater rigidity and demands higher tension for stability [166, 247]. Although attempts were made to measure the sample under tented conditions, consistently achieving this configuration proved challenging due to significant deformation of the polyimide. Indications of potentially damaged polyimide in tented conditions were observed through increased leakage current in the gate structure. Moreover, to understand strain effects, it is also necessary to measure the spectroscopy of relaxed 2D materials and compare it to strained structures.

Alternatively, the tip's perturbation on the sample can be minimized by conducting STS measurements at a lower tunneling current set point, resulting in a larger tip-sample distance. Despite reducing the electric field between the tip and sample [248, 249], no clear improvement was observed using a lower set point for tunneling current, and STS saturation continued to occur occasionally.

While conducting STS measurements poses challenges as previously described, successful

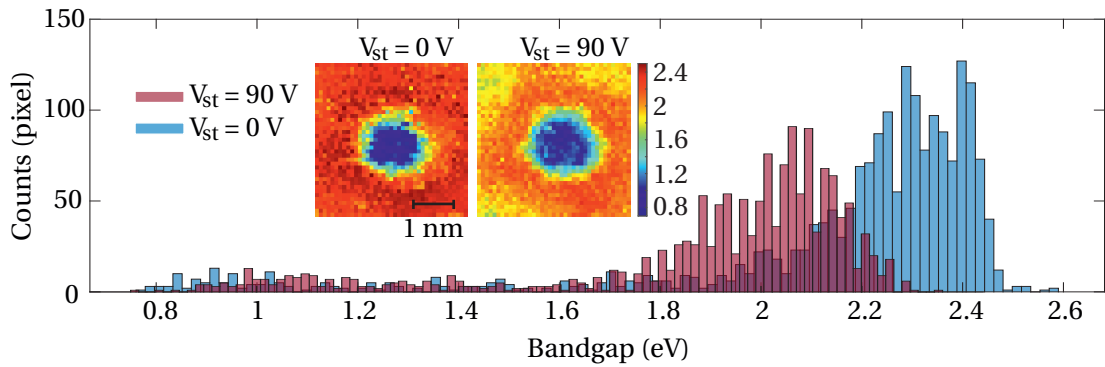


Figure 9.2: Bandgap histograms and distributions (inset) of a Mo vacancy with increasing V_{st} from 0 to 90 V. The bandgap is calculated by fitting the conduction and valance bands in each local tunneling spectrum.

LDOS mapping of a Mo vacancy was achieved by measuring the sample in the high-strain tented condition. Fig. 9.2 illustrates the histograms and distributions (shown in the inset) of the bandgap for a Mo vacancy as V_{st} increases from 0 to 90 V. The bandgaps are determined through fitting the conduction and valance bands in each local tunneling spectrum [1]. Notably, the histograms reveal that the population of bandgaps outside the defect area centers around 2.35 eV when V_{st} is 0, but shifts to approximately 2.05 eV as V_{st} increases to 90 V. This degree of bandgap shift suggests that a strain of 1-2% is applied, consistent with previously reported strain effects on bandgap reduction [1, 41]. Intriguingly, the bandgap within the defect area exhibits a reverse shift, moving from approximately 0.9 eV to 1.1 eV as V_{st} increases from 0 to 90 V. Further detailed analysis of each STS spectrum will be undertaken, offering invaluable insights into the influence of strain on the electronic structure of defects.

In summary, although atomic resolution STM images were obtained, STS characterization faced technical challenges primarily due to sample flexibility. Future work should concentrate on improving measurement techniques, creating theoretical models, and comparing strained and relaxed 2D materials. This will ultimately lead to a better understanding of strain responses in 2D materials and enhance their controllability for various applications.

Bibliography

- [1] B. G. Shin, G. H. Han, S. J. Yun, H. M. Oh, J. J. Bae, Y. J. Song, C. Y. Park, and Y. H. Lee. Indirect bandgap puddles in monolayer mos₂ by substrate-induced local strain. *Advanced Materials*, 28(42):9378–9384, 2016. doi: 10.1002/adma.201602626.
- [2] Z. H. Dai, L. Q. Liu, and Z. Zhang. Strain engineering of 2d materials: Issues and opportunities at the interface. *Advanced Materials*, 31(45):1805417, 2019. doi: 10.1002/adma.201805417.
- [3] S. X. Yang, Y. J. Chen, and C. B. Jiang. Strain engineering of two-dimensional materials: Methods, properties, and applications. *Infomat*, 3(4):397–420, 2021. doi: 10.1002/inf2.12177.
- [4] J. C. Meyer, A. K. Geim, M. I. Katsnelson, K. S. Novoselov, T. J. Booth, and S. Roth. The structure of suspended graphene sheets. *Nature*, 446(7131):60–63, 2007. doi: 10.1038/nature05545.
- [5] D. Akinwande, N. Petrone, and J. Hone. Two-dimensional flexible nanoelectronics. *Nature Communications*, 5(1):5678, 2014. doi: 10.1038/ncomms6678.
- [6] S. Bertolazzi, J. Brivio, and A. Kis. Stretching and breaking of ultrathin mos₂. *ACS Nano*, 5(12):9703–9709, 2011. doi: 10.1021/nn203879f.
- [7] J. O. Island, A. Kuc, E. H. Diependaal, R. Bratschitsch, H. S. J. van der Zant, T. Heine, and A. Castellanos-Gomez. Precise and reversible band gap tuning in single-layer mose₂ by uniaxial strain. *Nanoscale*, 8(5):2589–2593, 2016. doi: 10.1039/c5nr08219f.
- [8] T. Cheiwchanchamnangij, W. R. L. Lambrecht, Y. Song, and H. Dery. Strain effects on the spin-orbit-induced band structure splittings in monolayer mos₂ and graphene. *Physical Review B*, 88(15):155404, 2013. doi: 10.1103/PhysRevB.88.155404.
- [9] G. Zhang and Y. W. Zhang. Strain effects on thermoelectric properties of two-dimensional materials. *Mechanics of Materials*, 91:382–398, 2015. doi: 10.1016/j.mechmat.2015.03.009.
- [10] L. Y. Zhu, T. T. Zhang, Z. M. Sun, J. H. Li, G. B. Chen, and S. Y. A. Yang. Thermal conductivity of biaxial-strained mos₂: sensitive strain dependence and size-dependent reduction rate. *Nanotechnology*, 26(46):465707, 2015. doi: 10.1088/0957-4484/26/46/465707.
- [11] L. Dong, R. R. Namburu, T. P. O’Regan, M. Dubey, and A. M. Dongare. Theoretical study on strain-induced variations in electronic properties of monolayer mos₂. *Journal of Materials Science*, 49(19):6762–6771, 2014. doi: 10.1007/s10853-014-8370-5.

Bibliography

- [12] K. A. N. Duerloo, Y. Li, and E. J. Reed. Structural phase transitions in two-dimensional mo- and w-dichalcogenide monolayers. *Nature Communications*, 5(1):4214, 2014. doi: 10.1038/ncomms5214.
- [13] Y. Wang, J. Xiao, H. Y. Zhu, Y. Li, Y. Alsaïd, K. Y. Fong, Y. Zhou, S. Q. Wang, W. Shi, Y. Wang, A. Zettl, E. J. Reed, and X. Zhang. Structural phase transition in monolayer mote2 driven by electrostatic doping. *Nature*, 550(7677):487–491, 2017. doi: 10.1038/nature24043.
- [14] H. Li, C. Tsai, A. L. Koh, L. L. Cai, A. W. Contryman, A. H. Fragapane, J. H. Zhao, H. S. Han, H. C. Manoharan, F. Abild-Pedersen, J. K. Nørskov, and X. L. Zheng. Activating and optimizing mos2 basal planes for hydrogen evolution through the formation of strained sulphur vacancies. *Nature Materials*, 15(1):48–53, 2016. doi: 10.1038/Nmat4465.
- [15] D. Voiry, J. Yang, and M. Chhowalla. Recent strategies for improving the catalytic activity of 2d tmd nanosheets toward the hydrogen evolution reaction. *Advanced Materials*, 28(29):6197–6206, 2016. doi: 10.1002/adma.201505597.
- [16] B. Radisavljevic, A. Radenovic, J. Brivio, V. Giacometti, and A. Kis. Single-layer mos2 transistors. *Nature Nanotechnology*, 6(3):147–150, 2011. doi: 10.1038/Nnano.2010.279.
- [17] X. F. Qian, J. W. Liu, L. Fu, and J. Li. Quantum spin hall effect in two-dimensional transition metal dichalcogenides. *Science*, 346(6215):1344–1347, 2014. doi: 10.1126/science.1256815.
- [18] Y. D. Ma, L. Z. Kou, X. Li, Y. Dai, and T. Heine. Two-dimensional transition metal dichalcogenides with a hexagonal lattice: Room-temperature quantum spin hall insulators. *Physical Review B*, 93(3):035442, 2016. doi: 10.1103/PhysRevB.93.035442.
- [19] Y. D. Ma, L. Z. Kou, X. Li, Y. Dai, S. C. Smith, and T. Heine. Quantum spin hall effect and topological phase transition in two-dimensional square transition-metal dichalcogenides. *Physical Review B*, 92(8):085427, 2015. doi: 10.1103/PhysRevB.92.085427.
- [20] K. F. Mak, C. Lee, J. Hone, J. Shan, and T. F. Heinz. Atomically thin mos2: A new direct-gap semiconductor. *Physical Review Letters*, 105(13):136805, 2010. doi: 10.1103/PhysRevLett.105.136805.
- [21] J. Q. Zhu, Z. C. Wang, H. J. Dai, Q. Q. Wang, R. Yang, H. Yu, M. Z. Liao, J. Zhang, W. Chen, Z. Wei, N. Li, L. J. Du, D. X. Shi, W. L. Wang, L. X. Zhang, Y. Jiang, and G. Y. Zhang. Boundary activated hydrogen evolution reaction on monolayer mos2. *Nature Communications*, 10(1):1348, 2019. doi: 10.1038/s41467-019-09269-9.
- [22] N. Li, Q. Q. Wang, C. Shen, Z. Wei, H. Yu, J. Zhao, X. B. Lu, G. L. Wang, C. L. He, L. Xie, J. Q. Zhu, L. J. Du, R. Yang, D. X. Shi, and G. Y. Zhang. Large-scale flexible and transparent electronics based on monolayer molybdenum disulfide field-effect transistors. *Nature Electronics*, 3(11):711–717, 2020. doi: 10.1038/s41928-020-00475-8.
- [23] E. Singh, P. Singh, K. S. Kim, G. Y. Yeom, and H. S. Nalwa. Flexible molybdenum disulfide (mos2) atomic layers for wearable electronics and optoelectronics. *ACS Applied Materials & Interfaces*, 11(12):11061–11105, 2019. doi: 10.1021/acsami.8b19859.
- [24] G. Yoo, S. L. Choi, S. J. Park, K. T. Lee, S. Lee, M. S. Oh, J. Heo, and H. J. Park. Flexible and wavelength-selective mos2 phototransistors with monolithically integrated transmission color filters. *Scientific Reports*, 7(1):40945, 2017. doi: 10.1038/srep40945.

- [25] J. Kim, Y. Lee, M. Kang, L. Hu, S. Zhao, and J. H. Ahn. 2d materials for skin-mountable electronic devices. *Advanced Materials*, 33(47):2005858, 2021. doi: 10.1002/adma.202005858.
- [26] T. T. Yang, X. Jiang, Y. H. Huang, Q. Tian, L. Zhang, Z. H. Dai, and H. W. Zhu. Mechanical sensors based on two-dimensional materials: Sensing mechanisms, structural designs and wearable applications. *Science*, 25(1):103728, 2022. doi: 10.1016/j.isci.2021.103728.
- [27] L. David, R. Bhandavat, and G. Singh. Mos₂/graphene composite paper for sodium-ion battery electrodes. *ACS Nano*, 8(2):1759–1770, 2014. doi: 10.1021/nn406156b.
- [28] Z. Hu, L. X. Wang, K. Zhang, J. B. Wang, F. Y. Cheng, Z. L. Tao, and J. Chen. Mos₂ nanoflowers with expanded interlayers as high-performance anodes for sodium-ion batteries. *Angewandte Chemie-International Edition*, 53(47):12794–12798, 2014. doi: 10.1002/anie.201407898.
- [29] E. Pomerantseva and Y. Gogotsi. Two-dimensional heterostructures for energy storage. *Nature Energy*, 2(7):1–6, 2017. doi: 10.1038/nenergy.2017.89.
- [30] R. Sahoo, A. Pal, and T. Pal. 2d materials for renewable energy storage devices: Outlook and challenges. *Chemical Communications*, 52(93):13528–13542, 2016. doi: 10.1039/c6cc05357b.
- [31] X. Y. Zhang, L. L. Hou, A. Ciesielski, and P. Samori. 2d materials beyond graphene for high-performance energy storage applications. *Advanced Energy Materials*, 6(23):1600671, 2016. doi: 10.1002/aenm.201600671.
- [32] D. H. Deng, K. S. Novoselov, Q. Fu, N. F. Zheng, Z. Q. Tian, and X. H. Bao. Catalysis with two-dimensional materials and their heterostructures. *Nature Nanotechnology*, 11(3):218–230, 2016. doi: 10.1038/Nnano.2015.340.
- [33] Y. G. Li, H. L. Wang, L. M. Xie, Y. Y. Liang, G. S. Hong, and H. J. Dai. Mos₂ nanoparticles grown on graphene: An advanced catalyst for the hydrogen evolution reaction. *Journal of the American Chemical Society*, 133(19):7296–7299, 2011. doi: 10.1021/ja201269b.
- [34] M. A. Lukowski, A. S. Daniel, F. Meng, A. Forticaux, L. S. Li, and S. Jin. Enhanced hydrogen evolution catalysis from chemically exfoliated metallic mos₂ nanosheets. *Journal of the American Chemical Society*, 135(28):10274–10277, 2013. doi: 10.1021/ja404523s.
- [35] Y. Zhu, L. L. Peng, Z. W. Fang, C. S. Yan, X. Zhang, and G. H. Yu. Structural engineering of 2d nanomaterials for energy storage and catalysis. *Advanced Materials*, 30(15):1706347, 2018. doi: 10.1002/adma.201706347.
- [36] X. Cong, X. L. Liu, M. L. Lin, and P. H. Tan. Application of raman spectroscopy to probe fundamental properties of two-dimensional materials. *npj 2D Materials and Applications*, 4(1):13, 2020. doi: 10.1038/s41699-020-0140-4.
- [37] H. J. Conley, B. Wang, J. I. Ziegler, R. F. Haglund, S. T. Pantelides, and K. I. Bolotin. Bandgap engineering of strained monolayer and bilayer mos₂. *Nano Letters*, 13(8):3626–3630, 2013. doi: 10.1021/nl4014748.
- [38] Z. H. Ni, T. Yu, Y. H. Lu, Y. Y. Wang, Y. P. Feng, and Z. X. Shen. Uniaxial strain on graphene: Raman spectroscopy study and band-gap opening. *ACS Nano*, 2(11):2301–5, 2008. doi: 10.1021/nn800459e.

Bibliography

- [39] H. Li, A. W. Contryman, X. F. Qian, S. M. Ardakani, Y. J. Gong, X. L. Wang, J. M. Weisse, C. H. Lee, J. H. Zhao, P. M. Ajayan, J. Li, H. C. Manoharan, and X. L. Zheng. Optoelectronic crystal of artificial atoms in strain-textured molybdenum disulphide. *Nature Communications*, 6:7381, 2015. doi: 10.1038/ncomms8381.
- [40] A. Reserbat-Plantey, D. Kalita, Z. Han, L. Ferlazzo, S. Autier-Laurent, K. Komatsu, C. Li, R. Weil, A. Ralko, L. Marty, S. Gueron, N. Bendiab, H. Bouchiat, and V. Bouchiat. Strain superlattices and macroscale suspension of graphene induced by corrugated substrates. *Nano Letters*, 14(9):5044–5051, 2014. doi: 10.1021/nl5016552.
- [41] D. J. Trainer, Y. Zhang, F. Bobba, X. X. Xi, S. W. Hla, and M. Iavarone. The effects of atomic-scale strain relaxation on the electronic properties of monolayer mos2. *ACS Nano*, 13(7):8284–8291, 2019. doi: 10.1021/acsnano.9b03652.
- [42] Y. Y. Hui, X. F. Liu, W. J. Jie, N. Y. Chan, J. H. Hao, Y. T. Hsu, L. J. Li, W. L. Guo, and S. P. Lau. Exceptional tunability of band energy in a compressively strained trilayer mos2 sheet. *ACS Nano*, 7(8):7126–7131, 2013. doi: 10.1021/nn4024834.
- [43] D. Edelberg, H. Kumar, V. Shenoy, H. Ochoa, and A. N. Pasupathy. Tunable strain soliton networks confine electrons in van der waals materials. *Nature Physics*, 16(11):1097–1102, 2020. doi: 10.1038/s41567-020-0953-2.
- [44] F. R. Eder, J. Kotakoski, K. Holzweber, C. Mangler, V. Skakalova, and J. C. Meyer. Probing from both sides: Reshaping the graphene landscape via face-to-face dual-probe microscopy. *Nano Letters*, 13(5):1934–1940, 2013. doi: 10.1021/nl3042799.
- [45] Kenan Elibol, Stefan Hummel, Bernhard C. Bayer, and Jannik C. Meyer. New imaging modes for analyzing suspended ultra-thin membranes by double-tip scanning probe microscopy. *Scientific Reports*, 10(1):4839, 2020. doi: 10.1038/s41598-020-60731-x.
- [46] J. Li, Z. W. Shan, and E. Ma. Elastic strain engineering for unprecedented materials properties. *MRS Bulletin*, 39(2):108–117, 2014. doi: 10.1557/mrs.2014.3.
- [47] S. W. Bedell, A. Khakifirooz, and D. K. Sadana. Strain scaling for cmos. *MRS Bulletin*, 39(2):131–137, 2014. doi: 10.1557/mrs.2014.5.
- [48] H. H. Radamson, H. Zhu, Z. Wu, X. He, H. Lin, J. Liu, J. Xiang, Z. Kong, W. Xiong, J. Li, H. Cui, J. Gao, H. Yang, Y. Du, B. Xu, B. Li, X. Zhao, J. Yu, Y. Dong, and G. Wang. State of the art and future perspectives in advanced cmos technology. *Nanomaterials*, 10(8):1555, 2020. doi: 10.3390/nano10081555.
- [49] Min Chu, Yongke Sun, Umamaheswari Aghoram, and Scott E. Thompson. Strain: A solution for higher carrier mobility in nanoscale mosfets. *Annual Review of Materials Research*, 39(1):203–229, 2009. doi: 10.1146/annurev-matsci-082908-145312.
- [50] Meikei Jeong, Bruce Doris, Jakub Kedzierski, Ken Rim, and Min Yang. Silicon device scaling to the sub-10-nm regime. *Science*, 306(5704):2057–2060, 2004. doi: 10.1126/science.1100731.
- [51] J. L. Hoyt, H. M. Nayfeh, S. Eguchi, I. Aberg, G. Xia, T. Drake, E. A. Fitzgerald, and D. A. Antoniadis. Strained silicon mosfet technology. *International Electron Devices Meeting, Technical Digest*, pages 23–26, 2002. doi: 10.1109/IEDM.2002.1175770.
- [52] C. S. Smith. Piezoresistance effect in germanium and silicon. *Physical Review*, 94(1):42–49, 1954. doi: 10.1103/PhysRev.94.42.

- [53] Scott Thompson, N Anand, M Armstrong, C Auth, B Arcot, M Alavi, P Bai, J Bielefeld, R Bigwood, and J Brandenburg. A 90 nm logic technology featuring 50 nm strained silicon channel transistors, 7 layers of cu interconnects, low k ild, and 1/spl mu/m/sup 2/sram cell. In *Digest. International Electron Devices Meeting*, pages 61–64. IEEE, 2002. ISBN 0780374622. doi: 10.1109/IEDM.2002.1175779.
- [54] F. Ding, R. Singh, J. D. Plumhof, T. Zander, V. Křápek, Y. H. Chen, M. Benyoucef, V. Zwiller, K. Dörr, G. Bester, A. Rastelli, and O. G. Schmidt. Tuning the exciton binding energies in single self-assembled ingaas/gaas quantum dots by piezoelectric-induced biaxial stress. *Physical Review Letters*, 104(6):067405, 2010. doi: 10.1103/physrevlett.104.067405.
- [55] Giorgio Signorello, Siegfried Karg, Mikael T. Björk, Bernd Gotsmann, and Heike Riel. Tuning the light emission from gaas nanowires over 290 mev with uniaxial strain. *Nano Letters*, 13(3):917–924, 2013. doi: 10.1021/nl303694c.
- [56] G. Tsutsui, S. Mochizuki, N. Loubet, S. W. Bedell, and D. K. Sadana. Strain engineering in functional materials. *AIP Advances*, 9(3):030701, 2019. doi: 10.1063/1.5075637.
- [57] S. Ito, H. Namba, K. Yamaguchi, T. Hirata, K. Ando, S. Koyama, S. Kuroki, N. Ikezawa, T. Suzuki, T. Saitoh, and T. Horiuchi. Mechanical stress effect of etch-stop nitride and its impact on deep submicron transistor design. *International Electron Devices Meeting, Technical Digest*, pages 247–250, 2000. doi: 10.1109/Iedm.2000.904303.
- [58] J. Welser, J. L. Hoyt, and J. F. Gibbons. Electron-mobility enhancement in strained-si n-type metal-oxide-semiconductor field-effect transistors. *IEEE Electron Device Letters*, 15(3):100–102, 1994. doi: 10.1109/55.285389.
- [59] S. Gannavaram, N. Pesovic, and M. C. Ozturk. Low temperature (≤ 800 degrees c) recessed junction selective silicon-germanium source/drain technology for sub-70 nm cmos. *International Electron Devices Meeting, Technical Digest*, pages 437–440, 2000. doi: 10.1109/Iedm.2000.904350.
- [60] K. Y. Lim, H. Lee, C. Ryu, K. I. Seo, U. Kwon, S. Kim, J. Choi, K. Oh, H. K. Jeon, C. Song, T. O. Kwon, J. Cho, S. Lee, Y. Sohn, H. S. Yoon, J. Park, K. Lee, W. Kim, E. Lee, S. P. Sim, C. G. Koh, S. B. Kang, S. Choi, and C. Chung. Novel stress-memorization-technology (smt) for high electron mobility enhancement of gate last high-k/metal gate devices. *International Electron Devices Meeting, Technical Digest*, 2010. doi: 10.1109/IEDM.2010.5703332.
- [61] K. Rim, J. Welser, J. L. Hoyt, and J. F. Gibbons. Enhanced hole mobilities in surface-channel strained-si p-mosfets. *International Electron Devices Meeting, Technical Digest*, pages 517–520, 1995. doi: 10.1109/IEDM.1995.499251.
- [62] P. Packan, S. Akbar, M. Armstrong, D. Bergstrom, M. Brazier, H. Deshpande, K. Dev, G. Ding, T. Ghani, O. Golonzka, W. Han, J. He, R. Heussner, R. James, J. Jopling, C. Kenyon, S. H. Lee, M. Liu, S. Lodha, B. Mattis, A. Murthy, L. Neiberg, J. Neiryneck, S. Pae, C. Parker, L. Pipes, J. Sebastian, J. Seiple, B. Sell, A. Sharma, S. Sivakumar, B. Song, A. St Amour, K. Tone, T. Troeger, C. Weber, K. Zhang, Y. Luo, and S. Natarajan. High performance 32nm logic technology featuring 2(nd) generation high-k plus metal gate transistors. *International Electron Devices Meeting*, pages 1–4, 2009. doi: 10.1109/IEDM.2009.5424253.

Bibliography

- [63] S. Kim, S. Lee, Y. Oshima, Y. Kondo, E. Okunishi, N. Endo, J. Jung, G. Byun, S. Lee, and K. Lee. Scanning moire fringe imaging for quantitative strain mapping in semiconductor devices. *Applied Physics Letters*, 102(16):161604, 2013. doi: 10.1063/1.4803087.
- [64] Y. Han, L. B. Gao, J. Z. Zhou, Y. Hou, Y. W. Jia, K. Cao, K. Duan, and Y. Lu. Deep elastic strain engineering of 2d materials and their twisted bilayers. *ACS Applied Materials & Interfaces*, 14(7):8655–8663, 2022. doi: 10.1021/acsami.1c23431.
- [65] N. Levy, S. A. Burke, K. L. Meaker, M. Panlasigui, A. Zettl, F. Guinea, A. H. C. Neto, and M. F. Crommie. Strain-induced pseudo-magnetic fields greater than 300 tesla in graphene nanobubbles. *Science*, 329(5991):544–547, 2010. doi: 10.1126/science.1191700.
- [66] M. Y. Li, Y. M. Shi, C. C. Cheng, L. S. Lu, Y. C. Lin, H. L. Tang, M. L. Tsai, C. W. Chu, K. H. Wei, J. H. He, W. H. Chang, K. Suenaga, and L. J. Li. Epitaxial growth of a monolayer wse₂-mos₂ lateral p-n junction with an atomically sharp interface. *Science*, 349(6247):524–528, 2015. doi: 10.1126/science.aab4097.
- [67] C. D. Zhang, M. Y. Li, J. Tersoff, Y. M. Han, Y. S. Su, L. J. Li, D. A. Muller, and C. K. Shih. Strain distributions and their influence on electronic structures of wse₂-mos₂ laterally strained heterojunctions. *Nature Nanotechnology*, 13(2):152–158, 2018. doi: 10.1038/s41565-017-0022-x.
- [68] E. Khestanova, F. Guinea, L. Fumagalli, A. K. Geim, and I. V. Grigorieva. Universal shape and pressure inside bubbles appearing in van der waals heterostructures. *Nature Communications*, 7:12587, 2016. doi: 10.1038/ncomms12587.
- [69] D. Lloyd, X. H. Liu, J. W. Christopher, L. Cantley, A. Wadehra, B. L. Kim, B. B. Goldberg, A. K. Swan, and J. S. Bunch. Band gap engineering with ultralarge biaxial strains in suspended monolayer mos₂. *Nano Letters*, 16(9):5836–5841, 2016. doi: 10.1021/acs.nanolett.6b02615.
- [70] R. Yang, J. Lee, S. Ghosh, H. Tang, R. M. Sankaran, C. A. Zorman, and P. X. L. Feng. Tuning optical signatures of single- and few-layer mos₂ by blown-bubble bulge straining up to fracture. *Nano Letters*, 17(8):4568–4575, 2017. doi: 10.1021/acs.nanolett.7b00730.
- [71] Wenjun Chen, Xuchun Gui, Leilei Yang, Hai Zhu, and Zikang Tang. Wrinkling of two-dimensional materials: methods, properties and applications. *Nanoscale Horizons*, 4(2):291–320, 2019. doi: 10.1039/c8nh00112j.
- [72] A. Castellanos-Gomez, R. Roldan, E. Cappelluti, M. Buscema, F. Guinea, H. S. J. van der Zant, and G. A. Steele. Local strain engineering in atomically thin mos₂. *Nano Letters*, 13(11):5361–5366, 2013. doi: 10.1021/nl402875m.
- [73] Fangyuan Zheng, Quoc Huy Thi, Lok Wing Wong, Qingming Deng, Thuc Hue Ly, and Jiong Zhao. Critical stable length in wrinkles of two-dimensional materials. *ACS Nano*, 14(2):2137–2144, 2020. doi: 10.1021/acsnano.9b08928.
- [74] G. Plechinger, A. Castellanos-Gomez, M. Buscema, H. S. J. van der Zant, G. A. Steele, A. Kuc, T. Heine, C. Schuller, and T. Korn. Control of biaxial strain in single-layer molybdenite using local thermal expansion of the substrate. *2D Materials*, 2(1):015006, 2015. doi: 10.1088/2053-1583/2/1/015006.
- [75] T. M. G. Mohiuddin, A. Lombardo, R. R. Nair, A. Bonetti, G. Savini, R. Jalil, N. Bonini, D. M. Basko, C. Galiotis, N. Marzari, K. S. Novoselov, A. K. Geim, and A. C. Ferrari. Uniaxial

- strain in graphene by raman spectroscopy: G peak splitting, gruneisen parameters, and sample orientation. *Physical Review B*, 79(20):205433, 2009. doi: 10.1103/PhysRevB.79.205433.
- [76] M. A. Bissett, W. Izumida, R. Saito, and H. Ago. Effect of domain boundaries on the raman spectra of mechanically strained graphene. *ACS Nano*, 6(11):10229–10238, 2012. doi: 10.1021/nn304032f.
- [77] J. W. Christopher, M. Vutukuru, D. Lloyd, J. S. Bunch, B. B. Goldberg, D. J. Bishop, and A. K. Swan. Monolayer mos₂ strained to 1.3% with a microelectromechanical system. *Journal of Microelectromechanical Systems*, 28(2):254–263, 2019. doi: 10.1109/Jmems.2018.2877983.
- [78] M. Y. Huang, H. G. Yan, C. Y. Chen, D. H. Song, T. F. Heinz, and J. Hone. Phonon softening and crystallographic orientation of strained graphene studied by raman spectroscopy. *Proceedings of the National Academy of Sciences*, 106(18):7304–7308, 2009. doi: 10.1073/pnas.0811754106.
- [79] Z. Li, Y. Lv, L. Ren, J. Li, L. Kong, Y. Zeng, Q. Tao, R. Wu, H. Ma, B. Zhao, D. Wang, W. Dang, K. Chen, L. Liao, X. Duan, X. Duan, and Y. Liu. Efficient strain modulation of 2d materials via polymer encapsulation. *Nature Communications*, 11(1):1151, 2020. doi: 10.1038/s41467-020-15023-3.
- [80] G. Tsoukleri, J. Parthenios, K. Papagelis, R. Jalil, A. C. Ferrari, A. K. Geim, K. S. Novoselov, and C. Galiotis. Subjecting a graphene monolayer to tension and compression. *Small*, 5(21):2397–2402, 2009. doi: 10.1002/smll.200900802.
- [81] T. Yu, Z. H. Ni, C. L. Du, Y. M. You, Y. Y. Wang, and Z. X. Shen. Raman mapping investigation of graphene on transparent flexible substrate: The strain effect. *Journal of Physical Chemistry C*, 112(33):12602–12605, 2008. doi: 10.1021/jp806045u.
- [82] Riccardo Frisenda, Matthias Drüppel, Robert Schmidt, Steffen Michaelis De Vasconcellos, David Perez De Lara, Rudolf Bratschitsch, Michael Rohlfing, and Andres Castellanos-Gomez. Biaxial strain tuning of the optical properties of single-layer transition metal dichalcogenides. *npj 2D Materials and Applications*, 1(1):10, 2017. doi: 10.1038/s41699-017-0013-7.
- [83] Lei Gong, Ian A. Kinloch, Robert J. Young, Ibtsam Riaz, Rashid Jalil, and Konstantin S. Novoselov. Interfacial stress transfer in a graphene monolayer nanocomposite. *Advanced Materials*, 22(24):2694–2697, 2010. doi: 10.1002/adma.200904264.
- [84] J. J. Yang, J. Colen, J. Liu, M. C. Nguyen, G. W. Chern, and D. Louca. Elastic and electronic tuning of magnetoresistance in mote₂. *Science Advances*, 3(12):eaao4949, 2017. doi: 10.1126/sciadv.aao4949.
- [85] C. Martella, C. Mennucci, E. Cinquanta, A. Lamperti, E. Cappelluti, F. B. de Mongeot, and A. Molle. Anisotropic mos₂ nanosheets grown on self-organized nanopatterned substrates. *Advanced Materials*, 29(19):1605785, 2017. doi: 10.1002/adma.201605785.
- [86] V. S. Mangu, M. Zamiri, S. R. J. Brueck, and F. Cavallo. Strain engineering, efficient excitonic photoluminescence, and exciton funnelling in unmodified mos₂ nanosheets. *Nanoscale*, 9(43):16602–16606, 2017. doi: 10.1039/c7nr03537c.

Bibliography

- [87] Y. H. Jiang, J. H. Mao, J. X. Duan, X. Y. Lai, K. Watanabe, T. Taniguchi, and E. Y. Andrei. Visualizing strain-induced pseudomagnetic fields in graphene through an hbn magnifying glass. *Nano Letters*, 17(5):2839–2843, 2017. doi: 10.1021/acs.nanolett.6b05228.
- [88] J. K. Lee, S. Yamazaki, H. Yun, J. Park, G. P. Kennedy, G. T. Kim, O. Pietzsch, R. Wiesendanger, S. Lee, S. Hong, U. Dettlaff-Weglikowska, and S. Roth. Modification of electrical properties of graphene by substrate-induced nanomodulation. *Nano Letters*, 13(8):3494–3500, 2013. doi: 10.1021/nl400827p.
- [89] A. G. Milekhin, M. Rahaman, E. E. Rodyakina, A. V. Latyshev, V. M. Dzhagan, and D. R. T. Zahn. Giant gap-plasmon tip-enhanced raman scattering of mos2 monolayers on au nanocluster arrays. *Nanoscale*, 10(6):2755–2763, 2018. doi: 10.1039/c7nr06640f.
- [90] S. K. Deng, A. V. Sumant, and V. Berry. Strain engineering in two-dimensional nanomaterials beyond graphene. *Nano Today*, 22:14–35, 2018. doi: 10.1016/j.nantod.2018.07.001.
- [91] C. C. Hsu, M. L. Teague, J. Q. Wang, and N. C. Yeh. Nanoscale strain engineering of giant pseudo-magnetic fields, valley polarization, and topological channels in graphene. *Science Advances*, 6(19):eaat9488, 2020. doi: 10.1126/sciadv.aat9488.
- [92] C. Lee, X. D. Wei, J. W. Kysar, and J. Hone. Measurement of the elastic properties and intrinsic strength of monolayer graphene. *Science*, 321(5887):385–388, 2008. doi: 10.1126/science.1157996.
- [93] D. Wang, X. B. Li, D. Han, W. Q. Tian, and H. B. Sun. Engineering two-dimensional electronics by semiconductor defects. *Nano Today*, 16:30–45, 2017. doi: 10.1016/j.nantod.2017.07.001.
- [94] Y. J. Wei, J. T. Wu, H. Q. Yin, X. H. Shi, R. G. Yang, and M. Dresselhaus. The nature of strength enhancement and weakening by pentagon-heptagon defects in graphene. *Nature Materials*, 11(9):759–763, 2012. doi: 10.1038/Nmat3370.
- [95] P. Luo, F. W. Zhuge, Q. F. Zhang, Y. Q. Chen, L. Lv, Y. Huang, H. Q. Li, and T. Y. Zhai. Doping engineering and functionalization of two-dimensional metal chalcogenides. *Nanoscale Horizons*, 4(1):26–51, 2019. doi: 10.1039/c8nh00150b.
- [96] S. Carr, D. Massatt, S. Fang, P. Cazeaux, M. Luskin, and E. Kaxiras. Twistronics: Manipulating the electronic properties of two-dimensional layered structures through their twist angle. *Physical Review B*, 95(7):075420, 2017. doi: 10.1103/PhysRevB.95.075420.
- [97] Y. Hou, Z. H. Dai, S. Zhang, S. Z. Feng, G. R. Wang, L. Q. Liu, Z. P. Xu, Q. Y. Li, and Z. Zhang. Elastocapillary cleaning of twisted bilayer graphene interfaces. *Nature Communications*, 12(1):5069, 2021. doi: 10.1038/s41467-021-25302-2.
- [98] M. Yankowitz, S. W. Chen, H. Polshyn, Y. X. Zhang, K. Watanabe, T. Taniguchi, D. Graf, A. F. Young, and C. R. Dean. Tuning superconductivity in twisted bilayer graphene. *Science*, 363(6431):1059–1064, 2019. doi: 10.1126/science.aav1910.
- [99] K. S. Novoselov, A. K. Geim, S. V. Morozov, D. Jiang, Y. Zhang, S. V. Dubonos, I. V. Grigorieva, and A. A. Firsov. Electric field effect in atomically thin carbon films. *Science*, 306(5696):666–669, 2004. doi: 10.1126/science.1102896.
- [100] A. A. Balandin, S. Ghosh, W. Z. Bao, I. Calizo, D. Teweldebrhan, F. Miao, and C. N. Lau. Superior thermal conductivity of single-layer graphene. *Nano Letters*, 8(3):902–907, 2008. doi: 10.1021/nl0731872.

- [101] Y. B. Zhang, Y. W. Tan, H. L. Stormer, and P. Kim. Experimental observation of the quantum hall effect and berry's phase in graphene. *Nature*, 438(7065):201–204, 2005. doi: 10.1038/nature04235.
- [102] Y. Cao, V. Fatemi, A. Demir, S. Fang, S. L. Tomarken, J. Y. Luo, J. D. Sanchez-Yamagishi, K. Watanabe, T. Taniguchi, E. Kaxiras, R. C. Ashoori, and P. Jarillo-Herrero. Correlated insulator behaviour at half-filling in magic-angle graphene superlattices. *Nature*, 556(7699):80–84, 2018. doi: 10.1038/nature26154.
- [103] Y. Cao, V. Fatemi, S. Fang, K. Watanabe, T. Taniguchi, E. Kaxiras, and P. Jarillo-Herrero. Unconventional superconductivity in magic-angle graphene superlattices. *Nature*, 556(7699):43–50, 2018. doi: 10.1038/nature26160.
- [104] A. L. Sharpe, E. J. Fox, A. W. Barnard, J. Finney, K. Watanabe, T. Taniguchi, M. A. Kastner, and D. Goldhaber-Gordon. Emergent ferromagnetism near three-quarters filling in twisted bilayer graphene. *Science*, 365(6453):605–608, 2019. doi: 10.1126/science.aaw3780.
- [105] C. G. Liu, Z. N. Yu, D. Neff, A. Zhamu, and B. Z. Jang. Graphene-based supercapacitor with an ultrahigh energy density. *Nano Letters*, 10(12):4863–4868, 2010. doi: 10.1021/nl102661q.
- [106] Y. Wang, Z. Q. Shi, Y. Huang, Y. F. Ma, C. Y. Wang, M. M. Chen, and Y. S. Chen. Supercapacitor devices based on graphene materials. *Journal of Physical Chemistry C*, 113(30):13103–13107, 2009. doi: 10.1021/jp902214f.
- [107] S. Stankovich, D. A. Dikin, G. H. B. Dommett, K. M. Kohlhaas, E. J. Zimney, E. A. Stach, R. D. Piner, S. T. Nguyen, and R. S. Ruoff. Graphene-based composite materials. *Nature*, 442(7100):282–286, 2006. doi: 10.1038/nature04969.
- [108] Z. J. Gu, S. Zhu, L. Yan, F. Zhao, and Y. L. Zhao. Graphene-based smart platforms for combined cancer therapy. *Advanced Materials*, 31(9):1800662, 2019. doi: 10.1002/adma.201800662.
- [109] D. Iannazzo, A. Pistone, M. Salamo, S. Galvagno, R. Romeo, S. V. Giofre, C. Branca, G. Visalli, and A. Di Pietro. Graphene quantum dots for cancer targeted drug delivery. *International Journal of Pharmaceutics*, 518(1-2):185–192, 2017. doi: 10.1016/j.ijpharm.2016.12.060.
- [110] M. Orecchioni, R. Cabizza, A. Bianco, and L. G. Delogu. Graphene as cancer theranostic tool: Progress and future challenges. *Theranostics*, 5(7):710–723, 2015. doi: 10.7150/thno.11387.
- [111] F. Yavari and N. Koratkar. Graphene-based chemical sensors. *Journal of Physical Chemistry Letters*, 3(13):1746–1753, 2012. doi: 10.1021/jz300358t.
- [112] Youdi Kuang, Lucas Lindsay, Sanqiang Shi, Xinjiang Wang, and Baoling Huang. Thermal conductivity of graphene mediated by strain and size. *International Journal of Heat and Mass Transfer*, 101:772–778, 2016. doi: 10.1016/j.ijheatmasstransfer.2016.05.072.
- [113] V. S. D. K, S. K. Kannam, and S. P. Sathian. Thermal conductivity of graphene under biaxial strain: an analysis of spectral phonon properties. *Nanotechnology*, 31(34):345703, 2020. doi: 10.1088/1361-6528/ab9042.

Bibliography

- [114] F. Guinea. Strain engineering in graphene. *Solid State Communications*, 152(15):1437–1441, 2012. doi: 10.1016/j.ssc.2012.04.019.
- [115] D. Yoon, Y. W. Son, and H. Cheong. Strain-dependent splitting of the double-resonance raman scattering band in graphene. *Physical Review Letters*, 106(15):155502, 2011. doi: 10.1103/PhysRevLett.106.155502.
- [116] F. Ding, H. X. Ji, Y. H. Chen, A. Herklotz, K. Dorr, Y. F. Mei, A. Rastelli, and O. G. Schmidt. Stretchable graphene: A close look at fundamental parameters through biaxial straining. *Nano Letters*, 10(9):3453–3458, 2010. doi: 10.1021/nl101533x.
- [117] C. Si, Z. Liu, W. H. Duan, and F. Liu. First-principles calculations on the effect of doping and biaxial tensile strain on electron-phonon coupling in graphene. *Physical Review Letters*, 111(19):196802, 2013. doi: 10.1103/PhysRevLett.111.196802.
- [118] W. Z. Bao, F. Miao, Z. Chen, H. Zhang, W. Y. Jang, C. Dames, and C. N. Lau. Controlled ripple texturing of suspended graphene and ultrathin graphite membranes. *Nature Nanotechnology*, 4(9):562–566, 2009. doi: 10.1038/Nnano.2009.191.
- [119] Z. F. Wang, Y. Zhang, and F. Liu. Formation of hydrogenated graphene nanoripples by strain engineering and directed surface self-assembly. *Physical Review B*, 83(4):041403, 2011. doi: 10.1103/PhysRevB.83.041403.
- [120] Daniel R Dreyer, Alexander D Todd, and Christopher W Bielawski. Harnessing the chemistry of graphene oxide. *Chemical Society Reviews*, 43(15):5288–5301, 2014. doi: 10.1039/C4CS00060A.
- [121] M. S. Nevius, M. Conrad, F. Wang, A. Celis, M. N. Nair, A. Taleb-Ibrahimi, A. Tejada, and E. H. Conrad. Semiconducting graphene from highly ordered substrate interactions. *Physical Review Letters*, 115(13):136802, 2015. doi: 10.1103/PhysRevLett.115.136802.
- [122] S. Y. Zhou, G. H. Gweon, A. V. Fedorov, P. N. First, W. A. De Heer, D. H. Lee, F. Guinea, A. H. Castro Neto, and A. Lanzara. Substrate-induced bandgap opening in epitaxial graphene. *Nature Materials*, 6(10):770–775, 2007. doi: 10.1038/nmat2003.
- [123] R. Balog, B. Jorgensen, L. Nilsson, M. Andersen, E. Rienks, M. Bianchi, M. Fanetti, E. Laegsgaard, A. Baraldi, S. Lizzit, Z. Slijivancanin, F. Besenbacher, B. Hammer, T. G. Pedersen, P. Hofmann, and L. Hornekaer. Bandgap opening in graphene induced by patterned hydrogen adsorption. *Nature Materials*, 9(4):315–319, 2010. doi: 10.1038/Nmat2710.
- [124] D. C. Elias, R. R. Nair, T. M. G. Mohiuddin, S. V. Morozov, P. Blake, M. P. Halsall, A. C. Ferrari, D. W. Boukhvalov, M. I. Katsnelson, A. K. Geim, and K. S. Novoselov. Control of graphene’s properties by reversible hydrogenation: Evidence for graphane. *Science*, 323(5914):610–613, 2009. doi: 10.1126/science.1167130.
- [125] W. Liu, Z. F. Wang, Q. W. Shi, J. L. Yang, and F. Liu. Band-gap scaling of graphene nanohole superlattices. *Physical Review B*, 80(23):233405, 2009. doi: 10.1103/PhysRevB.80.233405.
- [126] F. P. Ouyang, S. L. Peng, Z. F. Liu, and Z. R. Liu. Bandgap opening in graphene antidot lattices: The missing half. *ACS Nano*, 5(5):4023–4030, 2011. doi: 10.1021/nn200580w.
- [127] V. M. Pereira, A. H. Castro Neto, and N. M. R. Peres. Tight-binding approach to uniaxial strain in graphene. *Physical Review B*, 80(4):045401, 2009. doi: 10.1103/PhysRevB.80.045401.

- [128] F. Guinea, M. I. Katsnelson, and A. K. Geim. Energy gaps and a zero-field quantum hall effect in graphene by strain engineering. *Nature Physics*, 6(1):30–33, 2009. doi: 10.1038/nphys1420.
- [129] D. H. Kang, H. Sun, M. Luo, K. Lu, M. Chen, Y. Kim, Y. Jung, X. Gao, S. J. Parluhutan, J. Ge, S. W. Koh, D. Giovanni, T. C. Sum, Q. J. Wang, H. Li, and D. Nam. Pseudo-magnetic field-induced slow carrier dynamics in periodically strained graphene. *Nature Communications*, 12(1):5087, 2021. doi: 10.1038/s41467-021-25304-0.
- [130] S. Y. Li, Y. Su, Y. N. Ren, and L. He. Valley polarization and inversion in strained graphene via pseudo-landau levels, valley splitting of real landau levels, and confined states. *Physical Review Letters*, 124(10):106802, 2020. doi: 10.1103/PhysRevLett.124.106802.
- [131] T. Low and F. Guinea. Strain-induced pseudomagnetic field for novel graphene electronics. *Nano Letters*, 10(9):3551–3554, 2010. doi: 10.1021/nl1018063.
- [132] W. Ortiz, N. Szpak, and T. Stegmann. Graphene nanoelectromechanical systems as valleytronic devices. *Physical Review B*, 106(3):035416, 2022. doi: 10.1103/PhysRevB.106.035416.
- [133] M. Settnes, S. R. Power, M. Brandbyge, and A. P. Jauho. Graphene nanobubbles as valley filters and beam splitters. *Physical Review Letters*, 117(27):276801, 2016. doi: 10.1103/PhysRevLett.117.276801.
- [134] S. Manzeli, D. Ovchinnikov, D. Pasquier, O. V. Yazyev, and A. Kis. 2d transition metal dichalcogenides. *Nature Reviews Materials*, 2(8):1–15, 2017. doi: 10.1038/natrevmats.2017.33.
- [135] M. Hosseini, M. Elahi, M. Pourfath, and D. Esseni. Strain-induced modulation of electron mobility in single-layer transition metal dichalcogenides mx_2 ($m = mo, w$; $x = s, se$). *Ieee Transactions on Electron Devices*, 62(10):3192–3198, 2015. doi: 10.1109/Ted.2015.2461617.
- [136] S. Pak, J. Lee, Y. W. Lee, A. R. Jang, S. Ahn, K. Y. Ma, Y. Cho, J. Hong, S. Lee, H. Y. Jeong, H. Im, H. S. Shin, S. M. Morris, S. Cha, J. I. Sohn, and J. M. Kim. Strain-mediated interlayer coupling effects on the excitonic behaviors in an epitaxially grown mos_2/ws_2 van der waals heterobilayer. *Nano Letters*, 17(9):5634–5640, 2017. doi: 10.1021/acs.nanolett.7b02513.
- [137] T. Cheiwchanchamnangij and W. R. L. Lambrecht. Quasiparticle band structure calculation of monolayer, bilayer, and bulk mos_2 . *Physical Review B*, 85(20):205302, 2012. doi: 10.1103/PhysRevB.85.205302.
- [138] Arend van der Zande and James Hone. Inspired by strain. *Nature Photonics*, 6(12):804–806, 2012. doi: 10.1038/nphoton.2012.303.
- [139] J. Feng, X. F. Qian, C. W. Huang, and J. Li. Strain-engineered artificial atom as a broad-spectrum solar energy funnel. *Nature Photonics*, 6(12):865–871, 2012. doi: 10.1038/Nphoton.2012.285.
- [140] Z. W. Peng, X. L. Chen, Y. L. Fan, D. J. Srolovitz, and D. Y. Lei. Strain engineering of 2d semiconductors and graphene: from strain fields to band-structure tuning and photonic applications. *Light-Science & Applications*, 9(1):190, 2020. doi: 10.1038/s41377-020-00421-5.

Bibliography

- [141] Heejun Yang, Sung Wng Kim, Manish Chhowalla, and Young Hee Lee. Structural and quantum-state phase transitions in van der waals layered materials. *Nature Physics*, 13 (10):931–937, 2017. doi: 10.1038/nphys4188.
- [142] Jing Zhu, Liangsheng Hu, Pengxiang Zhao, Lawrence Yoon Suk Lee, and Kwok-Yin Wong. Recent advances in electrocatalytic hydrogen evolution using nanoparticles. *Chemical Reviews*, 120(2):851–918, 2020. doi: 10.1021/acs.chemrev.9b00248.
- [143] B. Hinnemann, P. G. Moses, J. Bonde, K. P. Jorgensen, J. H. Nielsen, S. Horch, I. Chorkendorff, and J. K. Norskov. Biornimetic hydrogen evolution: Mos2 nanoparticles as catalyst for hydrogen evolution. *Journal of the American Chemical Society*, 127(15): 5308–5309, 2005. doi: 10.1021/ja0504690.
- [144] Thomas F. Jaramillo, Kristina P. Jørgensen, Jacob Bonde, Jane H. Nielsen, Sebastian Horch, and Ib Chorkendorff. Identification of active edge sites for electrochemical h2 evolution from mos2 nanocatalysts. *Science*, 317(5834):100–102, 2007. doi: 10.1126/science.1141483.
- [145] X. Zong, H. J. Yan, G. P. Wu, G. J. Ma, F. Y. Wen, L. Wang, and C. Li. Enhancement of photocatalytic h2 evolution on cds by loading mos2 as cocatalyst under visible light irradiation. *Journal of the American Chemical Society*, 130(23):7176–7177, 2008. doi: 10.1021/ja8007825.
- [146] X. B. Chen and G. J. Wang. Tuning the hydrogen evolution activity of ms2 (m = mo or nb) monolayers by strain engineering. *Physical Chemistry Chemical Physics*, 18(14): 9388–9395, 2016. doi: 10.1039/c5cp06475a.
- [147] Dohyun Rhuy, Youjin Lee, Ji Yoon Kim, Chansoo Kim, Yongwoo Kwon, Daniel J. Preston, In Soo Kim, Teri W. Odom, Kibum Kang, Dongwook Lee, and Won-Kyu Lee. Ultraefficient electrocatalytic hydrogen evolution from strain-engineered, multilayer mos2. *Nano Letters*, 22(14):5742–5750, 2022. doi: 10.1021/acs.nanolett.2c00938.
- [148] Ke Bian, Christoph Gerber, Andreas J. Heinrich, Daniel J. Müller, Simon Scheuring, and Ying Jiang. Scanning probe microscopy. *Nature Reviews Methods Primers*, 1(1):36, 2021. doi: 10.1038/s43586-021-00033-2.
- [149] Gerd Binnig and Heinrich Rohrer. Scanning tunneling microscopy—from birth to adolescence. *Reviews of Modern Physics*, 59(3):615–625, 1987. doi: 10.1103/revmodphys.59.615.
- [150] C Julian Chen. *Introduction to Scanning Tunneling Microscopy Third Edition*, volume 69. Oxford University Press, USA, 2021. ISBN 0198856555.
- [151] Paul K. Hansma and Jerry Tersoff. Scanning tunneling microscopy. *Journal of Applied Physics*, 61(2):R1–R24, 1987. doi: 10.1063/1.338189.
- [152] J. P. Ibe, P. P. Bey, S. L. Brandow, R. A. Brizzolara, N. A. Burnham, D. P. Dilella, K. P. Lee, C. R. K. Marrian, and R. J. Colton. On the electrochemical etching of tips for scanning tunneling microscopy. *Journal of Vacuum Science & Technology A: Vacuum, Surfaces, and Films*, 8(4):3570–3575, 1990. doi: 10.1116/1.576509.
- [153] L. Patra and R. Pandey. Mechanical properties of 2d materials: A review on molecular dynamics based nanoindentation simulations. *Materials Today Communications*, 31: 103623, 2022. doi: 10.1016/j.mtcomm.2022.103623.

- [154] J. W. Suk, A. Kitt, C. W. Magnuson, Y. Hao, S. Ahmed, J. An, A. K. Swan, B. B. Goldberg, and R. S. Ruoff. Transfer of cvd-grown monolayer graphene onto arbitrary substrates. *ACS Nano*, 5(9):6916–24, 2011. doi: 10.1021/nn201207c.
- [155] G. Binnig, C. F. Quate, and Ch Gerber. Atomic force microscope. *Physical Review Letters*, 56(9):930–933, 1986. doi: 10.1103/physrevlett.56.930.
- [156] Gerhard Meyer and Nabil M. Amer. Novel optical approach to atomic force microscopy. *Applied Physics Letters*, 53(12):1045–1047, 1988. doi: 10.1063/1.100061.
- [157] S. N. Magonov, V. Elings, and M. H. Whangbo. Phase imaging and stiffness in tapping-mode atomic force microscopy. *Surface Science*, 375(2-3):L385–L391, 1997. doi: 10.1016/S0039-6028(96)01591-9.
- [158] D. Necas and P. Klapetek. Gwyddion: an open-source software for spm data analysis. *Central European Journal of Physics*, 10(1):181–188, 2012. doi: 10.2478/s11534-011-0096-2.
- [159] G. Greczynski and L. Hultman. X-ray photoelectron spectroscopy: Towards reliable binding energy referencing. *Progress in Materials Science*, 107:100591, 2020. doi: 10.1016/j.pmatsci.2019.100591.
- [160] Ewen Smith and Geoffrey Dent. *Modern Raman spectroscopy: a practical approach*. John Wiley & Sons, 2019. ISBN 1119440556.
- [161] Leandro M. Malard, Lucas Lafeta, Renan S. Cunha, Rafael Nadas, Andreij Gadelha, Luiz Gustavo Cançado, and Ado Jorio. Studying 2d materials with advanced raman spectroscopy: Cars, srs and ters. *Physical Chemistry Chemical Physics*, 23(41):23428–23444, 2021. doi: 10.1039/d1cp03240b.
- [162] Ping-Heng Tan. *Raman Spectroscopy of two-dimensional materials*, volume 276. Springer, 2018. ISBN 981131828X.
- [163] Rusen Yan, Jeffrey R. Simpson, Simone Bertolazzi, Jacopo Brivio, Michael Watson, Xufei Wu, Andras Kis, Tengfei Luo, Angela R. Hight Walker, and Huili Grace Xing. Thermal conductivity of monolayer molybdenum disulfide obtained from temperature-dependent raman spectroscopy. *ACS Nano*, 8(1):986–993, 2014. doi: 10.1021/nn405826k.
- [164] Z. H. Dai, Y. Hou, D. A. Sanchez, G. R. Wang, C. J. Brennan, Z. Zhang, L. Q. Liu, and N. S. Lu. Interface-governed deformation of nanobubbles and nanotents formed by two-dimensional materials. *Physical Review Letters*, 121(26):266101, 2018. doi: 10.1103/PhysRevLett.121.266101.
- [165] Q. H. Zhang, Z. Y. Chang, G. Z. Xu, Z. Y. Wang, Y. P. Zhang, Z. Q. Xu, S. J. Chen, Q. L. Bao, J. Z. Liu, Y. W. Mai, W. H. Duan, M. S. Fuhrer, and C. X. Zheng. Strain relaxation of monolayer ws₂ on plastic substrate. *Advanced Functional Materials*, 26(47):8707–8714, 2016. doi: 10.1002/adfm.201603064.
- [166] N. N. Klimov, S. Jung, S. Z. Zhu, T. Li, C. A. Wright, S. D. Solares, D. B. Newell, N. B. Zhitenev, and J. A. Stroscio. Electromechanical properties of graphene drumheads. *Science*, 336(6088):1557–1561, 2012. doi: 10.1126/science.1220335.
- [167] G. G. Naumis, S. Barraza-Lopez, M. Oliva-Leyva, and H. Terrones. Electronic and optical properties of strained graphene and other strained 2d materials: a review. *Reports on Progress in Physics*, 80(9):096501, 2017. doi: 10.1088/1361-6633/aa74ef.

Bibliography

- [168] G. N. Greaves, A. L. Greer, R. S. Lakes, and T. Rouxel. Poisson's ratio and modern materials. *Nature Materials*, 10(11):823–837, 2011. doi: 10.1038/nmat3134.
- [169] P. H. Mott and C. M. Roland. Limits to poisson's ratio in isotropic materials. *Physical Review B*, 80(13):132104, 2009. doi: 10.1103/physrevb.80.132104.
- [170] Kenneth E Evans and Andrew Alderson. Auxetic materials: functional materials and structures from lateral thinking! *Advanced Materials*, 12(9):617–628, 2000. doi: 10.1002/(sici)1521-4095(200005)12:9<617::aid-adma617>3.0.co;2-3.
- [171] Chuanwei Huang and Lang Chen. Negative poisson's ratio in modern functional materials. *Advanced Materials*, 28(37):8079–8096, 2016. doi: 10.1002/adma.201601363.
- [172] Roderic Lakes. Advances in negative poisson's ratio materials. *Advanced Materials*, 5(4): 293–296, 1993. doi: 10.1002/adma.19930050416.
- [173] JB Choi and RS Lakes. Non-linear properties of metallic cellular materials with a negative poisson's ratio. *Journal of Materials Science*, 27:5375–5381, 1992. doi: 10.1007/BF02403846.
- [174] RS Lakes and K Elms. Indentability of conventional and negative poisson's ratio foams. *Journal of Composite Materials*, 27(12):1193–1202, 1993. doi: 10.1177/002199839302701203.
- [175] JB Choi and RS Lakes. Fracture toughness of re-entrant foam materials with a negative poisson's ratio: experiment and analysis. *International Journal of fracture*, 80:73–83, 1996. doi: 10.1007/BF00036481.
- [176] Chuanwei Huang and Lang Chen. Negative poisson's ratio in modern functional materials. *Advanced Materials*, 28(37):8079–8096, 2016. doi: 10.1002/adma.201601363.
- [177] Fabrizio Scarpa. Auxetic materials for bioprotheses [in the spotlight]. *IEEE Signal Processing Magazine*, 25(5):128–126, 2008. doi: 10.1109/MSP.2008.926663.
- [178] Marco Avellaneda and Pieter J Swart. Calculating the performance of 1–3 piezoelectric composites for hydrophone applications: an effective medium approach. *The Journal of the Acoustical Society of America*, 103(3):1449–1467, 1998. doi: 10.1121/1.421306.
- [179] JB Choi and RS Lakes. Design of a fastener based on negative poisson's ratio foam. *Cellular Polymers*, 10(3):205–212, 1991.
- [180] Mohammad Sanami, Naveen Ravirala, Kim Alderson, and Andrew Alderson. Auxetic materials for sports applications. *Procedia Engineering*, 72:453–458, 2014. doi: 10.1016/j.proeng.2014.06.079.
- [181] Jin-Wu Jiang and Harold S Park. Negative poisson's ratio in single-layer black phosphorus. *Nature Communications*, 5(1):4727, 2014. doi: 10.1038/ncomms5727.
- [182] Jianwei Han, Jiafeng Xie, Zhiya Zhang, Dezheng Yang, Mingsu Si, and Desheng Xue. Negative poisson's ratios in few-layer orthorhombic arsenic: First-principles calculations. *Applied Physics Express*, 8(4):041801, 2015. doi: 10.7567/APEX.8.041801.
- [183] Andrew J Mannix, Xiang-Feng Zhou, Brian Kiraly, Joshua D Wood, Diego Alducin, Benjamin D Myers, Xiaolong Liu, Brandon L Fisher, Ulises Santiago, and Jeffrey R Guest. Synthesis of borophenes: Anisotropic, two-dimensional boron polymorphs. *Science*, 350(6267):1513–1516, 2015. doi: 10.1126/science.aad1080.

- [184] Bei Liu, Mengqi Niu, Jia Fu, Zeyu Xi, Ming Lei, and Ruge Quhe. Negative poisson's ratio in puckered two-dimensional materials. *Physical Review Materials*, 3(5):054002, 2019. doi: 10.1103/physrevmaterials.3.054002.
- [185] Joseph N Grima, Michael C Grech, James N Grima-Cornish, Ruben Gatt, and Daphne Attard. Giant auxetic behaviour in engineered graphene. *Annalen der Physik*, 530(6): 1700330, 2018. doi: 10.1002/andp.201700330.
- [186] Y. Y. Wen, E. L. Gao, Z. X. Hu, T. G. Xu, H. B. Lu, Z. P. Xu, and C. Li. Chemically modified graphene films with tunable negative poisson's ratios. *Nature Communications*, 10(1): 2446, 2019. doi: 10.1038/s41467-019-10361-3.
- [187] H. S. Qin, Y. Sun, J. Z. Liu, M. J. Li, and Y. L. Liu. Negative poisson's ratio in rippled graphene. *Nanoscale*, 9(12):4135–4142, 2017. doi: 10.1039/c6nr07911c.
- [188] J. N. Grima, S. Winczewski, L. Mizzi, M. C. Grech, R. Cauchi, R. Gatt, D. Attard, K. W. Wojciechowski, and J. Rybicki. Tailoring graphene to achieve negative poisson's ratio properties. *Advanced Materials*, 27(8):1455–1459, 2015. doi: 10.1002/adma.201404106.
- [189] J. W. Jiang, T. C. Chang, and X. M. Guo. Tunable negative poisson's ratio in hydrogenated graphene. *Nanoscale*, 8(35):15948–15953, 2016. doi: 10.1039/c6nr04976a.
- [190] J. W. Jiang, T. C. Chang, X. M. Guo, and H. S. Park. Intrinsic negative poisson's ratio for single-layer graphene. *Nano Letters*, 16(8):5286–5290, 2016. doi: 10.1021/acs.nanolett.6b02538.
- [191] G. Z. Qin and Z. Z. Qin. Negative poisson's ratio in two-dimensional honeycomb structures. *npj Computational Materials*, 6(1):51, 2020. doi: 10.1038/s41524-020-0313-x.
- [192] Z. Z. Qin, G. Z. Qin, and M. Hu. Origin of anisotropic negative poisson's ratio in graphene. *Nanoscale*, 10(22):10365–10370, 2018. doi: 10.1039/c8nr00696b.
- [193] L. P. Yu, Q. M. Yan, and A. Ruzsinszky. Negative poisson's ratio in 1t-type crystalline two-dimensional transition metal dichalcogenides. *Nature Communications*, 8:15224, 2017. doi: 10.1038/ncomms15224.
- [194] Q. Q. Zhang, X. Xu, D. Lin, W. L. Chen, G. P. Xiong, Y. K. Yu, T. S. Fisher, and H. Li. Hyperbolically patterned 3d graphene metamaterial with negative poisson's ratio and supere-lasticity. *Advanced Materials*, 28(11):2229–2237, 2016. doi: 10.1002/adma.201505409.
- [195] A. Politano and G. Chiarello. Probing the young's modulus and poisson's ratio in graphene/metal interfaces and graphite: A comparative study. *Nano Research*, 8(6): 1847–1856, 2015. doi: 10.1007/s12274-014-0691-9.
- [196] Jz-Yuan Juo, Bong Gyu Shin, Wolfgang Stiepany, Marko Memmler, Klaus Kern, and Soon Jung Jung. In-situ atomic level observation of the strain response of graphene lattice. *Scientific Reports*, 13(1):2451, 2023. doi: 10.1038/s41598-023-29128-4.
- [197] Bong Gyu Shin, Ji-Hoon Park, Jz-Yuan Juo, Jing Kong, and Soon Jung Jung. Structural-disorder-driven critical quantum fluctuation and localization in two-dimensional semiconductors. *Nature Communications*, 14(1):2283, 2023. doi: 10.1038/s41467-023-38024-4.
- [198] J. Wan, J. W. Jiang, and H. S. Park. Negative poisson's ratio in graphene oxide. *Nanoscale*, 9(11):4007–4012, 2017. doi: 10.1039/c6nr08657h.

Bibliography

- [199] G. Gui, J. Li, and J. X. Zhong. Band structure engineering of graphene by strain: First-principles calculations. *Physical Review B*, 78(7):075435, 2008. doi: 10.1103/PhysRevB.78.075435.
- [200] Jun Kang, Hasan Sahin, and François M. Peeters. Mechanical properties of monolayer sulphides: a comparative study between mos2, hfs2 and tis3. *Physical Chemistry Chemical Physics*, 17(41):27742–27749, 2015. doi: 10.1039/c5cp04576b.
- [201] R. C. Cooper, C. Lee, C. A. Marianetti, X. D. Wei, J. Hone, and J. W. Kysar. Nonlinear elastic behavior of two-dimensional molybdenum disulfide. *Physical Review B*, 87(3):035423, 2013. doi: 10.1103/PhysRevB.87.035423.
- [202] N. T. Hung, A. R. T. Nugraha, and R. Saito. Two-dimensional mos2 electromechanical actuators. *Journal of Physics D: Applied Physics*, 51(7):075306, 2018. doi: 10.1088/1361-6463/aaa68f.
- [203] Si Xiong and Guoxin Cao. Molecular dynamics simulations of mechanical properties of monolayer mos2. *Nanotechnology*, 26(18):185705, 2015. doi: 10.1088/0957-4484/26/18/185705.
- [204] Yingye Gan and Huijuan Zhao. Chirality effect of mechanical and electronic properties of monolayer mos2 with vacancies. *Physics Letters A*, 378(38-39):2910–2914, 2014. doi: 10.1016/j.physleta.2014.08.008.
- [205] V. H. Ho, D. T. Ho, S. Y. Kwon, and S. Y. Kim. Negative poisson’s ratio in periodic porous graphene structures. *physica status solidi (b)*, 253(7):1303–1309, 2016. doi: 10.1002/pssb.201600061.
- [206] Nan Liu, Zhonghuai Pan, Lei Fu, Chaohua Zhang, Boya Dai, and Zhongfan Liu. The origin of wrinkles on transferred graphene. *Nano Research*, 4(10):996–1004, 2011. doi: 10.1007/s12274-011-0156-3.
- [207] Kwanpyo Kim, Zonghoon Lee, Brad D. Malone, Kevin T. Chan, Benjamín Alemán, William Regan, Will Gannett, M. F. Crommie, Marvin L. Cohen, and A. Zettl. Multiply folded graphene. *Physical Review B*, 83(24), 2011. doi: 10.1103/physrevb.83.245433.
- [208] Xuesong Li, Weiwei Cai, Jinho An, Seyoung Kim, Junghyo Nah, Dongxing Yang, Richard Piner, Aruna Velamakanni, Inhwa Jung, Emanuel Tutuc, Sanjay K. Banerjee, Luigi Colombo, and Rodney S. Ruoff. Large-area synthesis of high-quality and uniform graphene films on copper foils. *Science*, 324(5932):1312–1314, 2009. doi: 10.1126/science.1171245.
- [209] Keun Soo Kim, Yue Zhao, Houk Jang, Sang Yoon Lee, Jong Min Kim, Kwang S. Kim, Jong-Hyun Ahn, Philip Kim, Jae-Young Choi, and Byung Hee Hong. Large-scale pattern growth of graphene films for stretchable transparent electrodes. *Nature*, 457(7230):706–710, 2009. doi: 10.1038/nature07719.
- [210] I. Popov, G. Seifert, and D. Tomanek. Designing electrical contacts to mos2 monolayers: a computational study. *Physical Review Letters*, 108(15):156802, 2012. doi: 10.1103/PhysRevLett.108.156802.
- [211] E. Cha, M. D. Patel, J. Park, J. Hwang, V. Prasad, K. Cho, and W. Choi. 2d mos2 as an efficient protective layer for lithium metal anodes in high-performance li-s batteries. *Nature Nanotechnology*, 13(4):337–344, 2018. doi: 10.1038/s41565-018-0061-y.

- [212] D. Voiry, R. Fullon, J. E. Yang, C. D. C. E. Silva, R. Kappera, I. Bozkurt, D. Kaplan, M. J. Lagos, P. E. Batson, G. Gupta, A. D. Mohite, L. Dong, D. Q. Er, V. B. Shenoy, T. Asefa, and M. Chhowalla. The role of electronic coupling between substrate and 2d mos2 nanosheets in electrocatalytic production of hydrogen. *Nature Materials*, 15(9):1003–1009, 2016. doi: 10.1038/Nmat4660.
- [213] S. E. Thompson and S. Parthasarathy. Moore’s law: the future of si microelectronics. *Materials Today*, 9(6):20–25, 2006. doi: 10.1016/S1369-7021(06)71539-5.
- [214] S. McDonnell, C. Smyth, C. L. Hinkle, and R. M. Wallace. Mos2-titanium contact interface reactions. *ACS Applied Materials & Interfaces*, 8(12):8289–94, 2016. doi: 10.1021/acsami.6b00275.
- [215] K. Schauble, D. Zakhidov, E. Yalon, S. Deshmukh, R. W. Grady, K. A. Cooley, C. J. McClellan, S. Vaziri, D. Passarello, S. E. Mohney, M. F. Toney, A. K. Sood, A. Salleo, and E. Pop. Uncovering the effects of metal contacts on monolayer mos2. *ACS Nano*, 14(11):14798–14808, 2020. doi: 10.1021/acsnano.0c03515.
- [216] C. M. Smyth, R. Addou, S. McDonnell, C. L. Hinkle, and R. M. Wallace. Contact metal-mos2 interfacial reactions and potential implications on mos2-based device performance. *Journal of Physical Chemistry C*, 120(27):14719–14729, 2016. doi: 10.1021/acs.jpcc.6b04473.
- [217] R. C. Luo, W. W. Xu, Y. Z. Zhang, Z. Q. Wang, X. D. Wang, Y. Gao, P. Liu, and M. W. Chen. Van der waals interfacial reconstruction in monolayer transition-metal dichalcogenides and gold heterojunctions. *Nature Communications*, 11(1):1011, 2020. doi: 10.1038/s41467-020-14753-8.
- [218] C. C. Silva, D. Dombrowski, N. Atodiresei, W. Jolie, F. F. zum Hagen, J. Q. Cai, P. T. P. Ryan, P. K. Thakur, V. Caciuc, S. Blugel, D. A. Duncan, T. Michely, T. L. Lee, and C. Busse. Spatial variation of geometry, binding, and electronic properties in the moire superstructure of mos2 on au(111). *2D Materials*, 9(2):025003, 2022. doi: 10.1088/2053-1583/ac4958.
- [219] S. G. Sorensen, H. G. Fuchtbauer, A. K. Tuxen, A. S. Walton, and J. V. Lauritsen. Structure and electronic properties of in situ synthesized single-layer mos2 on a gold surface. *ACS Nano*, 8(7):6788–6796, 2014. doi: 10.1021/nn502812n.
- [220] Y. Huang, Y. H. Pan, R. Yang, L. H. Bao, L. Meng, H. L. Luo, Y. Q. Cai, G. D. Liu, W. J. Zhao, Z. Zhou, L. M. Wu, Z. L. Zhu, M. Huang, L. W. Liu, L. Liu, P. Cheng, K. H. Wu, S. B. Tian, C. Z. Gu, Y. G. Shi, Y. F. Guo, Z. G. Cheng, J. P. Hu, L. Zhao, G. H. Yang, E. Sutter, P. Sutter, Y. L. Wang, W. Ji, X. J. Zhou, and H. J. Gao. Universal mechanical exfoliation of large-area 2d crystals. *Nature Communications*, 11(1):2453, 2020. doi: 10.1038/s41467-020-16266-w.
- [221] B. T. Blue, G. G. Jernigan, D. Le, J. J. Fonseca, S. D. Lough, J. E. Thompson, D. D. Smalley, T. S. Rahman, J. T. Robinson, and M. Ishigami. Metallicity of 2h-mos2 induced by au hybridization. *2D Materials*, 7(2):025021, 2020. doi: 10.1088/2053-1583/ab6d34.
- [222] F. Wu, Z. T. Liu, N. Hawthorne, M. Chandross, Q. Moore, N. Argibay, J. F. Curry, and J. D. Batteas. Formation of coherent 1h-1t heterostructures in single-layer mos2 on au(111). *ACS Nano*, 14(12):16939–16950, 2020. doi: 10.1021/acsnano.0c06014.

Bibliography

- [223] Y. Liu, J. Guo, E. Zhu, L. Liao, S. J. Lee, M. Ding, I. Shakir, V. Gambin, Y. Huang, and X. Duan. Approaching the schottky-mott limit in van der waals metal-semiconductor junctions. *Nature*, 557(7707):696–700, 2018. doi: 10.1038/s41586-018-0129-8.
- [224] K. Jo, P. Kumar, J. Orr, S. B. Anantharaman, J. Miao, M. J. Motala, A. Bandyopadhyay, K. Kisslinger, C. Muratore, V. B. Shenoy, E. A. Stach, N. R. Glavin, and D. Jariwala. Direct optoelectronic imaging of 2d semiconductor-3d metal buried interfaces. *ACS Nano*, 15(3):5618–5630, 2021. doi: 10.1021/acsnano.1c00708.
- [225] M. Velicky, A. Rodriguez, M. Bousa, A. V. Krayev, M. Vondracek, J. Honolka, M. Ahmadi, G. E. Donnelly, F. M. Huang, H. D. Abruna, K. S. Novoselov, and O. Frank. Strain and charge doping fingerprints of the strong interaction between monolayer mos2 and gold. *Journal of Physical Chemistry Letters*, 11(15):6112–6118, 2020. doi: 10.1021/acs.jpcclett.0c01287.
- [226] S. Park, T. Schultz, X. M. Xu, B. Wegner, A. Aljarb, A. Han, L. J. Li, V. C. Tung, P. Amsalem, and N. Koch. Demonstration of the key substrate-dependent charge transfer mechanisms between monolayer mos2 and molecular dopants. *Communications Physics*, 2:109, 2019. doi: 10.1038/s42005-019-0212-y.
- [227] J. Gao, B. C. Li, J. W. Tan, P. Chow, T. M. Lu, and N. Koratkar. Aging of transition metal dichalcogenide monolayers. *ACS Nano*, 10(2):2628–2635, 2016. doi: 10.1021/acsnano.5b07677.
- [228] H. Bana, E. Travaglia, L. Bignardi, P. Lacovig, C. E. Sanders, M. Dendzik, M. Michiardi, M. Bianchi, D. Lizzit, F. Presel, D. De Angelis, N. Apostol, P. K. Das, J. Fujii, I. Vobornik, R. Larciprete, A. Baraldi, P. Hofmann, and S. Lizzit. Epitaxial growth of single-orientation high-quality mos2 monolayers. *2D Materials*, 5(3):035012, 2018. doi: 10.1088/2053-1583/aabb74.
- [229] A. Bruix, H. G. Fuchtbauer, A. K. Tuxen, A. S. Walton, M. Andersen, S. Porsgaard, F. Besenbacher, B. Hammer, and J. V. Lauritsen. In situ detection of active edge sites in single-layer mos2 catalysts. *ACS Nano*, 9(9):9322–9330, 2015. doi: 10.1021/acsnano.5b03199.
- [230] M. Donarelli, F. Bisti, F. Perrozzi, and L. Ottaviano. Tunable sulfur desorption in exfoliated mos2 by means of thermal annealing in ultra-high vacuum. *Chemical Physics Letters*, 588:198–202, 2013. doi: 10.1016/j.cplett.2013.10.034.
- [231] D. M. Sim, M. Kim, S. Yim, M. J. Choi, J. Choi, S. Yoo, and Y. S. Jung. Controlled doping of vacancy-containing few-layer mos2 via highly stable thiol-based molecular chemisorption. *ACS Nano*, 9(12):12115–12123, 2015. doi: 10.1021/acsnano.5b05173.
- [232] X. X. Zhang, S. P. Wang, C. K. Lee, C. M. Cheng, J. C. Lan, X. R. Li, J. Qiao, and X. T. Tao. Unravelling the effect of sulfur vacancies on the electronic structure of the mos2 crystal. *Physical Chemistry Chemical Physics*, 22(38):21776–21783, 2020. doi: 10.1039/c9cp07004d.
- [233] S. S. Chou, Y. K. Huang, J. Kim, B. Kaehr, B. M. Foley, P. Lu, C. Dykstra, P. E. Hopkins, C. J. Brinker, J. X. Huang, and V. P. Dravid. Controlling the metal to semiconductor transition of mos2 and ws2 in solution. *Journal of the American Chemical Society*, 137(5):1742–1745, 2015. doi: 10.1021/ja5107145.

- [234] G. Eda, H. Yamaguchi, D. Voiry, T. Fujita, M. W. Chen, and M. Chhowalla. Photoluminescence from chemically exfoliated mos₂. *Nano Letters*, 11(12):5111–5116, 2011. doi: 10.1021/nl201874w.
- [235] Jaehyuck Jung, Hunyoung Bark, Doyoung Byun, Changgu Lee, and Dae-Hyun Cho. Mechanical characterization of phase-changed single-layer mos₂ sheets. *2D Materials*, 6(2):025024, 2019. doi: 10.1088/2053-1583/ab070c.
- [236] X. Yin, Q. Wang, L. Cao, C. S. Tang, X. Luo, Y. Zheng, L. M. Wong, S. J. Wang, S. Y. Quek, W. Zhang, A. Rusydi, and A. T. S. Wee. Tunable inverted gap in monolayer quasi-metallic mos₂ induced by strong charge-lattice coupling. *Nature Communications*, 8(1):486, 2017. doi: 10.1038/s41467-017-00640-2.
- [237] J. Q. Zhu, Z. C. Wang, H. Yu, N. Li, J. Zhang, J. L. Meng, M. Z. Liao, J. Zhao, X. B. Lu, L. J. Du, R. Yang, D. Shi, Y. Jiang, and G. Y. Zhang. Argon plasma induced phase transition in monolayer mos₂. *Journal of the American Chemical Society*, 139(30):10216–10219, 2017. doi: 10.1021/jacs.7b05765.
- [238] S. Mignuzzi, A. J. Pollard, N. Bonini, B. Brennan, I. S. Gilmore, M. A. Pimenta, D. Richards, and D. Roy. Effect of disorder on raman scattering of single-layer mos₂. *Physical Review B*, 91(19):195411, 2015. doi: 10.1103/PhysRevB.91.195411.
- [239] B. Chakraborty, A. Bera, D. V. S. Muthu, S. Bhowmick, U. V. Waghmare, and A. K. Sood. Symmetry-dependent phonon renormalization in monolayer mos₂ transistor. *Physical Review B*, 85(16):161403, 2012. doi: 10.1103/PhysRevB.85.161403.
- [240] B. Liu, L. J. Wu, Y. Q. Zhao, L. Z. Wang, and M. Q. Cai. Tuning the schottky barrier height of the pd-mos₂ contact by different strains. *Physical Chemistry Chemical Physics*, 17(40):27088–27093, 2015. doi: 10.1039/c5cp04037j.
- [241] Daniel J. Trainer, Jouko Nieminen, Fabrizio Bobba, Baokai Wang, Xiaoxing Xi, Arun Bansil, and Maria Iavarone. Visualization of defect induced in-gap states in monolayer mos₂. *npj 2D Materials and Applications*, 6(1):13, 2022. doi: 10.1038/s41699-022-00286-9.
- [242] G. Q. Li, D. Zhang, Q. Qiao, Y. F. Yu, D. Peterson, A. Zafar, R. Kumar, S. Curtarolo, F. Hunte, S. Shannon, Y. M. Zhu, W. T. Yang, and L. Y. Cao. All the catalytic active sites of mos₂ for hydrogen evolution. *Journal of the American Chemical Society*, 138(51):16632–16638, 2016. doi: 10.1021/jacs.6b05940.
- [243] Fabian Bertoldo, Sajid Ali, Simone Manti, and Kristian S. Thygesen. Quantum point defects in 2d materials - the qpod database. *npj Computational Materials*, 8(1):56, 2022. doi: 10.1038/s41524-022-00730-w.
- [244] Elmar Mitterreiter, Bruno Schuler, Ana Micevic, Daniel Hernangómez-Pérez, Katja Barthelmi, Katherine A. Cochrane, Jonas Kiemle, Florian Sigger, Julian Klein, Edward Wong, Edward S. Barnard, Kenji Watanabe, Takashi Taniguchi, Michael Lorke, Frank Jahnke, Johnathan J. Finley, Adam M. Schwartzberg, Diana Y. Qiu, Sivan Refaely-Abramson, Alexander W. Holleitner, Alexander Weber-Bargioni, and Christoph Kastl. The role of chalcogen vacancies for atomic defect emission in mos₂. *Nature Communications*, 12(1):3822, 2021. doi: 10.1038/s41467-021-24102-y.
- [245] J. Klein, M. Lorke, M. Florian, F. Sigger, L. Sigl, S. Rey, J. Wierzbowski, J. Cerne, K. Müller, E. Mitterreiter, P. Zimmermann, T. Taniguchi, K. Watanabe, U. Wurstbauer, M. Kaniber,

Bibliography

- M. Knap, R. Schmidt, J. J. Finley, and A. W. Holleitner. Site-selectively generated photon emitters in monolayer mos2 via local helium ion irradiation. *Nature Communications*, 10(1):2755, 2019. doi: 10.1038/s41467-019-10632-z.
- [246] Yi Shi, Yue Zhou, Dong-Rui Yang, Wei-Xuan Xu, Chen Wang, Feng-Bin Wang, Jing-Juan Xu, Xing-Hua Xia, and Hong-Yuan Chen. Energy level engineering of mos2 by transition-metal doping for accelerating hydrogen evolution reaction. *Journal of the American Chemical Society*, 139(43):15479–15485, 2017. doi: 10.1021/jacs.7b08881.
- [247] Recep Zan, Chris Muryn, Ursel Bangert, Philip Mattocks, Paul Wincott, David Vaughan, Xuesong Li, Luigi Colombo, Rodney S. Ruoff, Bruce Hamilton, and Konstantin S. Novoselov. Scanning tunnelling microscopy of suspended graphene. *Nanoscale*, 4(10):3065, 2012. doi: 10.1039/c2nr30162h.
- [248] András Pálincás, György Molnár, Chanyong Hwang, László Péter Biró, and Zoltán Osváth. Determination of the stm tip-graphene repulsive forces by comparative stm and afm measurements on suspended graphene. *RSC Advances*, 6(89):86253–86258, 2016. doi: 10.1039/c6ra19660h.
- [249] P. Xu, Y. Yang, S. D. Barber, M. L. Ackerman, J. K. Schoelz, Igor A. Kornev, Salvador Barraza-Lopez, L. Bellaiche, and P. M. Thibado. Giant surface charge density of graphene resolved from scanning tunneling microscopy and first-principles theory. *Physical Review B*, 84(16):161409, 2011. doi: 10.1103/physrevb.84.161409.

Acknowledgements

First and foremost, I would like to express my sincere appreciation to my thesis advisor, Prof. Klaus Kern, for giving me the opportunity to do my PhD studies in his Nanoscale Science Department at the Max Planck Institute for Solid State Research in Stuttgart. I have enjoyed very much working at the state-of-art Precision Laboratory, the freedom to explore my ideas, and the challenges faced in this PhD project.

Next, I would like to thank the jury members in my thesis: Prof. Paolo Ricci, Prof. Nicolas Grandjean, Prof. Jannik Meyer, and Prof. Kirill Bolotin for dedicating their time to evaluate my work and providing invaluable suggestions.

I am deeply indebted to my day-to-day supervisor, Dr. Soon Jung Jung, whose unwavering belief in my abilities has been instrumental. She provided me with countless valuable suggestions, guided me through the most challenging times, and was a role model as a scientist and a parent to me. I also want to thank my senior colleague, Dr. Bong Gyu Shin, who introduced me to the field of STM and the sample preparation methods and shared useful skills and rigorous scientific practices with me. The regular discussions with them have significantly contributed to the development of my capabilities and logical thinking.

I want to thank Wolfgang Stiepany and Marko Memmler for their contributions to the design and fabrication of our crazy sample holder and Isabel Wolf for her support in troubleshooting our electronic devices. I also want to thank Sabine Birtel for helping me deal with everyday bureaucratic stuff and Anh Eymann for explaining anything that happened from the EPFL side. I am also grateful to Dr. Andreas Hupfer from SPECS for his invaluable support concerning our XPS system.

I am thankful for all kinds of support from my colleagues in the Nanoscale Science Department: Dr. Marko Burghard, Lukas Powalla, Dr. Sven Szilagyi, Peter Andler, Dr. Kelvin Anggara, Dr. Klaus Kuhnke, Dr. Haonan Huang, Dr. Liqing Zheng, Dr. Sujoy Karan, Dr. Manish Garg, Dr. Yang Luo, Dr. Shaoxiang Sheng, Dr. Aparajita Singha, Maneesha Ismail, Xianzhe Zeng.

I also thank Dr. Yu-Mi Wu, Yu-Hsiang Lin, Yu-Jung Wu, and Chun-Chieh Yen for the occasional gatherings and pleasant moments at the Institute, which have provided a refreshing break from academic pursuits.

Acknowledgements

I extend my deepest thanks to my family in Taiwan for their unconditional understanding and encouragement, which have been a constant source of support throughout my life.

Lastly, I am deeply grateful to my wife, Mei-Yi Liu, and my son, Bong-Hong Juo, who are the pillars of my existence. The joyous and challenging experiences that we have shared provide me with the strength and determination to overcome any future obstacles.

Filderstadt, July 5th 2023

Jz-Yuan Juo

Curriculum Vitae

Name Jz-Yuan Juo (卓至原)

Birth 10th December 1993
Hualien, Taiwan

Education

Sep 19 – **PhD Physics**
Ecole Polytechnique Federale de Lausanne, Switzerland
Advisor: Prof. Dr. Klaus Kern

Sep 11 – Jun 17 **MS & BS Physics**
National Cheng Kung University, Taiwan
Advisor: Prof. Yong-Fan Chen

Work Experience

Sep 19 – **PhD Researcher**
Max Planck Institute for Solid State Research, Germany
Director: Prof. Dr. Klaus Kern

Sep 18 – Aug 19 **Research Assistant**
Institute of Atomic and Molecular Sciences, Academia Sinica, Taiwan
Advisor: Dr. Chia-Lung Hsieh

Sep 17 – Sep 18 **Military Service**

Honor

Jun 20 **Taiwan Government Scholarship to Study Abroad**

Publications

11. J.-Y. Juo, K. Kern, S. J. Jung, "Atomic-scale Characterization of Strain Effects on Defect States of Monolayer MoS₂" In preparation
10. J.-Y. Juo, K. Kern, S. J. Jung, "Atomic-Scale Determination of Poisson's Ratio in Two-Dimensional Materials" In preparation
9. J.-Y. Juo, B. G. Shin, K. Kern, S. J. Jung, "Probing interfacial states in 2D semiconductor-metal junctions" To be submitted
8. J.-Y. Juo, B. G. Shin, W. Stiepany, M. Memmler, K. Kern, S. J. Jung, "In-situ atomic level observation of the strain response of graphene lattice" *Scientific Reports*, 13, 2451 (2023)
7. B. G. Shin, J.-H. Park, J.-Y. Juo, J. Kong, S. J. Jung, "Structural-disorder-driven critical quantum fluctuation and localization in two-dimensional semiconductors" *Nature Communications*, 14, 2283 (2023)
6. Y.-C. Huang, T.-H. Chen, J.-Y. Juo, S.-W. Chu, C.-L. Hsieh, "Quantitative Imaging of Single Light-Absorbing Nanoparticles by Widefield Interferometric Photothermal Microscopy" *ACS Photonics*, 8, 592–602 (2021)
5. C.-Y. Cheng, Z.-Y. Liu, P.-S. Hu, T.-N. Wang, C.-Y. Chien, J.-K. Lin, J.-Y. Juo, J.-S. Shiu, I. A. Yu, Y.-C. Chen, Y.-F. Chen, "Efficient frequency conversion based on resonant four-wave mixing" *Optics Letters*, 46, 681-684 (2021)
4. W. C. Wong*, J.-Y. Juo*, C.-H. Lin, Y.-H. Liao, C.-Y. Cheng, C.-L. Hsieh, "Characterization of Single-Protein dynamics in Polymer-Cushioned lipid bilayers derived from cell plasma membranes" *The Journal of Physical Chemistry B*, 123, 6492–6504 (2019)
*Equal contribution
3. Y.-H. Liao, C.-H. Lin, C.-Y. Cheng, W. C. Wong, J.-Y. Juo, C.-L. Hsieh, "Monovalent and Oriented Labeling of Gold Nanoprobes for the High-Resolution Tracking of a Single-Membrane Molecule" *ACS Nano*, 13, 10918-10928 (2019)
2. J.-Y. Juo, J.-K. Lin, C.-Y. Cheng, Z.-Y. Liu, I. A. Yu, Y.-F. Chen, "Demonstration of spatial-light-modulation-based four-wave mixing in cold atoms" *Physical Review A*, 97, 053815 (2018)
1. Z.-Y. Liu, J.-T. Xiao, J.-K. Lin, J.-J. Wu, J.-Y. Juo, C.-Y. Cheng, Y.-F. Chen, "High-efficiency backward four-wave mixing by quantum interference" *Scientific Reports*, 7, 15796 (2017)